Development of a flow-condition-based interpolation 9-node element for incompressible flows

by

Bahareh Banijamali

Submitted to the Department of Civil and Environmental Engineering
in partial fulfillment of the requirements for the degree of

Doctor of Philosophy in Structural Mechanics

at the

MASSACHUSETTS INSTITUTE OF TECHNOLOGY

February 2006

Author .....
Department of Civil and Environmental Engineering
August 23, 2005

Certified by .....
Klaus-Jürgen Bathe
Professor of Mechanical Engineering
Thesis Supervisor

Certified by .....
Franz-Josef Ulm
Associate Professor of Civil and Environmental Engineering
Thesis Supervisor

Accepted by .....
Andrew J. Whittle
Chairperson, Department Committee on Graduate Students

Development of a flow-condition-based interpolation 9-node element for incompressible flows

by

Bahareh Banijamali

Submitted to the Department of Civil and Environmental Engineering
on August 23, 2005, in partial fulfillment of the
requirements for the degree of
Doctor of Philosophy in Structures and Materials

Abstract

The Navier-Stokes equations are widely used for the analysis of incompressible laminar flows. If the Reynolds number is increased to certain values, oscillations appear in the finite element solution of the Navier-Stokes equations. In order to solve for high Reynolds number flows and avoid the oscillations, one technique is to use the flow condition-based interpolation scheme (FCBI), which is a hybrid of the finite element and the finite volume methods and introduces some upwinding into the laminar Navier-Stokes equations by using the exact solution of the advection-diffusion equation in the trial functions in the advection term.

The previous works on the FCBI procedure include the development of a 4-node element and a 9-node element consisting of four 4-node sub-elements. In this thesis, the stability, the accuracy and the rate of convergence of the already published FCBI schemes is studied. In addition, a new FCBI 9-node element is proposed that obtains more accurate solutions than the earlier proposed FCBI elements. The new 9-node element does not obtain the solution as accurate as the Galerkin 9-node elements but the solution is stable for much higher Reynolds numbers (than the Galerkin 9-node elements), and accurate enough to be used to find the structural responses in fluid flow structural interaction problems.

The Cubic-Interpolated Pseudo-particle (CIP) scheme is a very stable finite difference technique that can solve generalized hyperbolic equations with 3rd order accuracy in space. In this thesis, in order to solve the Navier-Stokes equations, the CIP scheme is linked to the finite element method (CIP-FEM) and the FCBI scheme (CIP-FCBI). From the numerical results, the CIP-FEM and the CIP-FCBI methods appear to predict the solution more accurate than the traditional finite element method and the FCBI scheme. In order to obtain accurate solutions for high Reynolds number flows, we require a finer mesh for the finite element and the FCBI methods than for the CIP-FEM and the CIP-FCBI methods. Linking the CIP method to the finite element and the FCBI methods improves the accuracy for the velocities and the derivatives. In addition, when the flow is not at the steady state and the time dependent terms need to be included in the Navier-Stokes equations, or in the prob-

lems when the derivatives of the velocities need to be obtained to high accuracy, the CIP-FCBI method is more convenient than the FCBI scheme.

Thesis Supervisor: Klaus-Jürgen Bathe
Title: Professor of Mechanical Engineering

Thesis Supervisor: Franz-Josef Ulm
Title: Associate Professor of Civil and Environmental Engineering

Acknowledgments

When I was offered a four year position as a Ph.D. student at MIT, I had only heard of the place. I barely thought I would go to MIT one day or spend four years of my life getting Ph.D. and being away from my family and my good friends. Assured by many that this was an opportunity that should not be missed, I left home and my loved ones. Now I realize that I have been extraordinarily lucky to have spent the last four years at MIT. There are so many wonderful things that could be said about MIT; the people, the lack of hierarchy, the open doors, the never-ending conversations, the atmosphere, the many workshops, countless interesting visitors and the diversity of interests. It is hard to imagine a more stimulating and encouraging academic environment. It will be difficult and sad to leave.

I am not leaving MIT only with the Ph.D. degree but with lots of memories and experiences. Memories of extremely stressful situations and memories of intense joy. I remember times I had wished to be away from MIT just to be able to be relax and sleep without being worried about my research, and times I had appreciated the chance of being a student at MIT. Needless to say that I could not have come so far if it were not for all the people that were near me, supported me, gave me strength and helped me to be patient and strong. During these four years, I have been fortunate to interact with many people who have influenced me greatly. One of the pleasures of finally finishing is this opportunity to thank them. I am sure I will not be able to include all of them, but at least let me mention the people that had most influenced my life during these four years.

First of all I would like to thank Prof. Klaus-Jürgen Bathe, my thesis advisor, who guided me through the world of research and supported me during the development of this research work. He gave me the opportunity to explore the world of finite element methods. His ability to rapidly assess the worth of ideas and algorithms is amazing. I would spend a week or two on an approach to a problem and Bathe could understand it, reconstruct it and tell me (correctly) that it would not work in about a minute. I would also want to thank the members of my Thesis Committee, Prof. Jerome J.

Connor and Prof Franz-Josef Ulm. I am particularly grateful to Prof. Connor. He is one of the people I will always respect and remember for his kind heart and the way he cares and supports all the students. In addition, I am thankful to Prof. Eduardo Kausel for always smiling and giving me support and encouragement whenever I was seeing him in the hallways or CEE events. I am also grateful to the researchers of ADINA R&D for their support with the use of ADINA.

I would also like to thank the people of the Finite Element Research Group at MIT (my lab-mates) Irfan Baig, Phill-Seung Lee, Junh-Wuk Hong, Jacques Olivier, Thomas Grätsch, Francisco Montans and Haruhiko Kono for their daily conversations and their friendship. Irfan, in particular, since we were the only two people in the lab during the last year of my thesis and he was always willing to talk with me and to give me advice and supportive comments.

I have made many friends along the way. Friends from different worlds and different cultures, people from each I learnt many new things. They have helped me, one way or another, in my struggle to complete my Ph.D. and my thesis. Many thanks to Farinaz Edalat, Taraneh Parvar, Maryam Modir Shanechi, Behnam Jafarpour, Sheila Tandon, Nima Shokrollahi and Elwin C Ong. In addition, many thanks to my friends back home, Mandana Bejanpour, Alireza Gharagozloo, Amir Maleki, Sanaz Khalili and Saharnaz Bigdeli and my cousin Soheila Chitsaz, who constantly loved me, supported me and gave me courage and strength during the four years of my Ph.D. at MIT.

I would also like to thank Blanche E Staton, Lynn Roberson and all the girls in the Graduate Women Group and Graduate Women Group in Civil Engineering department for their encouragement and support, and for providing a friendly atmosphere in the "Graduate Women Lounge". We spent many afternoons studying together or discussing our problems and sharing our experiences.

Cynthia Stewart, the academic administrator, is one of the many extremely competent people working at CEE department at MIT. The ongoing health of the CEE is, I believe, largely due to Cynthia's vision of what CEE and MIT should be, to her refusal to allow that vision to be compromised, to her warm and friendly personality,

and to her ability to deal calmly and rationally with any situation. She is fortunate to be surrounded by a team of people who combine to make CEE the unique place that it is. Jeanette Marchocki is one of them. Many many thanks to Cynthia and Jeanette to make me feel MIT was my home and I had a family here! I am also grateful to Una Sheehan, Deborah Alibrandi and Joan McCusker for always listening to me when I needed to talk, giving me hope and supporting me.

I would also like to thank my fiance and my best friend Yazdan. His support, encouragement, and companionship has turned the last year of my journey through Ph.D. into a pleasure. We proved that distance cannot, and will not hurt a bond between two people that is based on mutual respect, trust, commitment, and love. We believed that love and relationships are what make life special, and that ones built on love and understanding are always worth preserving, regardless of the miles that may separate two people.

It is not possible to summarize Bita, my sister, and her influence on me in one paragraph, but I will try. Bita has completely encouraged me and supported me over the last four years. Her love, intelligence, honesty, goodness, liveliness and kindness have given me strength and patience. She is the most caring person I have ever known. The fact of her existence is a continual miracle to me. She has supported me in hundreds of ways throughout the development and writing of this thesis.

Finally, my infinite gratitude goes to my parents, my best friends, for their love and encouragement and for always showing me the light at the end of the tunnel and giving meaning to my life. They have given their unconditional support, knowing that doing so contributed greatly to my absence these last four years. They were strong enough to let me go easily, to believe in me, and to let slip away all those years during which we could have been geographically closer and undoubtedly loving living together. Mom and dad, I love you, I am extremely grateful to what you have done for me and I am here because of you!

Contents

1 Introduction **15**

2 Governing equations of continua **21**

2.1 Eulerian formulation 22

2.2 Conservation equations 23

2.2.1 Mass conservation 24

2.2.2 Momentum conservation 25

2.3 Equations of motion 26

3 Finite element formulation **29**

4 Flow-condition-based interpolation scheme (FCBI) **35**

4.1 The governing equations 36

4.2 The fluid flow discretization 38

4.3 Fundamental properties of the FCBI procedure 51

4.4 Numerical examples 53

4.4.1 The driven cavity flow problem 53

4.4.2 The S-channel flow problem 59

4.5 Further study of the FCBI scheme 64

4.5.1 Stability of the FCBI scheme 64

4.5.2 Accuracy of the FCBI scheme 69

5 A new FCBI 9-node element **79**

5.1 Fluid flow discretization 81

5.2 Comparison of the new 9-node element with the earlier published 9-node element 92
5.3 Comparison of the new 9-node element with the Galerkin 9-node element 97

6 Linking FCBI to CIP method (CIP-FCBI) 107
6.1 CIP method 108
6.1.1 One-dimensional CIP solver 109
6.1.2 Two-dimensional CIP solver 115
6.1.3 The CIP solver for compressible and incompressible flows . . . 119
6.2 Linking the finite element method to the CIP method 123
6.2.1 The governing equations 123
6.2.2 Numerical solutions 131
6.3 Linking the FCBI scheme to the CIP method 136
6.3.1 The governing equations 136
6.3.2 Numerical solutions 145

7 Conclusions 151

A Consistency of the CIP scheme 155

B Stability of the CIP scheme 161

List of Figures

2-1 Reference, spatial and mesh configurations 23

4-1 The two-dimensional incompressible fluid flow problem considered . . 37

4-2 9-node elements and a sub-element in isoparametric coordinates . . . 39

4-3 The demonstration of x^1 and $1 - x^1$ functions for the flux through ab for the three different values of $q^1 = 10$, $q^1 = 0$ and $q^1 = 200$ 42

4-4 (a) The driven cavity flow problem (b) The uniform mesh of 8×8 elements used 54

4-5 Schematics of solutions for the driven cavity flow problem 55

4-6 The velocity solutions of the driven cavity flow problem for Re = 1, 100, 10,000, 1,000,000 for the uniform mesh 8 × 8 elements 56

4-7 The pressure solutions of the driven cavity flow problem for Re = 1, 100, 10,000, 1,000,000 for the uniform mesh 8 × 8 elements 57

4-8 Contours of the vorticity for different Re numbers for uniform mesh 8× 8 elements. The contour levels shown for each plot are -5.0, -4.0, -3.0, -2.0, -1.0, 0.0, 1.0, 2.0, 3.0, 4.0 and 5.0 58

4-9 The horizontal velocity at the vertical centerline of the cavity for Re = 100, 400, 1000, 5000 when the uniform mesh 8 × 8 elements is used 60

4-10 The vertical velocity at the horizontal centerline of the cavity for Re = 100, 400, 1000, 5000 when the uniform mesh 8× 8 elements is used 61

4-11 (a) The S-channel flow problem (b) The mesh used 62

4-12 Schematics of solutions for the S-channel flow problem (a) Re = 100, (b) Re = 10,000 63

4-13 The velocity solutions of the S-channel flow problem for $Re = 1, 100, 10, 000$ for the mesh shown in figure 4-11 (b) 65

4-14 The pressure solutions of the S-channel flow problem for $Re = 1, 100, 10, 000$ for the mesh shown in figure 4-11 (b) 66

4-15 Pressure solutions obtained by the FCBI procedure using the mesh shown in Fig. 4-11(b) and the two times finer and coarser meshes when $Re = 100$ 67

4-16 Pressure solutions obtained by the ADINA program using the mesh shown in Fig. 4-11(b) and the two times finer mesh when $Re = 100$. 68

4-17 The non-uniform mesh of 4×4 9-node elements used 73

4-18 Comparison of the FCBI 9-node elements, FCBI 4-node elements and the Galerkin 9-node elements for the driven cavity flow problem (Re=1000). In this figure, the x coordinate represents log h when h is the element size and the y coordinate for each case is a) $log\ \frac{\|\mathbf{u}-\mathbf{u}_h\|_{L^2}}{\|\mathbf{u}\|_{L^2}}$, b) $log\ \frac{\|\mathbf{u}-\mathbf{u}_h\|_{H^1}}{\|\mathbf{u}\|_{H^1}}$, c) $log\ \frac{\|p-p_h\|_{L^2}}{\|p\|_{L^2}}$, d) $log\ (\frac{\|\mathbf{u}-\mathbf{u}_h\|_{H^1}}{\|\mathbf{u}\|_{H^1}} + \frac{\|p-p_h\|_{L^2}}{\|p\|_{L^2}})$. 75

4-19 Comparison of the FCBI 9-node elements, FCBI 4-node elements and the Galerkin 9-node elements for the S-channel flow problem (Re=100). In this figure, the x coordinate represents log h when h is the element size and the y coordinate for each case is a) $log\ \frac{\|\mathbf{u}-\mathbf{u}_h\|_{L^2}}{\|\mathbf{u}\|_{L^2}}$, b) $log\ \frac{\|\mathbf{u}-\mathbf{u}_h\|_{H^1}}{\|\mathbf{u}\|_{H^1}}$, c) $log\ \frac{\|p-p_h\|_{L^2}}{\|p\|_{L^2}}$, d) $log\ (\frac{\|\mathbf{u}-\mathbf{u}_h\|_{H^1}}{\|\mathbf{u}\|_{H^1}} + \frac{\|p-p_h\|_{L^2}}{\|p\|_{L^2}})$. 77

5-1 The new FCBI 9-node element (a) The element in its isoparametric coordinates, (b) Definition of $\Delta\mathbf{x}^k$ for the flux through 5-7 82

5-2 The demonstration of f, g and ϕ functions for the flux through 5-7 for the three different values of $q^1 = 10$, $q^2 = 0$ and $q^3 = 200$ 85

5-3 The trial functions h_1^v, h_5^v and h_8^v for the flux through 5-7 87

5-4 The earlier proposed 9-node element (consists of four 4-node sub-elements); x^1 and $(1 - x^1)$ functions are shown for one sub-element and the assemblage of two adjacent sub-elements for high Reynolds number flow when the flux is through 5-7 89

5-5 Illustration of Ω_w and Ω_q; the control volumes of the velocity and pressure points respectively 92

5-6 Comparison of the new FCBI 9-node elements and the original FCBI 9-node elements for the driven cavity flow problem (Re=1000). In this figure, the x coordinate represents log h when h is the mesh size and the y coordinate for each case is a) $log\ \frac{\|\mathbf{u}-\mathbf{u}_h\|_{L^2}}{\|\mathbf{u}\|_{L^2}}$, b) $log\ \frac{\|\mathbf{u}-\mathbf{u}_h\|_{H^1}}{\|\mathbf{u}\|_{H^1}}$, c) $log\ \frac{\|p-p_h\|_{L^2}}{\|p\|_{L^2}}$, d) $log\ (\frac{\|\mathbf{u}-\mathbf{u}_h\|_{H^1}}{\|\mathbf{u}\|_{H^1}} + \frac{\|p-p_h\|_{L^2}}{\|p\|_{L^2}})$. 96

5-7 Comparison of the new FCBI 9-node elements and the original FCBI 9-node elements for the S-channel flow problem (Re=100). In this figure, the x coordinate represents log h when h is the mesh size and the y coordinate for each case is a) $log\ \frac{\|\mathbf{u}-\mathbf{u}_h\|_{L^2}}{\|\mathbf{u}\|_{L^2}}$, b) $log\ \frac{\|\mathbf{u}-\mathbf{u}_h\|_{H^1}}{\|\mathbf{u}\|_{H^1}}$, c) $log\ \frac{\|p-p_h\|_{L^2}}{\|p\|_{L^2}}$, d) $log\ (\frac{\|\mathbf{u}-\mathbf{u}_h\|_{H^1}}{\|\mathbf{u}\|_{H^1}} + \frac{\|p-p_h\|_{L^2}}{\|p\|_{L^2}})$. 99

5-8 Comparison of the new FCBI 9-node elements and the Galerkin 9-node elements for the driven cavity flow problem (Re=1000). In this figure, the x coordinate represents log h when h is the mesh size and the y coordinate for each case is a) $log\ \frac{\|\mathbf{u}-\mathbf{u}_h\|_{L^2}}{\|\mathbf{u}\|_{L^2}}$, b) $log\ \frac{\|\mathbf{u}-\mathbf{u}_h\|_{H^1}}{\|\mathbf{u}\|_{H^1}}$, c) $log\ \frac{\|p-p_h\|_{L^2}}{\|p\|_{L^2}}$, d) $log\ (\frac{\|\mathbf{u}-\mathbf{u}_h\|_{H^1}}{\|\mathbf{u}\|_{H^1}} + \frac{\|p-p_h\|_{L^2}}{\|p\|_{L^2}})$. 102

5-9 Comparison of the new FCBI 9-node elements and the Galerkin 9-node elements for the S-channel flow problem (Re=100). In this figure, the x coordinate represents log h when h is the mesh size and the y coordinate for each case is a) $log\ \frac{\|\mathbf{u}-\mathbf{u}_h\|_{L^2}}{\|\mathbf{u}\|_{L^2}}$, b) $log\ \frac{\|\mathbf{u}-\mathbf{u}_h\|_{H^1}}{\|\mathbf{u}\|_{H^1}}$, c) $log\ \frac{\|p-p_h\|_{L^2}}{\|p\|_{L^2}}$, d) $log\ (\frac{\|\mathbf{u}-\mathbf{u}_h\|_{H^1}}{\|\mathbf{u}\|_{H^1}} + \frac{\|p-p_h\|_{L^2}}{\|p\|_{L^2}})$. 105

6-1 The principle of the CIP method. (a) The initial profile and the exact solution (b) The exact solution at the grid points (c) Linear profile between the grid points (d) The spatial derivative in the CIP method 110

6-2 The 4-node element used in the finite element discretization 127

6-3 The driven cavity flow problem 131

6-4 The non-uniform meshes used for (a) $Re = 1000$, (b) $Re = 10000$. . . 133

6-5 Velocity profiles for $Re = 1000$. 134

6-6 Velocity profiles for $Re = 10000$. 135
6-7 9-node elements and the 4-node sub-element used in the finite element discretization 139
6-8 The non-uniform meshes used for (a) $Re = 1000$, (b) $Re = 10000$. . . 147
6-9 Velocity profiles for $Re = 1000$. 148
6-10 Velocity profiles for $Re = 10000$. 150

Chapter 1

Introduction

The study of incompressible flows is important in many areas of science and technology. At low speeds the flow will be ordered and follow regular patterns, i.e., it is *laminar* flow. Common applications in which laminar flow appears are biological fluid flow, Newtonian flows in chemical and mechanical engineering and any industrial process involving heat, fluid flow and mass transport at low Reynolds numbers. A balance between the inertia and viscous forces governs laminar flows and provides the stability. Flows are often characterized by a dimensionless number known as the *Reynolds number*, which is the ratio of inertia to viscous forces in a flow. Laminar flows correspond to smaller Reynolds numbers. Even though laminar flows are deterministic and ordered, instabilities and bifurcation may happen in the flow and take the flow from being laminar to be transition or *turbulent*. Numerical modelling of transition and turbulence requires greater insight into the flow physics.

For higher Reynolds numbers, the flow is governed by inertial forces and in most cases of engineering problems the flow is in a disordered or turbulent state. Common applications of incompressible turbulent flows involve the flow around vehicles and low speed flows in aeronautics where the fuel efficiency is greatly impacted by the details of the flow.

The Navier-Stokes equations are widely used for the analysis of incompressible laminar flows. If the Reynolds number is increased to certain values, oscillations appear in the finite element solution of the Navier-Stokes equations. In order to

solve for high Reynolds number flows and avoid the oscillations, one technique is to use *stabilized* methods. In these methods, artificial *upwinding* is introduced into the equations to stabilize the convective term, ideally without degrading the accuracy of the solution: e.g. the streamline upwind/Petrov-Galerkin (SUPG) method [7], the Galerkin/least-squares (GLS) method [15], the Cubic Interpolated Pseudo/Propagation (CIP) method [27] and use of the bubble functions [10], [6], [5], [22].

The flow condition-based interpolation scheme (FCBI) is a hybrid of the finite element and the finite volume methods and it was first introduced by *KJ. Bathe* and *J. Pontaza* in [2]. This scheme was later developed in [3], [19] and [20].

The FCBI procedure introduces some upwinding into the laminar Navier-Stokes equations by using the exact solution of the advection-diffusion equation in the trial functions in the advection term. The FCBI procedure is a finite element method since the domain of the problem is considered as an assemblage of discrete finite elements connected at nodal points on the element boundaries, and the velocity and the pressure are interpolated within each element. This procedure can also be considered a finite volume method since the weak form of the Navier-Stokes equations is satisfied over control volumes, when the test functions are unit step functions. Hence, the FCBI finite element solution satisfies the mass and momentum conservations for the control volumes (the traditional finite element methods do not satisfy the local mass and momentum conservations).

One reason why the FCBI procedure was proposed as a hybrid of the finite element and the finite volume methods, not being merely a finite volume method, is the lack of defining interpolation functions in the finite volume methods. Defining the interpolation functions enables us to directly evaluate the derivatives, and set up the Jacobian matrix for the Newton-Raphson iteration method. Also, no artificial factors are used and similar to the traditional finite element methods a mathematical theory is available.

The basic aim in developing an FCBI scheme is to reach a numerical scheme that is stable for low and high Reynolds numbers, and yields sufficiently accurate solutions using coarse meshes. Of course, the numerical solution of the laminar Navier-Stokes

equations at high Reynolds numbers would not be highly accurate. The fluid mesh would need to be too fine. However, when a coarse mesh is used, the scheme should still yield a reasonable solution. As the mesh is then refined, the numerical scheme would capture more details in the flow; e.g. circulations, and the solution obtained would ideally converge to the exact solution of the mathematical model. At some stages of the mesh refinement, a turbulent model might be required.

However, in practice, the accuracy of the solution and the computational cost are important issues. These issues are particularly important in the analysis of the fluid flows with structural interactions.

The analysis of fluid flows with structural interactions has captured much attention during the recent years. Such analysis is performed considering the solution of the Navier-Stokes fluid flows fully coupled to the non-linear structural response. However, a fully coupled fluid flow structural interaction analysis can be computationally very expensive. The cost of the solution is, roughly, proportional to the number of nodes or grid points used to discretize the fluid and the structure.

In order for interaction effects to be significant, the structure is usually thin and can be represented as a shell, hence not too many grid points are required. The large number of grid points and consequently number of equations in fluid flow structural interaction problems (FSI) is due to the representation of the fluid domain. For high Reynolds number fluid flows, to have a stable solution, more grid points are required. In order to decrease the number of grid points in the fluids (using a coarser mesh) and still have a stable solution, the flow-condition-based interpolation (FCBI) procedure was introduced [2], [3], [4].

The basic philosophy of FCBI scheme was presented earlier in [2]. However, our aim is to increase the effectiveness of this scheme. The previous works on the FCBI procedure include the development of a 4-node element and a 9-node element consisting of four 4-node sub-elements. In this thesis, the stability, the accuracy and the rate of convergence of the already published FCBI schemes is studied in section 4.5, and it is shown that the FCBI 4-node elements and the earlier proposed FCBI 9-node elements obtain more stable solutions than the Galerkin 9-node elements, used

in the traditional finite element methods. However, the Galerkin 9-node elements give more accurate solutions with a higher rate of convergence. Our objective is to use the FCBI scheme in rather coarse meshes together with the "goal-oriented error measurements" technique to control error in the structural response in the fluid flow structural interaction problems [12]. Hence, in chapter 5 we propose a new FCBI 9-node element that obtains more accurate solutions than the earlier proposed FCBI elements. The new 9-node element does not obtain the solution as accurate as the Galerkin 9-node elements but the solution is stable for much higher Reynolds numbers (than the Galerkin 9-node elements), and accurate enough to be used to find the structural responses.

In chapter 6, the focus is on the Cubic-Interpolated Pseudo-particle (CIP) method. The CIP method was introduced by T.Yabe *et al.* in 1991 [26], [17] . In this method, a cubic polynomial is used to interpolate spatial profiles and spatial derivatives. The spatial derivative itself is a free parameter and satisfies the master equation for the derivative. After the values have been found, the same values for the next time step are simply calculated by shifting the cubic polynomial.

The CIP scheme is a very stable finite difference technique that can solve generalized hyperbolic equations with 3rd order accuracy in space. In this thesis, in order to solve the Navier-Stokes equations, the CIP scheme is linked to the finite element method (CIP-FEM) and the FCBI scheme (CIP-FCBI).

The thesis is organized as follows. In Chapter 2 a brief review of the continuum governing equations for fluid flows is given, which includes the definition of the Eulerian formulation, the conservation equations and the equations of motion. Chapter 3 describes the finite element discretization of those governing equations. Chapter 4 is devoted to the introduction of the FCBI procedure, the discretization of the FCBI scheme for the earlier proposed 9-node elements (consisting of four 4-node sub-elements), the solution of some numerical examples and a further study of the FCBI scheme for these elements. Subsequently, in Chapter 5, a new FCBI 9-node element is proposed and compared with the former FCBI 9-node element and the Galerkin 9-node element. In Chapter 6, a review of the CIP method is given.

Then, in order to solve the Navier-Stokes equations, the CIP scheme is linked to the finite element method (CIP-FEM) and the FCBI scheme (CIP-FCBI) respectively. Finally, in Chapter 7 the conclusions of this work are given and future research in the development of the FCBI scheme is suggested.

Chapter 2

Governing equations of continua

In physics, materials are divided into three classes; solids, liquids and gases. In fluid mechanics, there are only two classes of matter: fluids and non-fluids (solids). In solid mechanics, one might follow the particle displacements since particles are bonded together. However in fluid mechanics, one's concern is normally the fluid velocity.

Consider the rigid-body dynamics problem of a rocket trajectory. We are finished after solving for the paths of any three non-collinear particles on the rocket since all other particle paths can be reached from these three paths. This scheme of following the trajectories of individual particles is called the *Lagrangian description* of motion and is very useful in solid mechanics.

But consider the fluid flow out of the nozzle of that rocket. Of course we cannot follow the millions of separate paths. Even the point of view is important, since an observer on the ground would see a complicated unsteady flow, while an observer fixed to the rocket might see a nearly steady flow of regular pattern. Thus it is useful in fluid mechanics to choose the most convenient origin of coordinates to make the flow appear steady, if it is possible, and to study the fluid velocity as a function of position and time, not to follow any specific particle path. This scheme of describing the flow at every fixed point as a function of time is called the *Eulerian formulation* of motion. In this chapter first the Eulerian formulation is briefly discussed, then the governing equations of Newtonian flows are considered.

2.1 Eulerian formulation

Consider a body that is moving from a *reference configuration*, the space occupied by the body at time $t = 0$, to the *spatial configuration*, the space occupied by the body at time t (see figure 2-1).

In the Lagrangian formulation, each fluid particle is labelled by its reference position $\mathbf{r}_0$ at time $t = 0$, giving velocity functions such as $\mathbf{v} = \mathbf{v}(\mathbf{r}_0, t)$. In the Eulerian formulation, a velocity field is specified by

$$\mathbf{v} = \mathbf{v}(\mathbf{r}, t) = \mathbf{v}(x, y, z, t) \tag{2.1}$$

That is, the velocity for time t is defined at the *fixed spatial position* $\mathbf{r}$. By defining this velocity, we can obtain a complete kinematic description of the flow. However, this function is not in general known in advance. The fixed spatial position $\mathbf{r}$ can be related to the reference position $\mathbf{r}_0$ as

$$\mathbf{r} = \varphi(\mathbf{r}_0, t) \tag{2.2}$$

If Q represents any property of the fluid, in the Eulerian formulation Q is given by

$$Q = f(\mathbf{r}, t) = F(\varphi(\mathbf{r}_0, t), t) \tag{2.3}$$

If dx, dy, dz and dt represent arbitrary changes in the four independent variables (x, y, z, t), the total differential change in Q is given by

$$dQ = \frac{\partial Q}{\partial x}\, dx + \frac{\partial Q}{\partial y}\, dy + \frac{\partial Q}{\partial z}\, dz + \frac{\partial Q}{\partial t}\, dt \tag{2.4}$$

For velocity components (v_x, v_y, v_z), the spatial increments must be such that

$$dx = v_x\, dt \qquad dy = v_y\, dt \qquad dy = v_z\, dt \tag{2.5}$$

Then, the expression for the time derivative of Q of a particular particle is

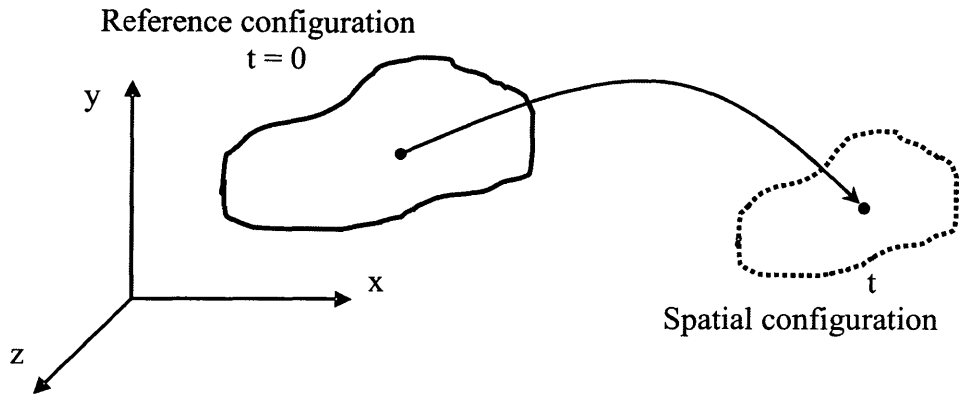

Figure 2-1: Reference, spatial and mesh configurations

$$\frac{DQ}{Dt} = \frac{\partial Q}{\partial t} + v_x \frac{\partial Q}{\partial x} + v_y \frac{\partial Q}{\partial y} + v_z \frac{\partial Q}{\partial z} \tag{2.6}$$

The quantity $\frac{DQ}{Dt}$ is called *material derivative* or *particle derivative* which shows that we are following a fixed particle. In this equation, $\frac{\partial Q}{\partial t}$ is the *local derivative* and the last three terms are called *convective derivatives.* The vector form of this equation is written as

$$\frac{DQ}{Dt} = \frac{\partial Q}{\partial t} + (\mathbf{v} \cdot \nabla) Q \tag{2.7}$$

2.2 Conservation equations

Consider a material volume moving from position $\mathbf{r}_0$ at time $t = 0$ to the new position $\mathbf{r}$ at t (see figure 2-1). The material volume is an arbitrary collection of matter enclosed by a *material surface* (or boundary) and every point of which moves with the local fluid velocity. This surface is hypothetical and in general does not correspond to any physical boundary in the flow. As the material volume moves through space, it is deformed in shape and changed in volume. We will refer to the material volume as $\Omega(t)$. The dynamical laws of motion are stated for the material volume and are as follows: *Conservation of mass* (continuity), *Balance of linear momentum* (Newton's

second law), *Balance of energy* (first law of thermodynamics) and *Creation of entropy* (second law of thermodynamics).

The first law, continuity, means that for a material volume the mass is constant. Newton's second law, momentum conservation, states that the rate of change of the volume momentum (momentum per unit volume) is equal to the sum of the surface forces (due to pressure and viscous stresses) and body forces (such as gravity) acting on it. From the first law of thermodynamics, the rate of change of the material-volume energy (internal plus kinetic) is equal to the rate at which forces do work upon it plus the rate at which heat is transferred to it. Finally, the second law of thermodynamics states that the change of internal entropy is greater or equal to the external entropy supply (due to the heat supply).

Our focus in this work is on isothermal processes of incompressible fluids. Hence, we only consider the mass and momentum conservations in this chapter.

2.2.1 Mass conservation

For a material volume the mass is constant, so that the conservation of mass takes the form

$$\frac{Dm}{Dt} = \frac{D}{Dt}\int_{\Omega(t)} \rho(\mathbf{r}) d\Omega = 0 \tag{2.8}$$

where $\Omega(t)$ is the material volume, m is the total mass enclosed in $\Omega(t)$ and ρ is the material density.

The differential equation of mass conservation can be derived from the integral equation with the application of the divergence theorem, and making use of the fact that the material volume is arbitrary. In the Lagrangian formulation, this equation is written as,

$$\frac{\rho(\mathbf{r}_0)}{\rho(\mathbf{r})} = det\ ({}^t_0\mathbf{X}) \tag{2.9}$$

where $({}^t_0\mathbf{X})$ is the deformation gradient (see [1]).

In the Eulerian formulation, this is equivalent to

$$\frac{D\rho}{Dt} + \rho\nabla \cdot \mathbf{v} = 0 \tag{2.10}$$

where $\mathbf{v}$ is the material velocity. If the density is constant (incompressible flow), this equation reduces to

$$\nabla \cdot \mathbf{v} = 0 \tag{2.11}$$

2.2.2 Momentum conservation

This law is called *Newton's law of motion* and it states that the rate of change of the material volume momentum is equal to the sum of all external forces acting on the body at time t.

$$\frac{D\mathbf{P}}{Dt} = \sum \mathbf{F}_{ext} \tag{2.12}$$

where $\mathbf{P}$ is the momentum of the material volume. This equation can also be written as

$$\frac{D}{Dt} \int_{\Omega(t)} \rho\mathbf{v} d\Omega = \sum \mathbf{F}_{ext}(t) \tag{2.13}$$

The differential equation of the above equation in Eulerian formulation is

$$\frac{D(\rho\mathbf{v})}{Dt} = \mathbf{f}_{body} = \mathbf{f}_{b1} + \mathbf{f}_{b2} \tag{2.14}$$

where $\mathbf{f}_{body}$ is the applied force on the fluid particles per unit volume, and contains two types of body forces: $\mathbf{f}_{b1}$, the gravitational body force (we only consider the gravitational force here) and $\mathbf{f}_{b2}$, which is the body force that satisfies the equilibrium. In the Lagrangian formulation, Newton's second law is easily written as $\mathbf{F}_{ext} = m\ \mathbf{a}$, where m is the mass and $\mathbf{a}$ is the acceleration of the body.

As it was already mentioned, only the gravitational body force is considered here and $\mathbf{f}_{b1} = \rho\ \mathbf{g}$, where $\mathbf{g}$ is the acceleration of gravity. The $\mathbf{f}_{b2}$ force satisfies equilibrium for the external stresses applied on the body and can be expressed as $\mathbf{f}_{b2} = \nabla \cdot \tau$,

where τ is the stress tensor. The momentum conservation then becomes

$$\frac{D(\rho \mathbf{v})}{Dt} = \rho\, \mathbf{g} + \nabla \cdot \tau \tag{2.15}$$

2.3 Equations of motion

The Navier-Stokes equations are derived from the momentum and mass conservation equations (2.15) and (2.10). It remains only to express τ in (2.15) in terms of the velocity $\mathbf{v}$. This is done by relating τ_{ij} to e_{ij} , the *(i,j)* th components of the stress and velocity strain tensors, through the Newtonian fluid constitutive law,

$$\tau_{ij} = -p\ \delta_{ij} + 2\mu e_{ij} \tag{2.16}$$

with

$$e_{ij} = \frac{1}{2}\ (v_{i,j} + v_{j,i}) \tag{2.17}$$

where p is the pressure and μ is the dynamic viscosity coefficient. The non-conservative form of the Navier-Stokes equations is obtained by substituting the stress relations (2.16) into Newton's law (2.15) as

$$\rho \frac{D\mathbf{v}}{Dt} = \rho\, \mathbf{g} - \nabla p + \mu \nabla^2 \mathbf{v} \tag{2.18}$$

The boundary conditions required to solve the Navier-Stokes equations can be given as follows:

$$\mathbf{v} = \mathbf{v}^s \quad on\ S_v \tag{2.19}$$

$$\tau \mathbf{n} = \mathbf{t} \quad on\ S_f \tag{2.20}$$

and the initial condition is

$$\mathbf{v}(t_0) = \mathbf{v}_0 \tag{2.21}$$

where S_v is the part of the fluid boundary with imposed velocities $\mathbf{v}^s$, S_f is the part of the boundary with imposed surface tractions $\mathbf{t}$ and $\mathbf{n}$ is the unit outward vector normal to the fluid boundary.

The momentum equation (2.15) can also be written as

$$\rho \frac{\partial v_i}{\partial t} + F_{ij,\,j} = \rho g_i \tag{2.22}$$

where

$$F_{ij,\,j} = \rho v_j v_i - \tau_{ij} \tag{2.23}$$

The above form is referred to as the conservative form of the momentum equation since for any material volume $\Omega(t)$ of the fluid, using the divergence theorem

$$\int_{\Omega(t)} F_{ij,\,j}\, d\Omega = \int_{S(t)} F_{ij} n_j\, dS \tag{2.24}$$

where $S(t)$ and the n_j are the material surface and the components of the unit vector normal to $S(t)$ respectively. Note that in the FCBI scheme, the conservative form of the momentum equation is used.

The Navier-Stokes equations are widely used for the analysis of incompressible viscous flows. However, viscosity is assumed to be constant in these equations and for non-isothermal flows, particularly for liquids whose viscosity is highly temperature-dependent, the Navier-Stokes equations may not be a good approximation. In our work, we only consider isothermal processes of incompressible fluids and the Navier-Stokes equations are used.

Chapter 3

Finite element formulation

In this chapter we consider the finite element formulation and solution of the Navier-Stokes equation given in (2.11) and (2.16).

Using index notation for a stationary Cartesian coordinate system (x_i, i=1,2,3), the Navier-Stokes equations (2.11) and (2.16) of incompressible fluid flow with in the domain Ω are (at time t),

$$\begin{aligned} &\rho\left(\frac{\partial v_i}{\partial t} + v_{i,\,j}\, v_j\right) = \tau_{ij,\,j} + f_i^B \\ &v_{i,\,i} = 0 \end{aligned} \tag{3.1}$$

where

$$\tau_{ij} = -p\,\delta_{ij} + 2\mu\, e_{ij} \tag{3.2}$$

and e_{ij} represents components of the velocity tensor and is given as,

$$e_{ij} = \frac{1}{2}\,(v_{i,\,j} + v_{j,\,i}) \tag{3.3}$$

Using index notation, the boundary conditions (2.19) and (2.20) are written as,

$$v_i = v_i^S \quad on\ S_v \tag{3.4}$$

$$\tau_{ij}\ n_j = f_i^S \quad on\ S_f \tag{3.5}$$

where S_v is the part of the fluid boundary with imposed velocities v_i^S, S_f is the part of the boundary with imposed surface tractions f_i^S and n_j are the components of the unit normal vector $\mathbf{n}$ (pointing outward) to the fluid surface.

The finite element solution of the Navier-Stokes equations (3.1) is obtained by considering a weak form of these equations. Using the Galerkin procedure (the test functions correspond to the finite element interpolations), the weak formulation of the problem can be given as:

Find $\mathbf{v} \in \mathbf{H}^1(\Omega)$ with $\mathbf{v} = \mathbf{v}^S$ on S_v, and $p \in H^1(\Omega)$ such that

$$\begin{aligned} &\int_\Omega \bar{v}_i\ \rho \left(\frac{\partial v_i}{\partial t} + v_{i,\ j}\ v_j \right) d\Omega + \int_\Omega \bar{e}_{ij}\ \tau_{ij}\ d\Omega = \int_\Omega \bar{v}_i\ f_i^B\ d\Omega + \int_{S_f} \bar{v}_i^S\ f_i^S\ dS \\ &\int_\Omega \bar{p}\ v_{i,\ i}\ d\Omega = 0 \end{aligned} \tag{3.6}$$

for all $\bar{\mathbf{v}} \in \mathbf{H}^1(\Omega)$ with $\bar{\mathbf{v}} = \mathbf{0}$ on S_v and $\bar{p} \in H^1(\Omega)$.

In the above expressions the overbar sign denotes the virtual quantity, the *Sobolev space* $H^k(\Omega)$ (for any non-negative integer k) is defined as the space of square integrable functions over Ω, whose derivatives up to order k are also square integrable over Ω.

In equations (3.6), the mixed-formulation is used (the velocity and the pressure are both considered as variables), and the momentum equation is weighted with the virtual velocity while the continuity equation is weighted with the virtual pressure. These equations must be discretized in space in order to be solved numerically. The following finite element spaces are introduced for the velocity and pressure,

$$
\begin{aligned}
\mathbf{V}^h &= \mathbf{v}^h \in \mathbf{H}^1(\Omega) \\
\bar{\mathbf{V}}^h &= \bar{\mathbf{v}}^h \in \mathbf{H}^1(\Omega) \\
Q^h &= p^h \in H^1(\Omega) \\
\bar{Q}^h &= \bar{p}^h \in H^1(\Omega)
\end{aligned}
\tag{3.7}
$$

Then, the finite element problem can be stated as:

Find $\mathbf{v}^h \in \mathbf{V}^h(\Omega)$ and $p^h \in Q^h(\Omega)$ such that

$$
\begin{aligned}
&\int_\Omega \bar{v}_i^h \; \rho \left(\frac{\partial v_i^h}{\partial t} + v_{i,\,j}^h \; v_j^h \right) d\Omega + \int_\Omega \bar{e}_{ij}^h \; \tau_{ij}^h \; d\Omega = \int_\Omega \bar{v}_i^h \; f_i^B \; d\Omega + \int_{S_f} (\bar{v}_i^h)^S \; f_i^S \; dS \\
&\int_\Omega \bar{p}^h \; v_{i,\,i}^h \; d\Omega = 0
\end{aligned}
\tag{3.8}
$$

for all $\bar{\mathbf{v}}^h \in \bar{\mathbf{V}}^h(\Omega)$ with $\bar{\mathbf{v}}^h = \mathbf{0}$ on S_v and $\bar{p} \in \bar{Q}^h(\Omega)$.

In the finite element procedure, the space $\mathbf{V}^h$ depends on the elements chosen to discretize the volume Ω. In a 2D space, we can choose, for example, quadrilateral bilinear or parabolic elements. The pressure interpolation, however, cannot be chosen arbitrary (see for example [1]), otherwise, the formulation may not be stable. In order to have stability, the *inf-sup* condition must be satisfied. A list of the effective v/p (velocities are continuous between elements) and v/p-c elements (velocities and pressures are both continuous between elements) are given in table (4.6) and (4.7) in [1].

Using any of these elements (that satisfy the *inf-sup* condition) to discretize equations (3.8) in steady-state two-dimensional planar flow analysis, the governing matrix equations for a single element are then,

$$\begin{pmatrix} \mathbf{K}_{\mathbf{v}_x\mathbf{v}_x} & \mathbf{K}_{\mathbf{v}_x\mathbf{v}_y} & \mathbf{K}_{\mathbf{v}_x\mathbf{p}} \\ \mathbf{K}_{\mathbf{v}_y\mathbf{v}_x} & \mathbf{K}_{\mathbf{v}_y\mathbf{v}_y} & \mathbf{K}_{\mathbf{v}_y\mathbf{p}} \\ \mathbf{K}_{\mathbf{p}\mathbf{v}_x} & \mathbf{K}_{\mathbf{p}\mathbf{v}_y} & \mathbf{0} \end{pmatrix} \begin{pmatrix} \Delta\mathbf{v}_x \\ \Delta\mathbf{v}_y \\ \Delta\mathbf{p} \end{pmatrix} = \begin{pmatrix} \mathbf{R}_{\mathbf{v}_x} \\ \mathbf{R}_{\mathbf{v}_y} \\ \mathbf{0} \end{pmatrix} - \begin{pmatrix} \mathbf{F}_{\mathbf{v}_x} \\ \mathbf{F}_{\mathbf{v}_y} \\ \mathbf{F}_{\mathbf{p}} \end{pmatrix} \tag{3.9}$$

In these equations, $\Delta\mathbf{v}_x$, $\Delta\mathbf{v}_y$, $\Delta\mathbf{p}$, are the *increments* of the velocity in the x direction, the velocity in the y direction and the pressure with respect to the last iteration; $\mathbf{R}_{\mathbf{v}_x}$ and $\mathbf{R}_{\mathbf{v}_y}$ are the discretized load vectors and $\mathbf{F}_{\mathbf{v}_x}$, $\mathbf{F}_{\mathbf{v}_y}$, $\mathbf{F}_{\mathbf{p}}$ contain terms from the linearization process [1].

If $\mathbf{H}^v$ and $\mathbf{H}^p$ contain the interpolation functions for the velocities and the pressure respectively, the elements of the stiffness matrix are

$$
\begin{aligned}
\mathbf{K}_{\mathbf{v}_x\mathbf{v}_x} &= \int_\Omega \left[2\mu\ (\mathbf{H}^v_{,\,x})^T\ \mathbf{H}^v_{,\,x} + \mu\ (\mathbf{H}^v_{,\,y})^T\ \mathbf{H}^v_{,\,y}\right] d\Omega \\
&\quad + \rho \int_\Omega \left[\ (\mathbf{H}^v)^T\ \mathbf{H}^v\mathbf{v}_x\ \mathbf{H}^v_{,\,x} + (\mathbf{H}^v)^T\ \mathbf{H}^v\mathbf{v}_y\ \mathbf{H}^v_{,\,y}\right] d\Omega \\
\mathbf{K}_{\mathbf{v}_x\mathbf{v}_y} &= \int_\Omega \mu\ (\mathbf{H}^v_{,\,y})^T\ \mathbf{H}^v_{,\,x}\ d\Omega \\
\mathbf{K}_{\mathbf{v}_x\mathbf{p}} &= -\int_\Omega (\mathbf{H}^v_{,\,x})^T\ \mathbf{H}^p\ d\Omega \\
\mathbf{K}_{\mathbf{v}_y\mathbf{v}_x} &= (\mathbf{K}_{\mathbf{v}_x\mathbf{v}_y})^T \\
\mathbf{K}_{\mathbf{v}_y\mathbf{v}_y} &= \int_\Omega \left[2\mu\ (\mathbf{H}^v_{,\,y})^T\ \mathbf{H}^v_{,\,y} + \mu\ (\mathbf{H}^v_{,\,x})^T\ \mathbf{H}^v_{,\,x}\right] d\Omega \\
&\quad + \rho \int_\Omega \left[\ (\mathbf{H}^v)^T\ \mathbf{H}^v\mathbf{v}_x\ \mathbf{H}^v_{,\,x} + (\mathbf{H}^v)^T\ \mathbf{H}^v\mathbf{v}_y\ \mathbf{H}^v_{,\,y}\right] d\Omega \\
\mathbf{K}_{\mathbf{v}_y\mathbf{p}} &= -\int_\Omega (\mathbf{H}^v_{,\,y})^T\ \mathbf{H}^p\ d\Omega \\
\mathbf{K}_{\mathbf{p}\mathbf{v}_x} &= (\mathbf{K}_{\mathbf{v}_x\mathbf{p}})^T \\
\mathbf{K}_{\mathbf{p}\mathbf{v}_y} &= (\mathbf{K}_{\mathbf{v}_y\mathbf{p}})^T
\end{aligned}
\tag{3.10}
$$

Since in this work, we only consider the incompressible fluid flow, $\mathbf{K}_{\mathbf{pp}} = \mathbf{0}$ and $\Delta\mathbf{p}$ cannot be statically condensed out for each element.

For a fluid flow problem, the solution obtained using the discretized equations (3.9) and (3.10) is good for low Reynolds number flows (laminar flows). However, if the Reynolds number is increased to certain values, oscillations appear in the solution

due to the presence of the convective terms $v_{i,\,j}\,v_j$ in equations (3.6).

Before we discuss how to avoid these oscillations, we mention that, of course, after Reynolds number is increased to a certain range, the flow condition turns from laminar to turbulent, and a turbulence model should be used. However, the turbulent flow could still be solved using the laminar Navier-Stokes equations. In order to increase the accuracy of the solution for high Reynolds number flows, the mesh need to be too fine and the analysis can be computationally very expensive.

In order to solve the high Reynolds number flows, one technique is to use *stabilized* methods. In these methods, artificial *upwinding* is introduced into the equations to stabilize the convective term, ideally without degrading the accuracy of the solution.

Different stabilized methods have been proposed and compared in various papers, i.e. the streamline upwind/Petrov-Galerkin (SUPG) method [7], the Galerkin/least-squares (GLS) method [15] and use of the bubble functions [10], [6], [5], [22].

Among all the proposed stabilized methods, this thesis focuses on two of these methods; the flow-condition-based interpolation (FCBI) procedure [2] and the Cubic Interpolated Pseudo/Propagation (CIP) method [27]. The FCBI procedure introduces some upwinding into the laminar Navier-Stokes equations by using the exact solution of the advection-diffusion equation in the trial functions in the advection term. Chapter 4 is devoted to the introduction of the FCBI procedure, the discretization of the FCBI scheme for the earlier published 9-node elements (consist of four 4-node sub-elements), the solution of some numerical examples and the stability and convergence study of the FCBI scheme for these elements. Subsequently, in Chapter 5, a new 9-node FCBI element is proposed and compared with the former FCBI 9-node element. In Chapter 6, the focus is on the CIP scheme. This chapter begins by reviewing the CIP procedure, then linking the CIP scheme to the finite element method (CIP-FEM) and finally to the FCBI procedure (CIP-FCBI).

Chapter 4

Flow-condition-based interpolation scheme (FCBI)

The flow condition-based interpolation scheme (FCBI) is a hybrid of the finite element and the finite volume methods and it was first introduced by *KJ. Bathe* and *J. Pontaza* in [2]. This scheme was later developed in [3], [19] and [20].

As it was mentioned earlier in chapter 3, if the Reynolds number is increased to certain values, oscillations appear in the traditional finite element solution of the laminar Navier-Stokes equations. In order to solve the high Reynolds number flows and avoid the oscillations, one technique is to use *stabilized* methods. In these methods, artificial *upwinding* is introduced into the equations to stabilize the convective term, ideally without degrading the accuracy of the solution.

The FCBI procedure introduces some upwinding into the laminar Navier-Stokes equations by using the exact solution of the advection-diffusion equation in the trial functions in the advection term. The FCBI procedure is a finite element method since the domain of the problem is considered as an assemblage of discrete finite elements connected at nodal points on the element boundaries, and the velocity and the pressure are interpolated within each element. This procedure is also considered as a finite volume method since the weak form of the Navier-Stokes equations is satisfied over the control volumes, when the test functions are unit step functions. Hence, the FCBI finite element solution satisfies the mass and momentum conservations for the

control volumes (the traditional finite element methods do not satisfy the mass and momentum conservations).

The main reason the FCBI procedure was proposed as a hybrid of the finite element and the finite volume methods, not merely a finite volume method, is that interpolation functions are not defined in the finite volume methods. Defining the interpolation functions enables us to directly evaluate the derivatives, and set up the Jacobian matrix for the Newton-Raphson iteration method.

In this chapter first the review of the FCBI procedure is given for the earlier published 9-node element (consists of four 4-node sub-elements) [3]. Then, the effectiveness of this method is tested by solving some numerical problems. At the end of this chapter, the stability and convergence study of this method is presented.

4.1 The governing equations

We consider the conservative form of the Navier-Stokes equations of a two-dimensional incompressible fluid flow within the domain Ω at time t (figure 4-1),

$$\begin{aligned} &\frac{\partial \rho \mathbf{v}}{\partial t} + \nabla \cdot (\rho \mathbf{v}\mathbf{v} - \boldsymbol{\tau}) = \mathbf{0} && (\mathbf{x}, t) \in \Omega \times [0, T] \\ &\nabla \cdot (\rho \mathbf{v}) = 0 && (\mathbf{x}, t) \in \Omega \times [0, T] \end{aligned} \tag{4.1}$$

subject to the (sufficiently smooth) initial and boundary conditions

$$\begin{aligned} &\mathbf{v}(\mathbf{x}, 0) = \mathbf{v}^0 && (\mathbf{x}) \in \Omega \\ &p(\mathbf{x}, 0) = p^0 && (\mathbf{x}) \in \Omega \\ &\mathbf{v} = \mathbf{v}^S && (\mathbf{x}, t) \in S_v \times (0, T) \\ &\boldsymbol{\tau} \cdot \mathbf{n} = \mathbf{f}^S && (\mathbf{x}, t) \in S_f \times (0, T) \end{aligned} \tag{4.2}$$

where

$$\boldsymbol{\tau} = \boldsymbol{\tau}(\mathbf{v}, p) = -p\,\mathbf{I} + \mu\,[\nabla\mathbf{v} + (\nabla\mathbf{v})^T] \tag{4.3}$$

In equations (4.1-4.3), μ is the viscosity, ρ is the density, $\mathbf{v}^S$ are the prescribed velocities on the boundary S_v, $\mathbf{f}^S$ are the prescribed tractions on the boundary S_f ($S = S_v \cup S_f$, $S_v \cap S_f = \emptyset$) and $\mathbf{n}$ is the unit vector normal to the boundary.

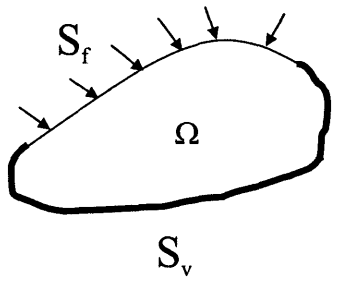

Figure 4-1: The two-dimensional incompressible fluid flow problem considered

The finite element solution of the Navier-Stokes equations (4.1) is obtained by considering a weak form of these equations. Using the Petrov-Galerkin procedure (the test functions do not correspond to the trial functions), the weak formulation of the problem can be given as

Find $\mathbf{v}_h \in V_h$, $\mathbf{u}_h \in U_h$ and $p_h \in P_h$ such that

$$\begin{aligned} &\int_\Omega w_h \left[\frac{\partial \rho \mathbf{u}_h}{\partial t} + \nabla \cdot (\rho\, \mathbf{u}_h \mathbf{v}_h - \boldsymbol{\tau}_h(\mathbf{u}_h, p_h))\right] d\Omega = \mathbf{0} \\ &\int_\Omega q_h \nabla \cdot (\rho\, \mathbf{u}_h)\, d\Omega = 0 \end{aligned} \tag{4.4}$$

where $w_h \in W_h$ and $q_h \in Q_h$.

Note that in these equations, the convective term $(\rho\mathbf{v}\mathbf{v})$ in equation (4.1) is replaced by $(\rho\mathbf{u}_h\mathbf{v}_h)$ in the weak formulation where $\mathbf{v}_h \in V_h$ and $\mathbf{u}_h \in U_h$ (two different spaces are defined for the velocities but of course the functions in these spaces are

defined for the same nodal velocity variables). The idea of using these two different spaces lies in that it is the convective term that for high Reynolds numbers introduces the instability and oscillation in the numerical solution . Hence, the convective term needs to be interpolated exponentially. Therefore, we replace the convective term ($\rho\ \mathbf{v}_h\mathbf{v}_h$) by ($\rho\ \mathbf{u}_h\mathbf{v}_h$) and we define the interpolation functions to be exponential in V_h and linear in U_h. Another reason is that then the FCBI scheme is also applicable to any other transport equation, for example, the advection-diffusion equation where, in the convective term, the temperature would be interpolated in V_h and the velocity in U_h.

4.2 The fluid flow discretization

The spaces used in the finite element procedure depend on the elements chosen to discretize the volume Ω. In this chapter, we consider the earlier published 9-node element (consists of four 4-node sub-elements) [3].

A mesh of elements is shown in its natural coordinate systems in figure 4-2. Each 9-node element is defined in the $r-s$ coordinates with $0 \leq r, s \leq 1.0$ and consists of four 4-node sub-elements. Each sub-element is defined by four nodes of the 9-node element and is used for the interpolation of velocities. The pressure is interpolated by the four corner points in each element. Hence, for the definition of the spaces V_h, U_h and P_h, we refer to the sub-elements and elements respectively. The sub-element is defined in $\xi-\eta$ coordinates with $0 \leq \xi, \eta \leq 1.0$. To obtain the matrices or derivatives in $x-y$ coordinates, the usual isoparametric transformation is used [1].

The trial functions in U_h are defined in each sub-element as,

$$\begin{bmatrix} h_1^u & h_4^u \\ h_2^u & h_3^u \end{bmatrix} = \begin{bmatrix} 1-\xi \\ \xi \end{bmatrix} \begin{bmatrix} 1-\eta & \eta \end{bmatrix} \tag{4.5}$$

or

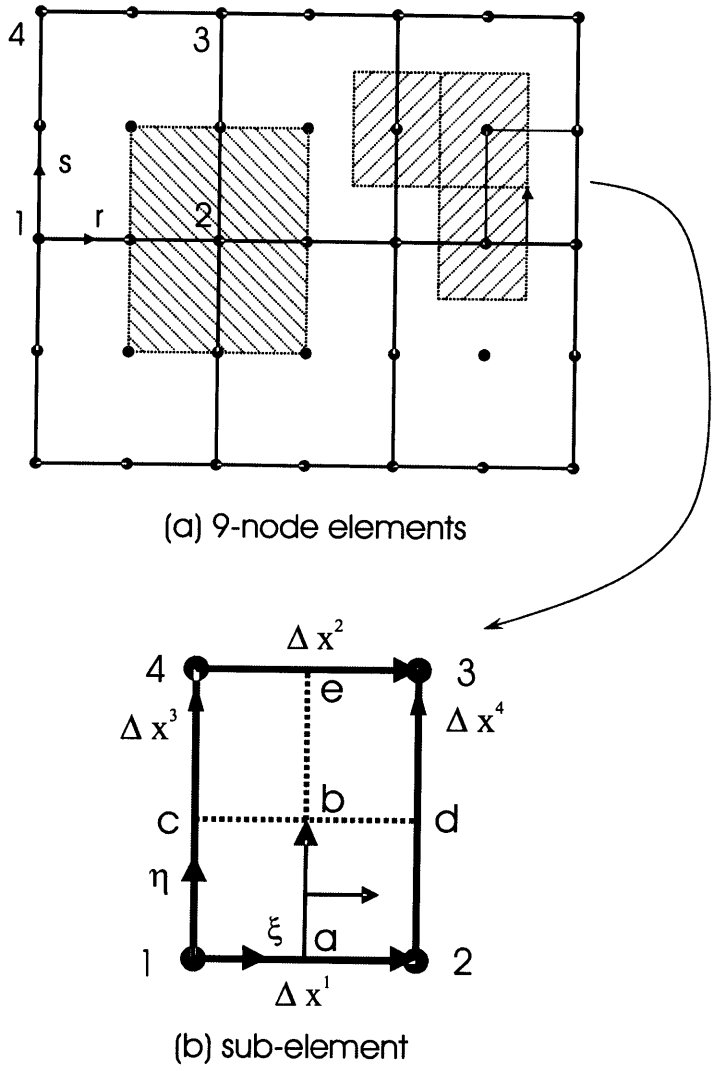

Figure 4-2: 9-node elements and a sub-element in isoparametric coordinates

$$
\begin{aligned}
h_1^u &= (1-\xi)(1-\eta) \\
h_2^u &= \xi(1-\eta) \\
h_3^u &= \xi\eta \\
h_4^u &= (1-\xi)\eta
\end{aligned}
\tag{4.6}
$$

with $0 \leq \xi, \eta \leq 1$.

Similarly, the trial functions in the space P_h are given in each element as,

$$
\begin{bmatrix} h_1^p & h_4^p \\ h_2^p & h_3^p \end{bmatrix} = \begin{bmatrix} 1-r \\ r \end{bmatrix} \begin{bmatrix} 1-s & s \end{bmatrix} \tag{4.7}
$$

or

$$
\begin{aligned}
h_1^p &= (1-r)(1-s) \\
h_2^p &= r(1-s) \\
h_3^p &= rs \\
h_4^p &= (1-r)s
\end{aligned}
\tag{4.8}
$$

with $0 \leq r, s \leq 1$.

The trial functions in V_h are defined using the flow conditions along each side of the sub-element. The functions are, for the flux through ab (Fig. 4-2),

$$
\begin{bmatrix} h_1^v & h_4^v \\ h_2^v & h_3^v \end{bmatrix} = \left(\begin{bmatrix} 1-x^1 & 1-x^2 \\ x^1 & x^2 \end{bmatrix} \begin{bmatrix} 1-\eta \\ \eta \end{bmatrix} \right) \begin{bmatrix} 1-\eta & \eta \end{bmatrix} \tag{4.9}
$$

or

$$
\begin{aligned}
h_1^v &= (1-x^1)(1-\eta)^2 + (1-x^2)(1-\eta)\eta \\
h_2^v &= x^1(1-\eta)^2 + x^2(1-\eta)\eta \\
h_3^v &= x^1(1-\eta)\eta + x^2\eta^2 \\
h_4^v &= (1-x^1)(1-\eta)\eta + (1-x^2)\eta^2
\end{aligned}
\tag{4.10}
$$

with

$$
x^k = \frac{e^{q^k\xi} - 1}{e^{q^k} - 1}\ , \quad q^k = \frac{\rho \bar{\mathbf{u}}_h^k \cdot \Delta \mathbf{x}^k}{\mu} \tag{4.11}
$$

where $\bar{\mathbf{u}}_h^k \in U_h$ and is the velocity at the center of the sides considered ($\xi = \frac{1}{2}$ and $\eta = 0, 1$ for $k = 1, 2$ respectively).

To demonstrate these functions in more details, functions x^1 and $1 - x^1$ are shown in Fig 4-3 for three different values of $q^1 = 10$, $q^1 = 0$ and $q^1 = 200$.

As we see in figure 4-3 for the case $q^1 = 0$, when q^k goes to zero, the x^k function approaches ξ , and h_j^v functions approach the linear functions h_j^u .

Note that h_j^v functions for the flux through ab in Fig 4-2 for example, are exponential functions in the direction of the flow and linear in the other direction (functions x^k and $1 - x^k$ are interpolated linearly for the other direction). h_1^v is, for example,

$$
h_1^v = \begin{cases} 1 - x^1 & \text{for} \quad 0 \le \xi \le 1.0, \eta = 0 \\ (1-\eta) & \text{for} \quad 0 \le \eta \le 1.0, \xi = 0 \end{cases} \tag{4.12}
$$

Analogously, the h_j^v functions are defined for the flux through bc as,

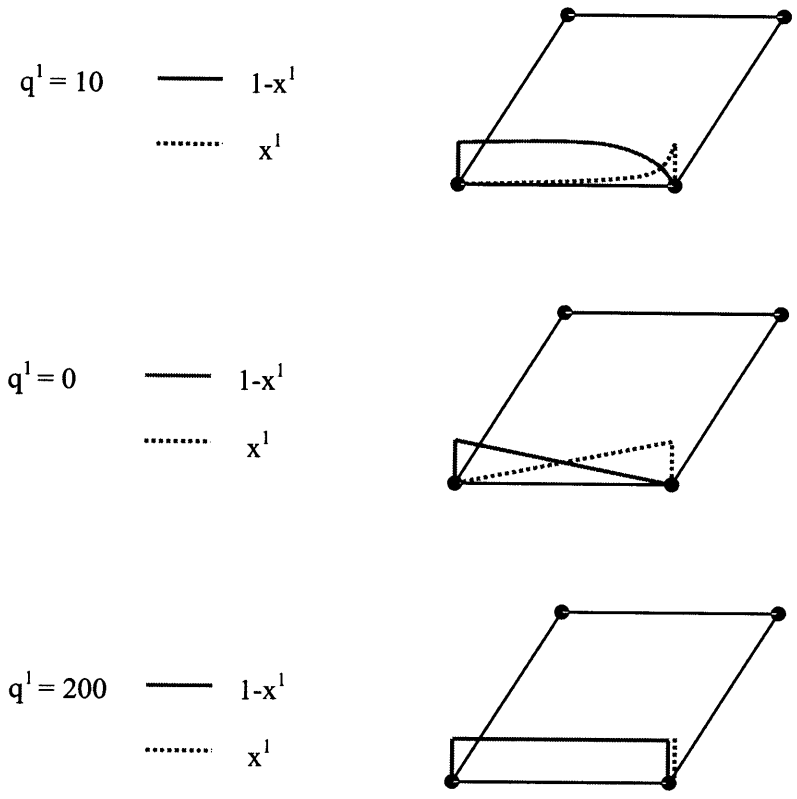

Figure 4-3: The demonstration of x^1 and $1 - x^1$ functions for the flux through ab for the three different values of $q^1 = 10$, $q^1 = 0$ and $q^1 = 200$

$$
\begin{aligned}
h_1^v &= (1-x^3)(1-\xi)^2 + (1-x^4)(1-\xi)\xi \\
h_2^v &= (1-x^3)(1-\xi)\xi + (1-x^4)\xi^2 \\
h_3^v &= x^3(1-\xi)\xi + x^4\xi^2 \\
h_4^v &= x^3(1-\xi)^2 + x^4(1-\xi)\xi
\end{aligned}
\tag{4.13}
$$

with

$$
x^k = \frac{e^{q^k\eta} - 1}{e^{q^k} - 1}\,, \quad q^k = \frac{\rho \bar{\mathbf{u}}_h^k \cdot \Delta \mathbf{x}^k}{\mu} \tag{4.14}
$$

where $\bar{\mathbf{u}}_h^k \in U_h$ and is the velocity at the center of the sides considered ($\eta = \frac{1}{2}$ and $\xi = 0, 1$ for $k = 3, 4$ respectively). .

Note that the trial functions h_j^v satisfy the requirement $\sum h_j^v = 1$.

The elements in the space Q_h are step functions. Referring to Fig. 4-2(a), we have, at node 2, for example,

$$
h_2^q = \begin{cases} 1 & \text{for } (r,s) \in [\frac{1}{2}\,, 1] \times [0, \frac{1}{2}\,] \\ 0 & \text{elsewhere} \end{cases} \tag{4.15}
$$

Similarly, the weight functions in the space W_h are also step functions. Considering the sub-element shown in Fig. 4-2(b), at node 1, for example,

$$
h_2^w = \begin{cases} 1 & \text{for } (\xi,\eta) \in [0, \frac{1}{2}\,] \times [0, \frac{1}{2}\,] \\ 0 & \text{elsewhere} \end{cases} \tag{4.16}
$$

Then, the velocities $\mathbf{u}_h$, $\mathbf{v}_h$ (in each sub-element) and the pressure p_h (in each element) , interpolated with the trial functions in U_h, V_h and P_h respectively, are

$$\begin{aligned}
\mathbf{u}_h &= \sum_{i=1}^{4} h_i^u \ \mathbf{v}_{hi} \\
\mathbf{v}_h &= \sum_{i=1}^{4} h_i^v \ \mathbf{v}_{hi} \\
p_h &= \sum_{i=1}^{4} h_i^p \ p_{hi}
\end{aligned} \tag{4.17}$$

where $\mathbf{v}_{hi}$ and p_{hi} are the nodal velocity and pressure variables.

We again mention that although two different spaces are defined for the velocities but of course h_i^v and h_i^u functions are defined for the same nodal velocity variables $\mathbf{v}_{hi}$. The idea of using these two different spaces lies in that it is the convective term that for high Reynolds numbers introduces the instability and oscillation in the numerical solution. Hence, the convective term needs to be interpolated exponentially. We replace the convective term ($\rho \ \mathbf{v}_h \mathbf{v}_h$) by ($\rho \ \mathbf{u}_h \mathbf{v}_h$) and we define the interpolation functions to be exponential in V_h and linear in U_h. Another reason is that then the FCBI scheme is also applicable to any other transport equation, for example, the advection-diffusion equation where, in the convective term, the temperature would be interpolated in V_h and the velocity in U_h.

Considering the steady-state condition, equation (4.4) is then,

$$\begin{aligned}
&\int_\Omega w_h \nabla \cdot [\rho \ \mathbf{u}_h \mathbf{v}_h - \boldsymbol{\tau}_h(\mathbf{u}_h, p_h)] \ d\Omega = \mathbf{0} \\
&\int_\Omega q_h \nabla \cdot (\rho \ \mathbf{u}_h) \ d\Omega = 0
\end{aligned} \tag{4.18}$$

Assembling equations 4.18 for all the control volumes in the body, and using the divergence theorem to take these integrals around the control volumes we get

$$\sum \int_S w_h \, \mathbf{n} \cdot [\rho \, \mathbf{u}_h \mathbf{v}_h - \boldsymbol{\tau}_h(\mathbf{u}_h, p_h)] \, dS = \mathbf{0}$$
$$\sum \int_S q_h \, \mathbf{n} \cdot (\rho \, \mathbf{u}_h) \, dS = 0 \tag{4.19}$$

where the momentum and the continuity equations are summed over the control volumes of the velocity points and pressure points respectively, S is the surface of each control volume (that corresponds to the length in two-dimensional problems), $\mathbf{n}$ is the unit normal vector pointing to the outside of the control volume and

$$\boldsymbol{\tau}_h = -p_h \, \mathbf{I} + \mu \, [\nabla \mathbf{u}_h + (\nabla \mathbf{u}_h)^T] \tag{4.20}$$

The flux is then calculated with the interpolated values at the center of the sides of the control volumes. For example, the flux through ab (Fig. 4-2) is obtained as

$$\int_a^b \mathbf{n} \cdot \mathbf{f} \, dS = \mathbf{n} \cdot \bar{\mathbf{f}}(\xi)|_{\xi=1/2, \, \eta=1/4} \, \Delta S_{ab} \tag{4.21}$$

where ΔS_{ab} is the length of ab and

$$\mathbf{f}(\xi) = \rho \, \mathbf{u}_h \mathbf{v}_h + p_h \, \mathbf{I} - \mu \, [\nabla \mathbf{u}_h + (\nabla \mathbf{u}_h)^T] \tag{4.22}$$

in the momentum equation and

$$\mathbf{f}(\xi) = \rho \, \mathbf{u}_h \tag{4.23}$$

in the continuity equation.

Replacing $\mathbf{u}_h$, $\mathbf{v}_h$ and p_h from the equations (4.17) , when w_h and q_h are the unit step functions (for the control volumes of the velocity and pressure points respectively), the corresponding *linearized* finite element matrix equations are,

$$\begin{pmatrix} \mathbf{K}_{\mathbf{v}_x\mathbf{v}_x} & \mathbf{K}_{\mathbf{v}_x\mathbf{v}_y} & \mathbf{K}_{\mathbf{v}_x\mathbf{p}} \\ \mathbf{K}_{\mathbf{v}_y\mathbf{v}_x} & \mathbf{K}_{\mathbf{v}_y\mathbf{v}_y} & \mathbf{K}_{\mathbf{v}_y\mathbf{p}} \\ \mathbf{K}_{\mathbf{p}\mathbf{v}_x} & \mathbf{K}_{\mathbf{p}\mathbf{v}_y} & \mathbf{0} \end{pmatrix} \begin{pmatrix} \Delta\mathbf{v}_x \\ \Delta\mathbf{v}_y \\ \Delta\mathbf{p} \end{pmatrix} = \begin{pmatrix} \mathbf{R}_{\mathbf{v}_x} \\ \mathbf{R}_{\mathbf{v}_y} \\ \mathbf{0} \end{pmatrix} - \begin{pmatrix} \mathbf{F}_{\mathbf{v}_x} \\ \mathbf{F}_{\mathbf{v}_y} \\ \mathbf{F}_{\mathbf{p}} \end{pmatrix} \tag{4.24}$$

where $\Delta\mathbf{v}_x$, $\Delta\mathbf{v}_y$, $\Delta\mathbf{p}$, are the *increments* of the velocity in x direction, velocity in y direction and pressure with respect to the last iteration; $\mathbf{R}_{\mathbf{v}_x}$ and $\mathbf{R}_{\mathbf{v}_y}$ are the discretized load vectors and $\mathbf{F}_{\mathbf{v}_x}$, $\mathbf{F}_{\mathbf{v}_y}$, $\mathbf{F}_{\mathbf{p}}$ contain terms from the linearization process. Using the full Newton-Raphson iteration method, for a mesh of non-distorted elements, we get

$$\begin{aligned}
\mathbf{K}_{\mathbf{v}_x\mathbf{v}_x}(j,i) &= \sum_j w_{hj}\ \mu\ n_x\ \frac{\partial y}{\partial \eta}\ \frac{\partial \xi}{\partial x}\ \overline{(q_i h_i^v - h_{i\xi}^u)} \\
&- \sum_j w_{hj}\ \mu\ n_x\ \frac{\partial y}{\partial \eta}\ \frac{\partial \xi}{\partial x}\ \overline{h_{i\xi}^u} + \sum_j w_{hj}\ \mu\ n_y\ \frac{\partial x}{\partial \xi}\ \frac{\partial \eta}{\partial y}\ \overline{(q_i h_i^v - h_{i\eta}^u)} \\
&+ \sum_j w_{hj}\ \mu\ n_x\ \frac{\partial y}{\partial \eta}\ \frac{\partial \xi}{\partial x}\ [\frac{\partial \overline{(g_m h_m^v - h_{m\xi}^u)}}{\partial (v_{hi})_x}\ (v_{hm})_x] \\
\mathbf{K}_{\mathbf{v}_x\mathbf{v}_y}(j,i) &= -\sum_j w_{hj}\ \mu\ n_y\ \frac{\partial x}{\partial \xi}\ \frac{\partial \xi}{\partial x}\ \overline{h_{i\xi}^u} \\
&+ \sum_j w_{hj}\ \mu\ n_y\ \frac{\partial x}{\partial \xi}\ \frac{\partial \eta}{\partial y}\ [\frac{\partial \overline{(g_m h_m^v - h_{m\xi}^u)}}{\partial (v_{hi})_y}\ (v_{hm})_x] \\
\mathbf{K}_{\mathbf{v}_x\mathbf{p}}(j,i) &= \sum_j w_{hj}\ n_x \frac{\partial y}{\partial \eta}\ \overline{h_i^p}
\end{aligned} \tag{4.25}$$

$$\mathbf{K}_{\mathbf{v}_y\mathbf{v}_x}(j,i) = -\sum_j w_{hj}\ \mu\ n_x\ \frac{\partial y}{\partial \eta}\ \frac{\partial \eta}{\partial y}\ \overline{h^u_{i\eta}}$$

$$+\sum_j w_{hj}\ \mu\ n_x\ \frac{\partial y}{\partial \eta}\ \frac{\partial \xi}{\partial x}\ [\frac{\partial(\overline{g_m h^v_m - h^u_{m\xi}})}{\partial (v_{hi})_x}\ (v_{hm})_y]$$

$$\mathbf{K}_{\mathbf{v}_y\mathbf{v}_y}(j,i) = \sum_j w_{hj}\ \mu\ n_x\ \frac{\partial y}{\partial \eta}\ \frac{\partial \xi}{\partial x}\ (\overline{q_i h^v_i - h^u_{i\xi}})$$

$$-\sum_j w_{hj}\ \mu\ n_y\ \frac{\partial x}{\partial \xi}\ \frac{\partial \eta}{\partial y}\ \overline{h^u_{i\eta}} + \sum_j w_{hj}\ \mu\ n_y\ \frac{\partial x}{\partial \xi}\ \frac{\partial \eta}{\partial y}\ (\overline{q_i h^v_i - h^u_{i\eta}}) \tag{4.26}$$

$$+\sum_j w_{hj}\ \mu\ n_y\ \frac{\partial x}{\partial \xi}\ \frac{\partial \eta}{\partial y}\ [\frac{\partial(\overline{g_m h^v_m - h^u_{m\xi}})}{\partial (v_{hi})_y}\ (v_{hm})_y]$$

$$\mathbf{K}_{\mathbf{v}_y\mathbf{p}}(j,i) = \sum_j w_{hj}\ n_y \frac{\partial x}{\partial \xi}\ \overline{h^p_i}$$

$$\mathbf{K}_{\mathbf{p}\mathbf{v}_x}(j,i) = \sum_j q_{hj}\ n_x\ \frac{\partial y}{\partial s}\ \int h^u_i ds$$

$$\mathbf{K}_{\mathbf{p}\mathbf{v}_y}(j,i) = \sum_j q_{hj}\ n_y\ \frac{\partial x}{\partial r}\ \int h^u_i\ dr \tag{4.27}$$

In these equations, $\overline{f} = 2\int_{\eta_1}^{\eta_2} f\ d\eta$ or $\overline{f} = 2\int_{\xi_1}^{\xi_2} f\ d\xi$ based on the direction of the flux, the velocities are the values calculated at the end of the previous iteration; $(v_{hm})_x = (v_{hm})_x^{l-1}, (v_{hm})_y = (v_{hm})_y^{l-1}$ where the repeated subscript m denotes sum-

mation, the subscripts x and y show the direction of the velocity and the subscript l stands for the iteration number . The terms used in these equations are as follows (for the control volumes which have no sides on the boundary),

- For $\eta_1 = 0$, $\eta_2 = \frac{1}{2}$ (flux through ab)

$$\overline{h^u_{i\xi}} = \frac{1}{4}\begin{bmatrix} -3 & -1 \\ 3 & 1 \end{bmatrix}$$

$$\overline{h^u_{i\eta}} = \frac{1}{2}\begin{bmatrix} -1 & 1 \\ -1 & 1 \end{bmatrix}$$

$$\overline{g_i h^v_i - h^u_{i\xi}} = \mathbf{D}\ \overline{h(\eta)h^T(\eta)} \tag{4.28}$$

$$\overline{h(\eta)h^T(\eta)} = \frac{1}{12}\begin{bmatrix} 7 & 2 \\ 2 & 1 \end{bmatrix}$$

$$\overline{h^p_i} = 2\int_0^{0.5} h^p_i\, d\eta$$

where

$$\mathbf{D} = \begin{bmatrix} B^1 & B^2 \\ -A^1 & -A^2 \end{bmatrix} \tag{4.29}$$

and

$$\begin{cases} A^k = \frac{q^k}{e^{q^k}-1} \\ B^k = A^k + q^k \end{cases} \tag{4.30}$$

- For $\eta_1 = \frac{1}{2}$, $\eta_2 = 1$

$$\overline{h^u_{i\xi}} = \frac{1}{4}\begin{bmatrix} -1 & -3 \\ 1 & 3 \end{bmatrix}$$

$$\overline{h^u_{i\eta}} = \frac{1}{2}\begin{bmatrix} -1 & 1 \\ -1 & 1 \end{bmatrix}$$

$$\overline{g_i h^v_i - h^u_{i\xi}} = \mathbf{D}\ \overline{h(\eta)h^T(\eta)} \tag{4.31}$$

$$\overline{h(\eta)h^T(\eta)} = \frac{1}{12}\begin{bmatrix} 1 & 2 \\ 2 & 7 \end{bmatrix}$$

$$\overline{h^p_i} = 2\int_{0.5}^{1} h^p_i\, d\eta$$

where $\mathbf{D}$ is as equation 4.29.

- For $\xi_1 = 0$, $\xi_2 = \frac{1}{2}$ (flux through bc)

$$\overline{h_{i\eta}^u} = \frac{1}{4} \begin{bmatrix} -3 & 3 \\ -1 & 1 \end{bmatrix}$$

$$\overline{h_{i\xi}^u} = \frac{1}{2} \begin{bmatrix} -1 & -1 \\ 1 & 1 \end{bmatrix}$$

$$\overline{g_i h_i^v - h_{i\eta}^u} = \overline{h(\xi) h^T(\xi)}\ \mathbf{E} \tag{4.32}$$

$$\overline{h(\xi) h^T(\xi)} = \frac{1}{12} \begin{bmatrix} 7 & 2 \\ 2 & 1 \end{bmatrix}$$

$$\overline{h_i^p} = 2 \int_0^{0.5} h_i^p \, d\xi$$

where

$$\mathbf{E} = \begin{bmatrix} B^1 & -A^1 \\ B^2 & -A^2 \end{bmatrix} \tag{4.33}$$

and

$$\begin{cases} A^k = \frac{q^k}{e^{q^k}-1} \\ B^k = A^k + q^k \end{cases} \tag{4.34}$$

- For $\xi_1 = \frac{1}{2}$, $\xi_2 = 1$

$$\overline{h^u_{i\eta}} = \frac{1}{4}\begin{bmatrix} -1 & 1 \\ -3 & 3 \end{bmatrix}$$

$$\overline{h^u_{i\xi}} = \frac{1}{2}\begin{bmatrix} -1 & -1 \\ 1 & 1 \end{bmatrix}$$

$$\overline{g_i h^v_i - h^u_{i\eta}} = \overline{h(\xi)h^T(\xi)}\ \mathbf{E} \tag{4.35}$$

$$\overline{h(\xi)h^T(\xi)} = \frac{1}{12}\begin{bmatrix} 1 & 2 \\ 2 & 7 \end{bmatrix}$$

$$\overline{h^p_i} = 2\int_{0.5}^{1} h^p_i\, d\xi$$

where $\mathbf{E}$ is as equation 4.33.

After the system of equations (4.24) is solved, the velocity and the pressure increments are obtained. The velocities and pressures are then updated as,

$$\begin{aligned} (\mathbf{v}_h)^l_x &= \Delta\mathbf{v}_x + (\mathbf{v}_h)^{l-1}_x \\ (\mathbf{v}_h)^l_y &= \Delta\mathbf{v}_y + (\mathbf{v}_h)^{l-1}_y \\ (\mathbf{p}_h)^l &= \Delta\mathbf{p} + (\mathbf{p}_h)^{l-1} \end{aligned} \tag{4.36}$$

4.3 Fundamental properties of the FCBI procedure

- Using two different spaces U_h and V_h for the velocities

In the FCBI procedure, the convective term (ρ **vv**) in equation (4.1) is replaced

by ($\rho\ \mathbf{u}_h\mathbf{v}_h$) in the weak formulation where $\mathbf{v}_h \in V_h$ and $\mathbf{u}_h \in U_h$ (two different spaces are defined for the velocities but of course the functions in these spaces are defined for the same nodal velocity variables). The idea of using these two different spaces lies in that for high Reynolds numbers it is the convective term which introduces the instability and oscillation in the numerical solution. Hence, the convective term needs to be interpolated exponentially. Therefore, we replace the convective term ($\rho\ \mathbf{v}_h\mathbf{v}_h$) by ($\rho\ \mathbf{u}_h\mathbf{v}_h$) and we define the interpolation functions to be exponential in V_h and linear in U_h. Another reason is that then the FCBI scheme is also applicable to any other transport equation, for example, the advection- diffusion equation where, in the convective term, the temperature would be interpolated in V_h and the velocity in U_h.

- Conservation of the mass and momentum

The traditional finite element methods do not satisfy the mass and momentum conservations. The FCBI procedure is a hybrid of the finite element and finite volume methods; the weak form of the Navier-Stokes equations is satisfied over the control volumes, when the test functions are unit step functions. Hence, the FCBI finite element solution satisfies the mass and momentum conservations for the control volumes.

- Calculating all the integrals around the control volumes

As it was explained earlier, we use the divergence theorem to integrate the weak form of the momentum and continuity equations around the control volumes (Eq. 4.19), and the flux is then calculated with the interpolated values at the center of the sides of the control volumes. This will simplify the calculations and decrease the computational effort.

- Defining the interpolation functions

The main reason the FCBI procedure was proposed as a hybrid of the finite element and finite volume methods, not merely a finite volume method, is that interpolation functions are not defined in the finite volume methods. Defining the

interpolation functions enables us to directly evaluate the derivatives, and set up the Jacobian matrix for the Newton-Raphson iteration method.

4.4 Numerical examples

To study the effectiveness of the FCBI procedure, we consider *the driven cavity flow problem* and *the S-channel flow problem* in this section. The results presented are obtained using the FCBI 9-node elements.

4.4.1 The driven cavity flow problem

The cavity flow problem shown in figure 4-4(a) has occupied attention of the scientific computational community since the pioneering paper of *Burggraf* back in 1966 [8]. In early papers finite difference methods and finite volume methods were used to overcome the difficulty of solving this problem for high Reynolds number flows and to improve the accuracy of the solution. For example, *Gatski et al.* used a velocity-vorticity formulation [13] and *Ghia et al.* used a finite difference method in conjunction with a multigrid procedure [11]. However, the new velocity-vorticity finite volume methods [9], [23] are more stable (up to Re=10,000) than the previous finite difference or finite volume methods but still less stable than some of the upwind finite element methods.

If the uniform mesh of 8×8 elements shown in Fig. 4-4(b) is used (this is a coarse mesh), reasonable results are obtained. Of course when the mesh is refined, more details in the flow could be captured as it is illustrated in figure 4-5. When the Reynolds number is high, there are circulations near the corners, also the flow solution hardly changes from a certain Reynolds number onwards.

The driven cavity flow problem for the uniform mesh of 8×8 elements shown in Fig. 4-4(b) is solved for different Reynolds numbers 1, 100, 10,000 and 1,000,000. The velocity and the pressure solutions are shown in Fig. 4-6 and Fig. 4-7 respectively. Furthermore, in Fig. 4-8 vorticity is plotted for different Re numbers.

To study the effectiveness of the FCBI procedure, the horizontal velocity at the

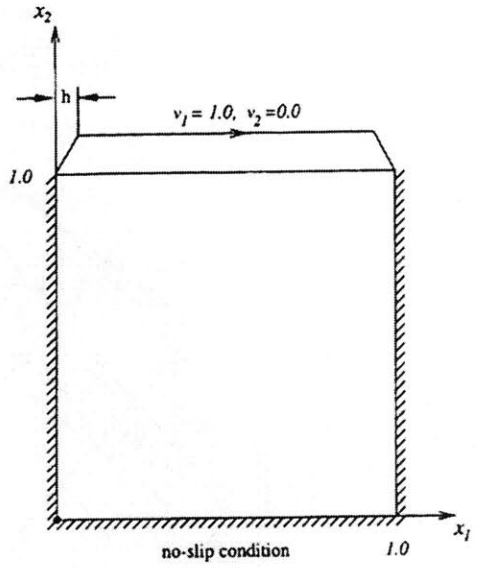

(a)

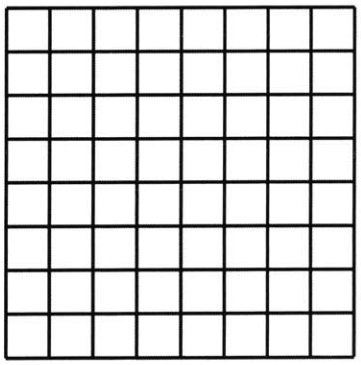

(b)

Figure 4-4: (a) The driven cavity flow problem (b) The uniform mesh of 8×8 elements used

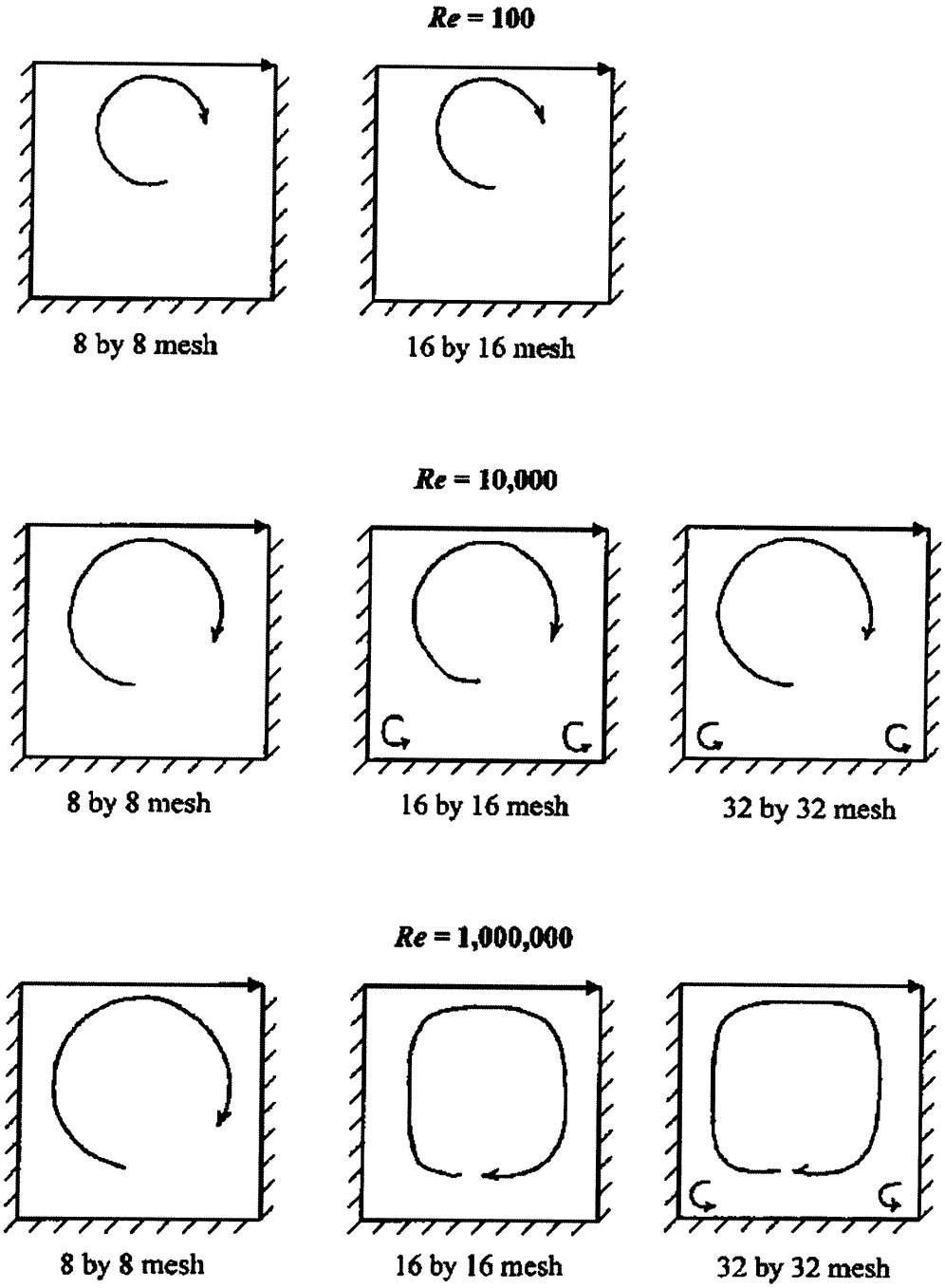

Figure 4-5: Schematics of solutions for the driven cavity flow problem

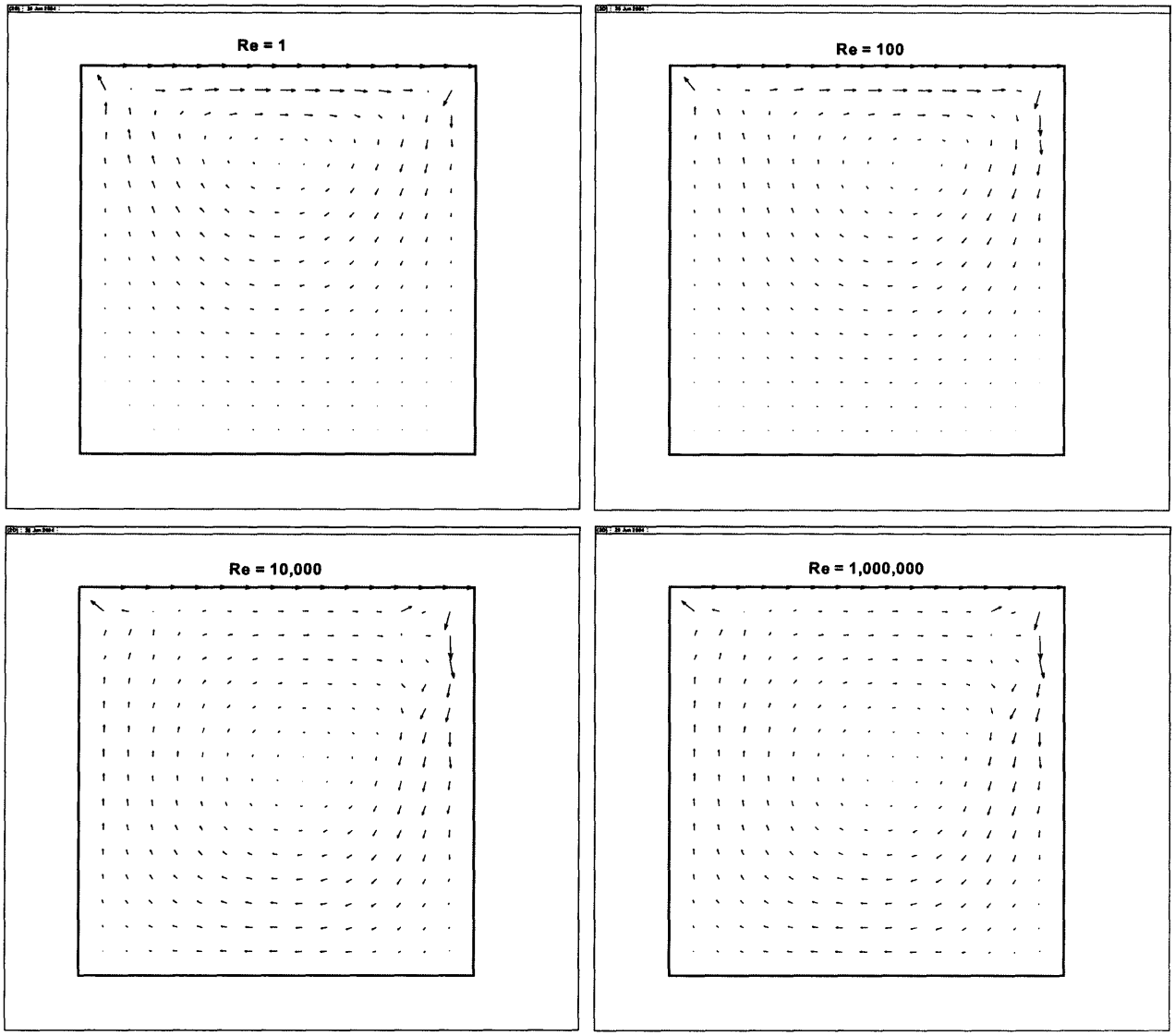

Figure 4-6: The velocity solutions of the driven cavity flow problem for $Re = 1$, 100, 10,000, 1,000,000 for the uniform mesh 8×8 elements

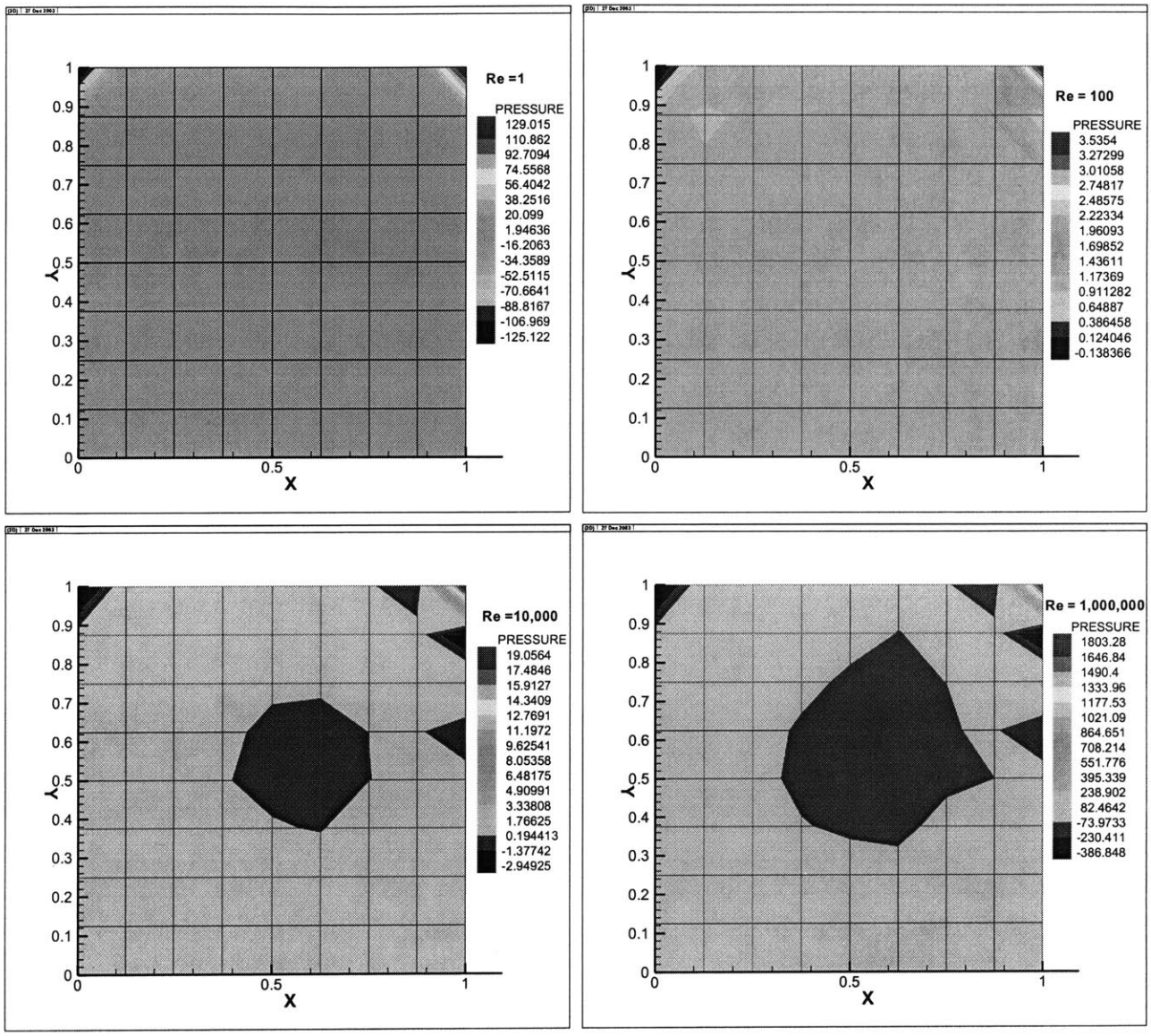

Figure 4-7: The pressure solutions of the driven cavity flow problem for $Re = 1$, 100, 10,000, 1,000,000 for the uniform mesh 8×8 elements

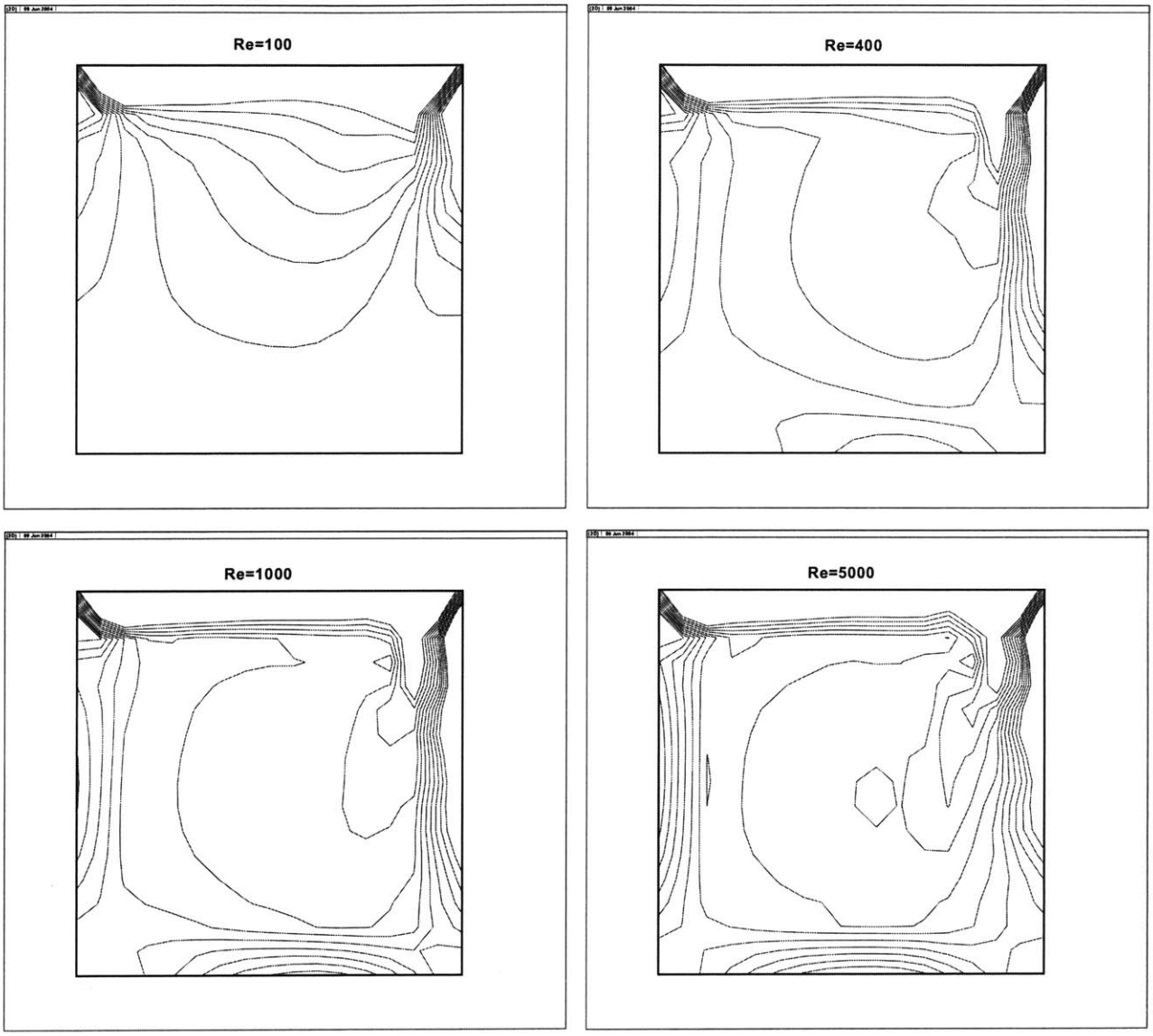

Figure 4-8: Contours of the vorticity for different *Re* numbers for uniform mesh 8× 8 elements. The contour levels shown for each plot are -5.0, -4.0, -3.0, -2.0, -1.0, 0.0, 1.0, 2.0, 3.0, 4.0 and 5.0

vertical centerline, and the vertical velocity at the horizontal centerline are plotted and compared with the solutions of the *Ghia et al.* [11] in figure 4-9 and 4-10 respectively. In these figures, the solution obtained by *Ghia et al.* is shown by "+", this solution is assumed to be the exact solution.

As it is clear from figures 4-9 and 4-10, the FCBI scheme yields reasonable solutions for the driven cavity flow problem (these results are obtained for the coarse mesh of 8× 8 elements). In order to improve the accuracy of the solution, the mesh needs to be refined. Also, close to the boundaries, a finer mesh is required in order to have higher spatial accuracy (a non-uniform mesh).

Note that the FCBI solution obtained for the coarse mesh of 8× 8 elements (16× 16 sub-elements) is stable up to Re=1,000,000 although no upwind parameter is used. Hence, defining two different spaces for the velocities and defining the trial functions in the space V_h to be exponential functions, as it is done in the FCBI procedure, stabilizes the solution even for very high Reynolds numbers.

4.4.2 The S-channel flow problem

The second problem considered in this chapter, is the S-channel flow problem shown in Fig. 4-11 (a). This problem is hard to solve for high Reynolds numbers. If the mesh shown in Fig. 4-11(b) is used (this is a coarse mesh), reasonable results are obtained. Of course when the mesh is refined, more details in the flow could be captured as it is illustrated in figure 4-12. When the Reynolds number is high, there are circulations near the corners, also the flow solution hardly changes from a certain Reynolds number onwards.

The S-channel flow problem for the mesh shown in Fig. 4-11(b) is solved for different Reynolds numbers 1, 100 and 10,000. The velocity and the pressure solutions are presented in Fig. 4-13 and Fig. 4-14 respectively.

Note that the FCBI solution obtained for the coarse mesh used, is stable up to $Re = 10,000$ although no upwind parameter is used. Similar to the cavity flow problem, defining two different spaces V_h and U_h for the velocities and defining the trial functions in the space V_h to be exponential functions, as it is done in the FCBI

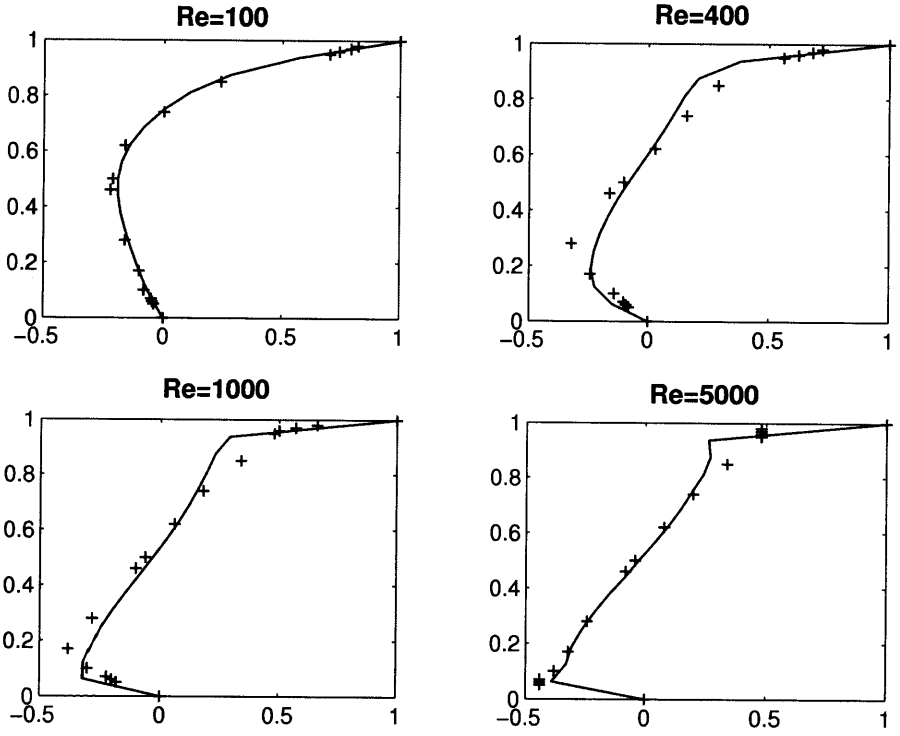

Figure 4-9: The horizontal velocity at the vertical centerline of the cavity for Re = 100, 400, 1000, 5000 when the uniform mesh 8×8 elements is used

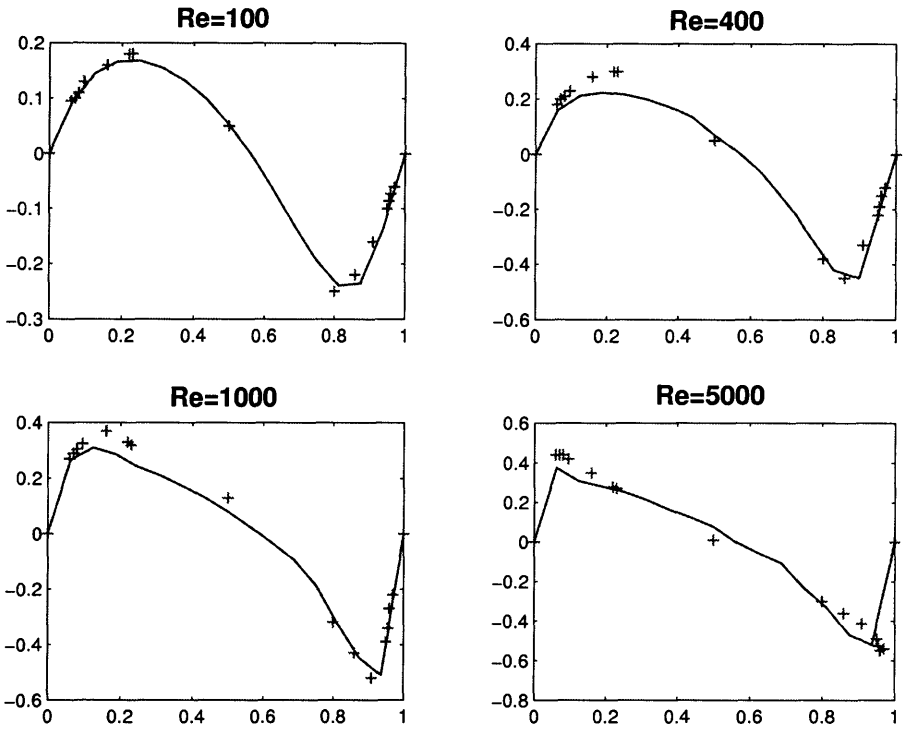

Figure 4-10: The vertical velocity at the horizontal centerline of the cavity for Re = 100, 400, 1000, 5000 when the uniform mesh 8× 8 elements is used

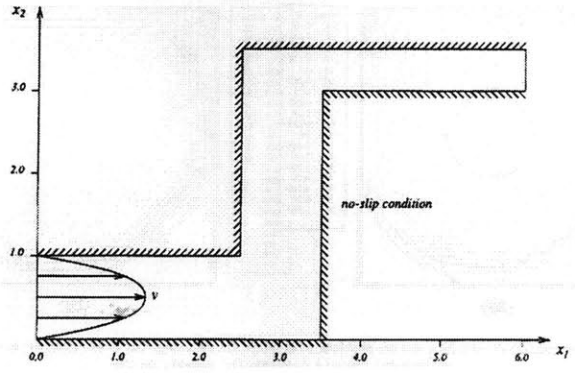

(a)

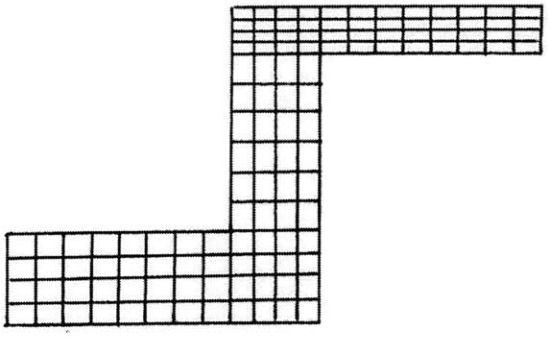

(b)

Figure 4-11: (a) The S-channel flow problem (b) The mesh used

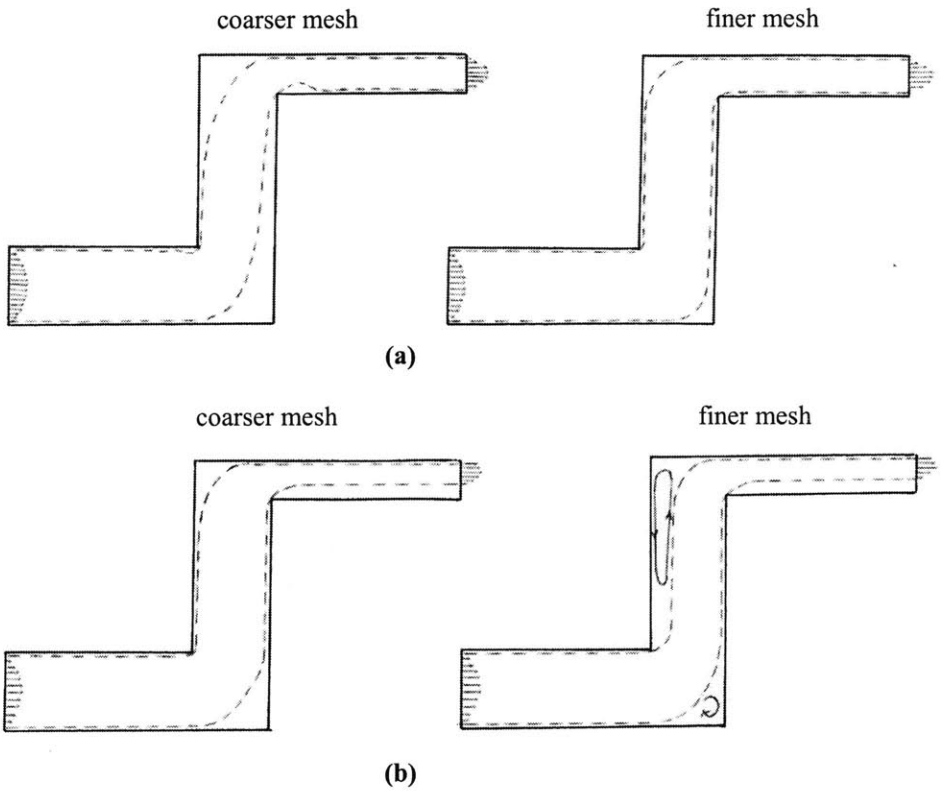

Figure 4-12: Schematics of solutions for the S-channel flow problem (a) $Re = 100$, (b) $Re = 10{,}000$

procedure, stabilizes the solution for high Reynolds numbers.

For further evaluation, nodal pressures along the lower boundary and upper boundary of the S-channel are shown in figure 4-15. These solutions are obtained using the mesh shown in Fig. 4-11(b) and two times finer and coarser meshes when $Re = 100$. The nodal pressures obtained from ADINA program (the FCBI procedure for 4-node elements) are given in figure 4-16. These pressures are the same as the pressure solutions in Fig. 4-15.

4.5 Further study of the FCBI scheme

4.5.1 Stability of the FCBI scheme

In the FCBI procedure, the convective term (ρ **vv**) in equation (4.1) is replaced by (ρ $\mathbf{u}_h\mathbf{v}_h$) in the weak formulation where $\mathbf{v}_h \in V_h$ and $\mathbf{u}_h \in U_h$ (two different spaces are defined for the velocities but of course the functions in these spaces are defined for the same nodal velocity variables). In addition, the trial functions in V_h are exponential functions which are evaluated based on the direction of the flux (the trial functions in U_h are linear functions). The idea of using these two different spaces lies in that it is the convective term which introduces the instability and oscillation in the numerical solution when the Reynolds number is high. Hence, the convective term needs to be interpolated exponentially.

Although no upwind parameter is used to make the FCBI procedure stable, defining two different spaces for the velocities, exponentially interpolating functions in the V_h space and evaluating the pressure interpolation functions such as the *inf-sup* condition is satisfied, stabilizes the FCBI procedure in a natural way.

In this section, the driven cavity flow and the S-channel flow problems are once again considered to compare the stability of the FCBI procedure to some of the upwind techniques in [14].

Table 4.1 compares the stability of the FCBI procedure to the stability of the streamline upwind/Petrov-Galerkin (SUPG) method and the Galerkin/least-squares

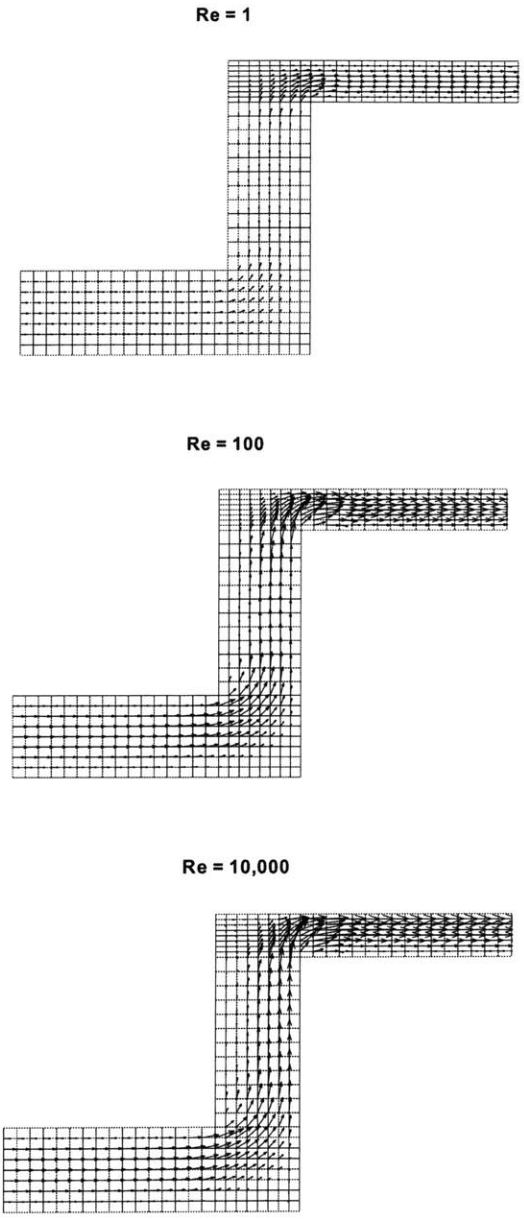

Figure 4-13: The velocity solutions of the S-channel flow problem for $Re = 1, 100, 10,000$ for the mesh shown in figure 4-11 (b)

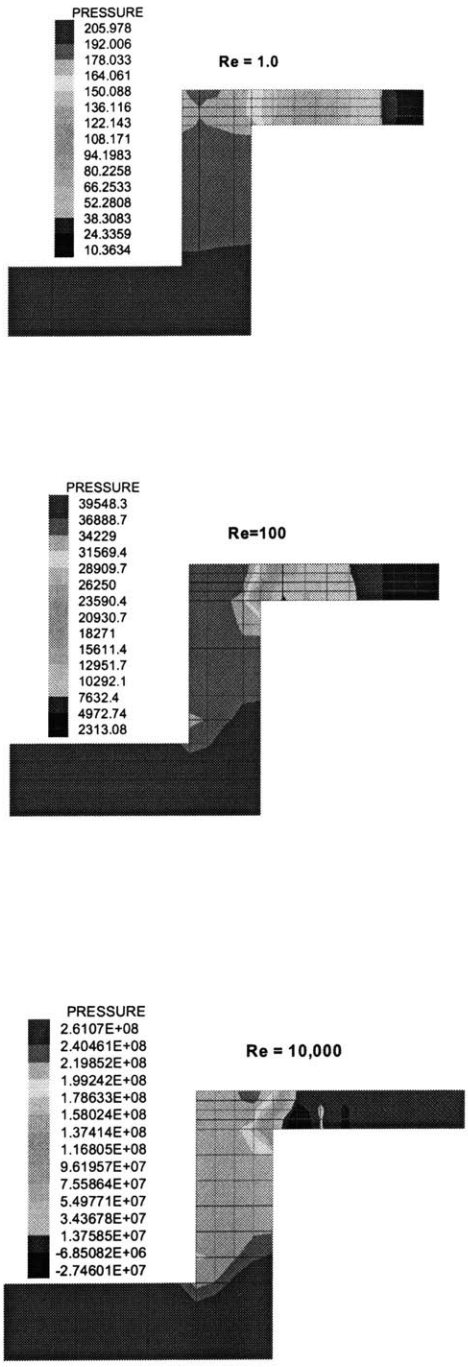

Figure 4-14: The pressure solutions of the S-channel flow problem for $Re = 1, 100, 10, 000$ for the mesh shown in figure 4-11 (b)

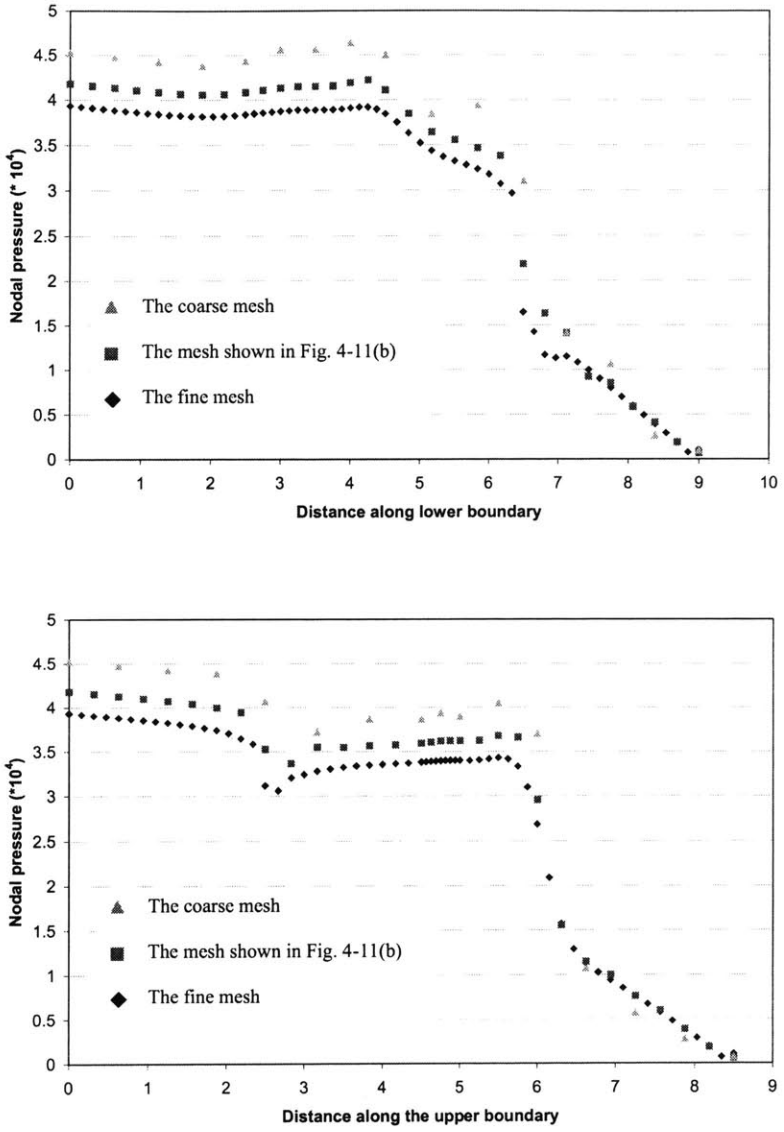

Figure 4-15: Pressure solutions obtained by the FCBI procedure using the mesh shown in Fig. 4-11(b) and the two times finer and coarser meshes when $Re = 100$

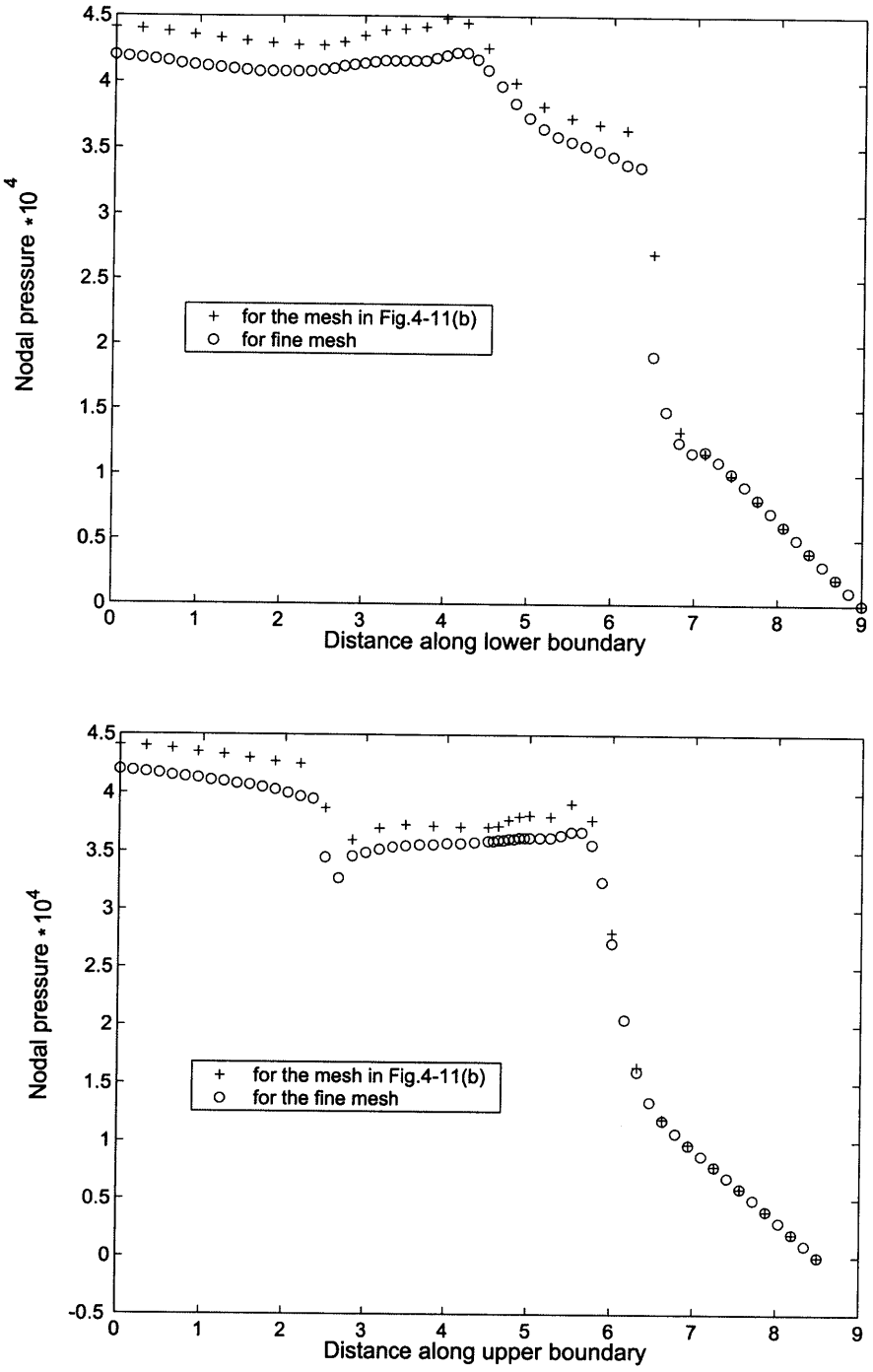

Figure 4-16: Pressure solutions obtained by the ADINA program using the mesh shown in Fig. 4-11(b) and the two times finer mesh when $Re = 100$

(GLS) method. In this table, a uniform mesh of 20×20 elements is used (20×20 sub-elements in the FCBI procedure). The number of iterations required to solve the problem, is also shown for the ADINA program (FCBI 4-node elements).

The S-channel flow problem shown in Fig. 4-11(a) is used as our second example. In Table 4.2, the number of iterations required to solve the problem, are given for the upwind/Petrov-Galerkin (SUPG) method, the Galerkin/least-squares (GLS) method, the FCBI scheme for 9-node elements (each element consists of four 4-node sub-elements) and the ADINA program (FCBI scheme for 4-node elements). In this Table, a mesh of 480 elements is used (120 elements and 480 sub-elements in the FCBI procedure).

To obtain results given in these tables, Newton-Raphson iteration method is used and (*) denotes iteration not converged within the allowable 35 number of iterations. In these tables the convergence tolerance is 10^{-6} for the normalized norms $R_{\mathbf{v}} = \frac{||\Delta \mathbf{v}_h||}{||\mathbf{v}_h||}$ and $R_p = \frac{||\Delta p_h||}{||p_h||}$.

As it is clear in both the driven cavity problem and the S-channel flow problem, the FCBI 9-node and 4-node elements (ADINA) give more stable solutions than the SUPG and GLS methods. The FCBI 4-node elements yield more stable solutions than the 9-node elements but as we see later on in this chapter, the 9-node element is more effective in capturing flow details, velocity and vorticity fields and showing the circulations for high Reynolds numbers. The S-channel flow problem is more sensitive for higher Reynolds numbers since there will be circulations near the corners.

4.5.2 Accuracy of the FCBI scheme

In this section the L^2 and H^1 norms of the velocities and the L^2 norm of the pressure are used to measure the errors in the FCBI method. Of course to study the accuracy and convergence of the FCBI 9-node element, more appropriate posteriori error estimator could be found. The L^2 and H^1 norms of the velocities and L^2 norm of the pressure considered here are as,

Re	**SUPG**	**GLS**	**FCBI**	**ADINA**
400	8	8	8	7
1000	8	8	8	8
2000	7	6	9	8
4000	*	4	9	9
8000		4	10	10
10000		4	10	10
12000		4	10	10
15000		4	11	10
18000		4	11	11
20000		4	11	11
24000		4	11	11
26000		5	11	11
28000		*	12	11
30000			12	12
40000			12	12
45000			16	12
48000			*	12
50000				12
100000				13
1,000,000				15

Table 4.1: Number of iterations required to solve the driven cavity flow problem for different *Re* numbers.

Re	**SUPG**	**GLS**	**FCBI**	**ADINA**
250	8	5	6	7
500	*	6	7	8
750		*	10	9
1000			11	9
1500			12	9
2000			16	9
4000			*	11
7000				12
8000				12
10000				13
15000				14
20000				15
40000				16
50000				*

Table 4.2: Number of iterations required to solve the S-channel flow problem for different *Re* numbers.

$$\| \mathbf{u} - \mathbf{u}_h \|^2_{L^2} = \sum_{over\ sub-elements} \int (u - u_h)^2_x \, dxdy + \sum_{over\ sub-elements} \int (u - u_h)^2_y \, dxdy \tag{4.37}$$

$$\begin{aligned} \| \mathbf{u} - \mathbf{u}_h \|^2_{H^1} = & \sum_{over\ sub-elements} \int (u - u_h)^2_x \, dxdy + \sum_{over\ sub-elements} \int (u - u_h)^2_y \, dxdy \\ & + \sum_{over\ sub-elements} \int (u - u_h)^2_{x,\,x} \, dxdy + \sum_{over\ sub-elements} \int (u - u_h)^2_{x,\,y} \, dxdy \\ & + \sum_{over\ sub-elements} \int (u - u_h)^2_{y,\,x} \, dxdy + \sum_{over\ sub-elements} \int (u - u_h)^2_{y,\,y} \, dxdy \end{aligned} \tag{4.38}$$

$$\| p - p_h \|^2_{L^2} = \sum_{over\ elements} \int (p - p_h)^2 \, dxdy \tag{4.39}$$

where $\mathbf{u}_h \in U_h$ and $p_h \in P_h$.

In these equations, $(\ \cdot\ )_{,\,x}$ and $(\ \cdot\ )_{,\,y}$ are the x and y derivatives, $(u - u_h)_x$ and $(u - u_h)_y$ are the x and y components of $(\mathbf{u} - \mathbf{u}_h)$ respectively where $\mathbf{u}$ is the exact velocity and $\mathbf{u}_h$ is the velocity obtained by the finite element solution. The exact solution is the analytical solution and it is unknown for most of the fluid flow problems. Here, the exact solution is assumed to be the finite element solution obtained using the Galerkin 9-node element (using 9 nodes for the interpolation of the velocities and the 4 corner nodes for the pressure interpolations[1]) with no upwinding for a fine mesh.

To demonstrate solution errors in more details, the driven-cavity flow and the S-channel flow problems in figures 4-4(a) and 4-11(a) are considered again. To plot the convergence curves in the cavity flow problem, the non-uniform meshes of 4×4 elements (Fig. 4-17), 8×8 and 16×16 elements are considered. In the S-channel flow problem the mesh shown in Fig. 4-11(b) and 2 times finer and coarser meshes are considered.

Figures 4-18 and 4-19 illustrate that in the cavity flow problem and the S-channel flow problem, the $\| \mathbf{u} - \mathbf{u}_h \|_{L^2}$, $\| \mathbf{u} - \mathbf{u}_h \|_{H^1}$ and $\| p - p_h \|_{L^2}$ norms converge when the mesh is refined. In these figures, the solid line represents the solutions obtained using the FCBI 9-node elements. The solution obtained using the Galerkin 9-node elements and the solution obtained by the ADINA program (for FCBI 4-node elements) are also given.

In both problems, from the convergence curves we observe that the pressure errors are larger using the FCBI elements (both 9-node elements and 4-node elements). However, more accurate pressures are obtained in the L^2 norm using the FCBI 9-node elements than the FCBI 4-node elements. In the driven cavity flow problem, velocity errors are almost the same in the L^2 and H^1 norms using the FCBI 9-node

[1] Also referred to as the Taylor-Hood, Q9/Q4, or 9/4-c element [1]

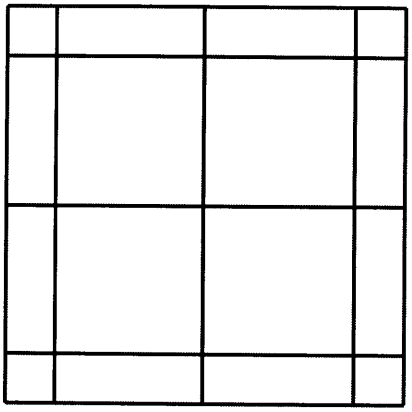

Figure 4-17: The non-uniform mesh of 4×4 9-node elements used

elements and the FCBI 4-node elements. Note that the solution using the Galerkin 9-node elements is not stable for the coarsest mesh and is not included in figure 4-18. In the S-channel flow problem, velocities are better predicted using the FCBI 9-node elements than the FCBI 4-node elements in both L^2 and H^1 norms. The solution obtained by the ADINA program (using FCBI 4-node elements) for the coarsest mesh is not accurate enough and therefore not included in figure 4-19.

Since in the FCBI procedure two different spaces V_h and U_h are used to define the velocities, and the trial functions in V_h are exponential functions, the rate of the convergence of the H^1 and L^2 norms (the slope of the given lines in figures 4-18 and 4-19 corresponding to the FCBI 9-node and 4-node elements) is less than the rate of the convergence using the Galerkin 9-node elements. In other words, although defining the trial functions in V_h as exponential functions makes the solution to be too stable (too much upwinding), it decreases the rate of the convergence of the H^1 and L^2 norms.

- Concluding remarks on the numerical results

Of course we can only draw partial conclusions from these preliminary numerical results since, in particular, other fluid problems need to be considered for compre-

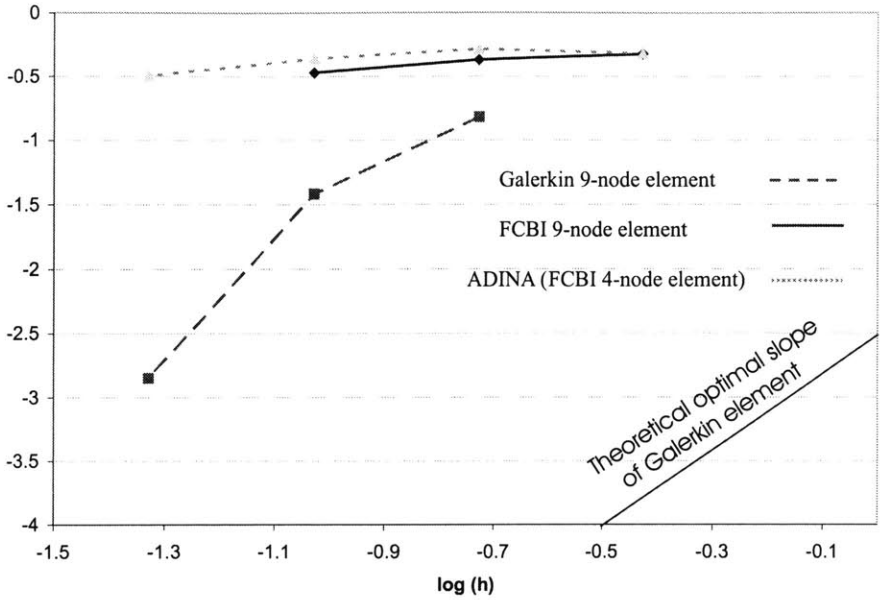

Fig 4.18 (a)

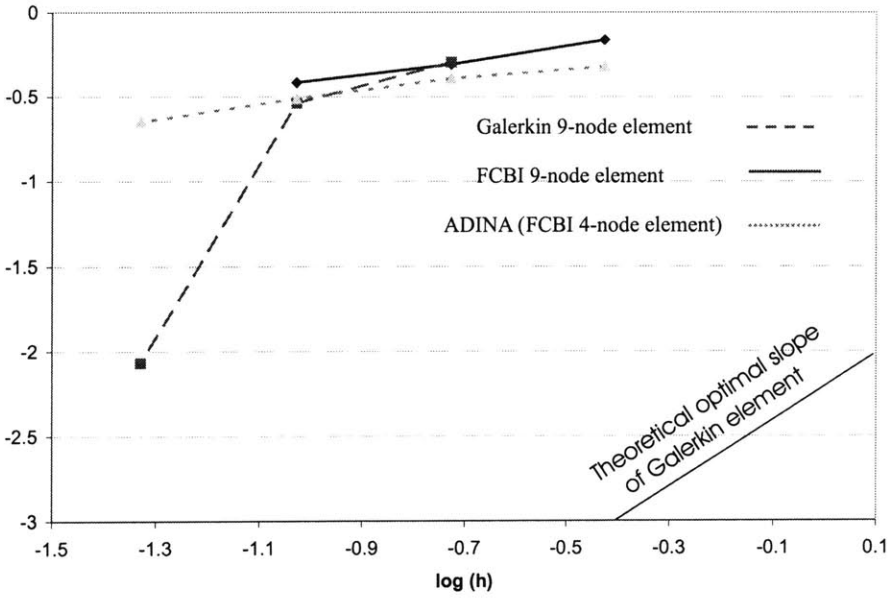

Fig 4.18 (b)

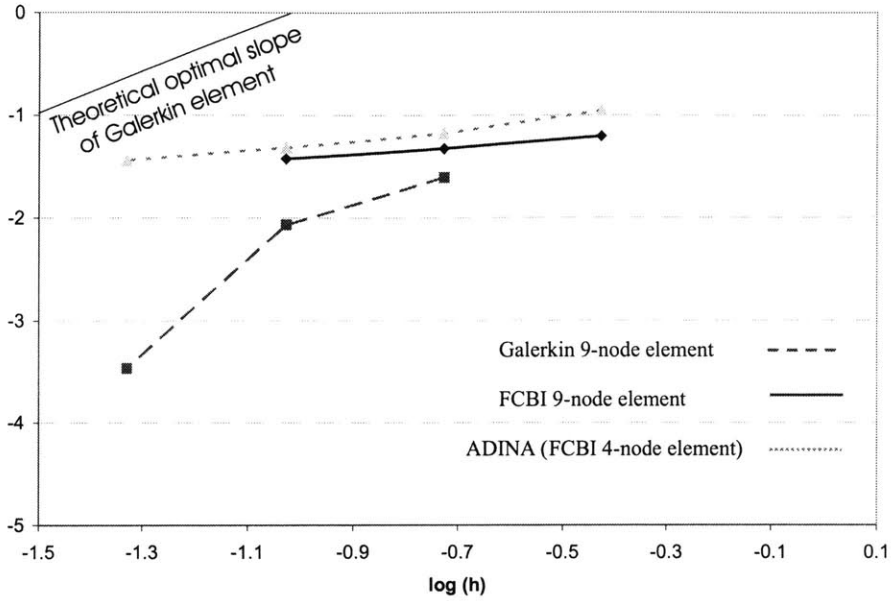

Fig 4.18 (c)

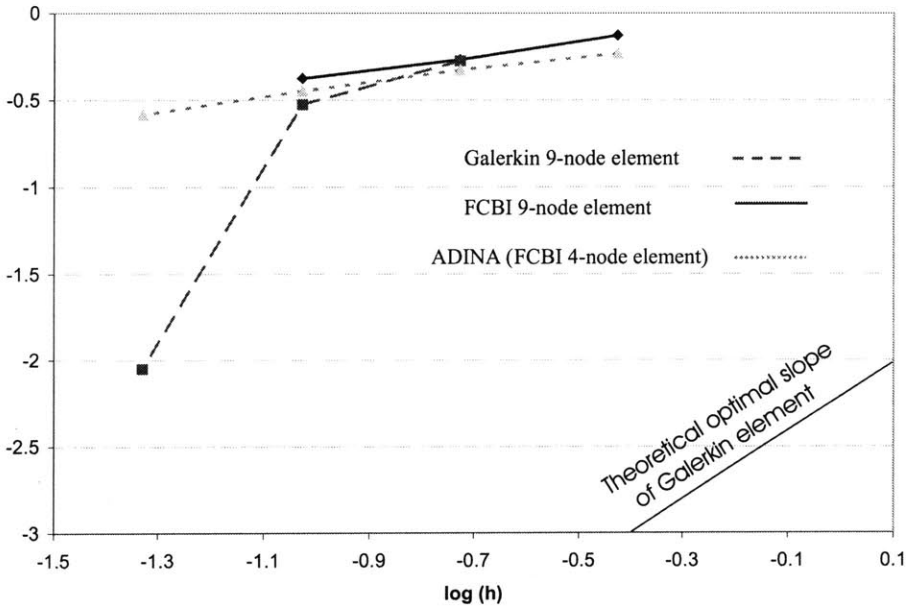

Fig 4.18 (d)

Figure 4-18: Comparison of the FCBI 9-node elements, FCBI 4-node elements and the Galerkin 9-node elements for the driven cavity flow problem (Re=1000). In this figure, the x coordinate represents log h when h is the element size and the y coordinate for each case is a) $log\ \frac{\|\mathbf{u}-\mathbf{u}_h\|_{L^2}}{\|\mathbf{u}\|_{L^2}}$, b) $log\ \frac{\|\mathbf{u}-\mathbf{u}_h\|_{H^1}}{\|\mathbf{u}\|_{H^1}}$, c) $log\ \frac{\|p-p_h\|_{L^2}}{\|p\|_{L^2}}$, d) $log\ (\frac{\|\mathbf{u}-\mathbf{u}_h\|_{H^1}}{\|\mathbf{u}\|_{H^1}} + \frac{\|p-p_h\|_{L^2}}{\|p\|_{L^2}})$.

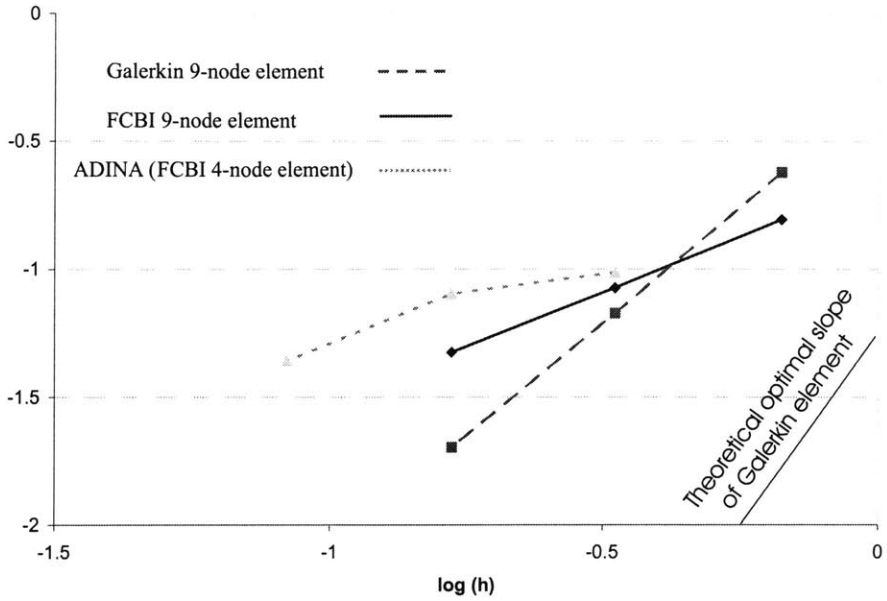

Fig 4.19 (a)

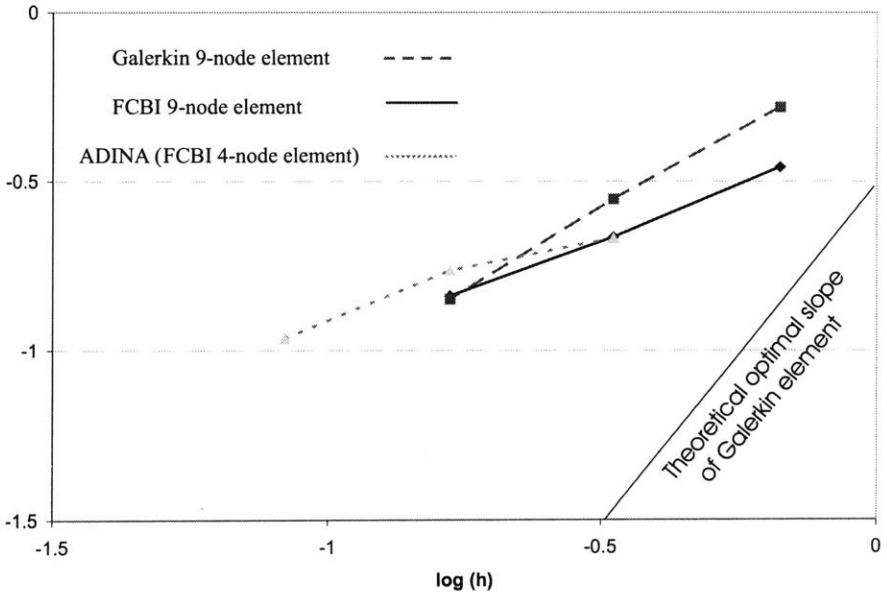

Fig 4.19 (b)

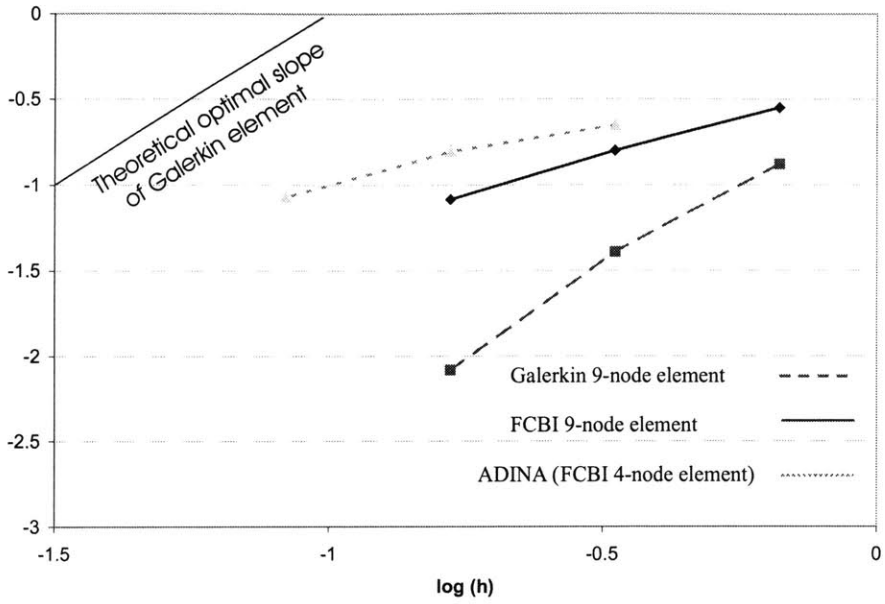

Fig 4.19 (c)

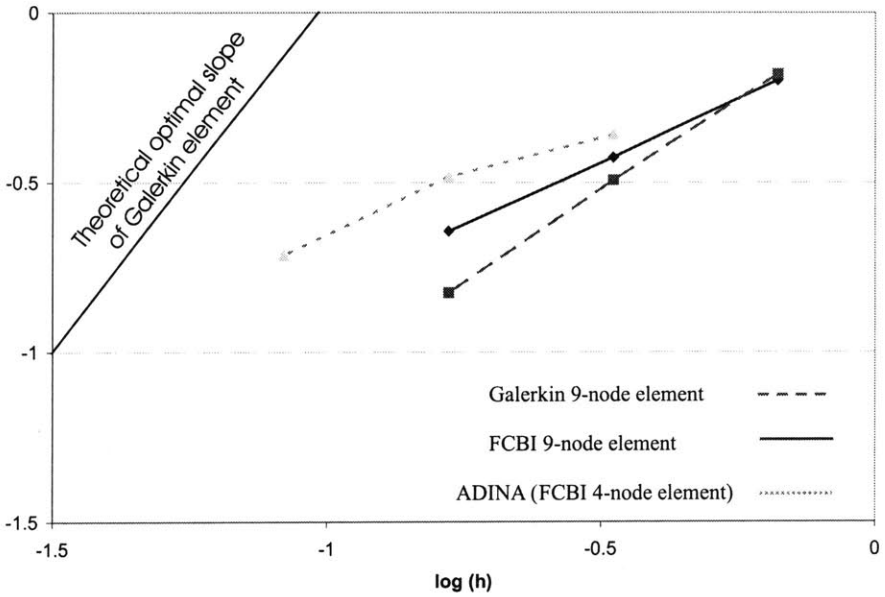

Fig 4.19 (d)

Figure 4-19: Comparison of the FCBI 9-node elements, FCBI 4-node elements and the Galerkin 9-node elements for the S-channel flow problem (Re=100). In this figure, the x coordinate represents log h when h is the element size and the y coordinate for each case is a) $log\ \frac{\|\mathbf{u}-\mathbf{u}_h\|_{L^2}}{\|\mathbf{u}\|_{L^2}}$, b) $log\ \frac{\|\mathbf{u}-\mathbf{u}_h\|_{H^1}}{\|\mathbf{u}\|_{H^1}}$, c) $log\ \frac{\|p-p_h\|_{L^2}}{\|p\|_{L^2}}$, d) $log\ (\frac{\|\mathbf{u}-\mathbf{u}_h\|_{H^1}}{\|\mathbf{u}\|_{H^1}} + \frac{\|p-p_h\|_{L^2}}{\|p\|_{L^2}})$.

hensiveness.

From these numerical results, the FCBI 9-node element (consists of four 4-node sub-elements) appears to be stable for high Reynolds numbers although no upwind parameter is used, and predict the solution reasonably accurate.

Of course, in order for the solution errors to be small, the mesh needs to be refined. However, the convergence curves display a small rate of convergence when the FCBI 9-node element is used.

Chapter 5

A new FCBI 9-node element

The analysis of fluid flows with structural interactions has captured much attention during the recent years. Such analysis is performed considering the solution of the Navier-Stokes fluid flows fully coupled to the non-linear structural response. However, a fully coupled fluid flow structural interaction analysis can be computationally very expensive. The cost of the solution is, roughly, proportional to the number of nodes or grid points used to discretize the fluid and the structure [1].

In order for interaction effects to be significant, the structure is usually thin and can be represented as a shell, hence not too many grid points are required. The large number of grid points and consequently number of equations in fluid flow structural interaction problems (FSI) is due to the representation of the fluid domain. For high Reynolds number fluid flows, to have a stable solution, more grid points are required. In order to decrease the number of grid points in the fluids (using a coarser mesh) and still have a stable solution, the flow-condition-based interpolation (FCBI) procedure was introduced [2], [3], [4].

As it was already mentioned in chapter 4, the FCBI procedure is a hybrid of the finite element and the finite volume methods. The test functions for both the continuity and the momentum equations are step functions and the governing equations are written over control volumes. Hence, the mass and momentum conservations are satisfied locally. Ideally any numerical solution for fluids should yield stable solutions for low and high Reynolds number flows with reasonable accuracy. Of course, when

fine meshes are used, more details of the flow are captured and the level of accuracy is higher. Ideally, we want our numerical scheme to yield still stable solutions with reasonable accuracy when coarse meshes are used. In particular, this will decrease the required number of grid points and elements in the fluid phase in the fluid-structure interaction problems.

In order to ensure that using the coarse meshes to represent the fluid yields an accurate enough structural response, the solution errors need to be controlled and measured. The "goal-oriented error estimation" might be applied to assess the error in the quantities of interest in the structure. In fluid flow structural interaction analysis, it is ideal to use an FCBI solution scheme in rather coarse meshes together with "goal-oriented error estimation" to control the error of the solution in the structural response [12]. In all the FSI problems considered in [12], the flow problems are solved using the 4-node FCBI elements available in ADINA. The error estimate then uses the fluid flow approximation obtained with a 9-node Galerkin finite element (using the 9 nodes for the velocities and the 4 corner nodes for the pressure interpolations[1]) and the same mesh (i.e., with the same number of elements) as used with the 4-node FCBI elements. However, Galerkin 9-node elements are unable to give stable solutions with coarse meshes for high Reynolds number flows. Hence, it would be ideal to use 9-node FCBI elements with much better stability and almost the same accuracy as Galerkin 9-node elements.

The earlier published 9-node FCBI elements, consisting of four 4-node sub-elements, are illustrated and studied in chapter 4. In this chapter, it became clear that these FCBI 9-node elements are more stable than the Galerkin 9-node elements. However, the Galerkin 9-node elements give more accurate solutions with a higher rate of convergence. Hence, in this chapter we propose a new FCBI 9-node element that obtains more accurate solutions than the earlier proposed FCBI elements. The new 9-node elements do not obtain the solution as accurate as the Galerkin 9-node elements but the solution is stable for much higher Reynolds numbers (than the Galerkin 9-node elements), and accurate enough to be used to find the structural responses.

[1]Also referred to as the Taylor-Hood, Q9/Q4, or 9/4-c element [1]

5.1 Fluid flow discretization

In chapter 4, we already introduced and studied the earlier published FCBI 9-node element consisting of four 4-node sub-elements. In this section we present a new FCBI 9-node element.

As we already mentioned in chapter 4, in the FCBI scheme, we use a Petrov-Galerkin variational formulation with subspaces V_h, U_h and W_h of V, and P_h and Q_h of P of the Navier-Stokes equations. The formulation used is:

Find $\mathbf{v}_h \in V_h$, $\mathbf{u}_h \in U_h$, $p_h \in P_h$ such that for all $w_h \in W_h$ and $q_h \in Q_h$

$$\int_\Omega w_h \left[\frac{\partial \rho \mathbf{u}_h}{\partial t} + \nabla \cdot (\rho \mathbf{u}_h \mathbf{v}_h - \boldsymbol{\tau}(\mathbf{u}_h, p_h)) \right] d\Omega = 0 \tag{5.1}$$

$$\int_\Omega q_h \nabla \cdot (\rho \mathbf{u}_h) d\Omega = 0 \tag{5.2}$$

To define the spaces used in the formulation, consider Fig. 5-1, where we show the new element in its natural coordinate system. This element is defined by nine nodes for the interpolation of the velocities and four corner nodes to interpolate the pressure. Let us mention that in chapter 4, each 9-node element consists of four 4-node sub-elements and in each sub-element the four corner nodes are used to interpolate the velocities $\mathbf{v}_h$ and $\mathbf{u}_h$. The pressure is interpolated by the four corner points in each element. Hence, for the definition of the spaces V_h, U_h and P_h, we referred to the sub-element and element respectively. Here, for the new 9-node element, spaces V_h, U_h and P_h are defined for the element.

The trial functions in U_h are

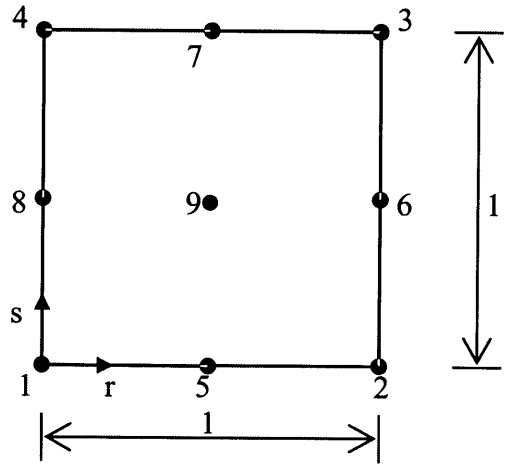

(a)

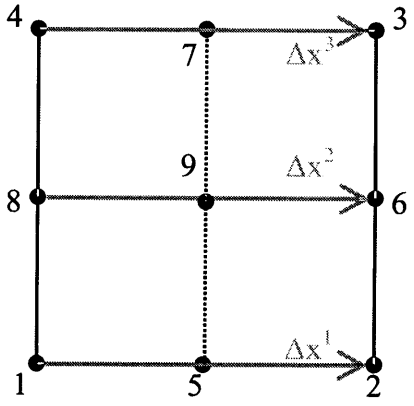

(b)

Figure 5-1: The new FCBI 9-node element (a) The element in its isoparametric coordinates, (b) Definition of $\Delta \mathbf{x}^k$ for the flux through 5-7

$$
\begin{aligned}
h_1^u &= (1-r)(1-s) - \frac{1}{2}\, h_5^u - \frac{1}{2}\, h_8^u - \frac{1}{4}\, h_9^u \\
h_2^u &= r(1-s) - \frac{1}{2}\, h_5^u - \frac{1}{2}\, h_6^u - \frac{1}{4}\, h_9^u \\
h_3^u &= rs - \frac{1}{2}\, h_6^u - \frac{1}{2}\, h_7^u - \frac{1}{4}\, h_9^u \\
h_4^u &= (1-r)s - \frac{1}{2}\, h_7^u - \frac{1}{2}\, h_8^u - \frac{1}{4}\, h_9^u \\
h_5^u &= 4r(1-r)(1-s) - \frac{1}{2}\, h_9^u \\
h_6^u &= 4rs(1-s) - \frac{1}{2}\, h_9^u \\
h_7^u &= 4rs(1-r) - \frac{1}{2}\, h_9^u \\
h_8^u &= 4s(1-r)(1-s) - \frac{1}{2}\, h_9^u \\
h_9^u &= 16rs(1-r)(1-s)
\end{aligned}
\tag{5.3}
$$

with $0 \leq r, s \leq 1$. These are the standard Lagrangian interpolations [1].

Similarly, an element in the space P_h is given by

$$
\begin{aligned}
h_1^p &= (1-r)(1-s) \\
h_2^p &= r(1-s) \\
h_3^p &= rs \\
h_4^p &= (1-r)s
\end{aligned}
\tag{5.4}
$$

The trial functions in V_h are defined using the flow conditions along each side of the element. The functions are, for the flux through 5-7 (refer to Fig. 5-1)

$$
\begin{aligned}
h_1^v &= f^1(1-2s)^2(1-s)^2 + g^1 4s(1-2s)(1-s)^2 - \phi^1 s(1-2s)^2(1-s) \\
h_2^v &= f^3(1-2s)^2(1-s)^2 + g^3 4s(1-2s)(1-s)^2 - \phi^3 s(1-2s)^2(1-s) \\
h_3^v &= -f^3 s(1-2s)^2(1-s) - g^3 4s^2(1-2s)(1-s) + \phi^3 s^2(1-2s)^2 \\
h_4^v &= -f^1 s(1-2s)^2(1-s) - g^1 4s^2(1-2s)(1-s) + \phi^1 s^2(1-2s)^2 \\
h_5^v &= f^2(1-2s)^2(1-s)^2 + g^2 4s(1-2s)(1-s)^2 - \phi^2 s(1-2s)^2(1-s) \\
h_6^v &= f^3 4s(1-2s)(1-s)^2 + g^3 16s^2(1-s)^2 - \phi^3 4s^2(1-2s)(1-s) \\
h_7^v &= -f^2 s(1-2s)^2(1-s) - g^2 4s^2(1-2s)(1-s) + \phi^2 s^2(1-2s)^2 \\
h_8^v &= f^1 4s(1-2s)(1-s)^2 + g^1 16s^2(1-s)^2 - \phi^1 4s^2(1-2s)(1-s) \\
h_9^v &= f^2 4s(1-2s)(1-s)^2 + g^2 16s^2(1-s)^2 - \phi^2 4s^2(1-2s)(1-s)
\end{aligned}
\tag{5.5}
$$

with

$$
0 \le r \le 0.5 : \begin{cases} f^1 = 1 - \frac{(e^{q^1 r}-1)}{(e^{0.5q^1}-1)} \\ f^3 = \frac{-0.5q^1}{(e^{0.5q^1}-1)}\,(1-2r)\frac{(e^{q^1 r sign(q^1)}-1)}{(e^{0.5q^1 sign(q^1)}-1)} \\ f^2 = 1 - f^1 - f^3 \end{cases} \tag{5.6}
$$

$$
0.5 \le r \le 1 : \begin{cases} f^1 = \frac{0.5q^1 e^{0.5q^1}}{(e^{0.5q^1}-1)}\,(1-2r)\frac{(e^{q^1(1-r)}-1)}{(e^{0.5q^1}-1)} \\ f^3 = \frac{(e^{q^1(r-0.5)}-1)}{(e^{0.5q^1}-1)} \\ f^2 = 1 - f^1 - f^3 \end{cases} \tag{5.7}
$$

Analogously, the g and ϕ functions are defined for q^2 and q^3 respectively where the q^k coefficients are

$$
q^k = \frac{\rho \bar{\mathbf{u}}_h^k \cdot \Delta \mathbf{x}^k}{\mu} \tag{5.8}
$$

where $\bar{\mathbf{u}}_h^k \in U_h$ and is the velocity at the center of $\Delta \mathbf{x}^k$ (Fig. 5-1). Similarly, the h_j^v functions are constructed for the flux through 8-6 and so on.

To demonstrate these functions in more details, the f, g and ϕ functions are shown in Fig 5-2 for three values $q^1 = 10$, $q^2 = 0$ and $q^3 = 200$ respectively. As it was mentioned earlier, for the flux through 5-7 (Fig 5-1), f^1, f^2 and f^3 are exponential functions of q^1 and r as given in equations (5.6) and (5.7). Similarly, g and ϕ functions are exponential functions of q^2 and r and q^3 and r respectively.

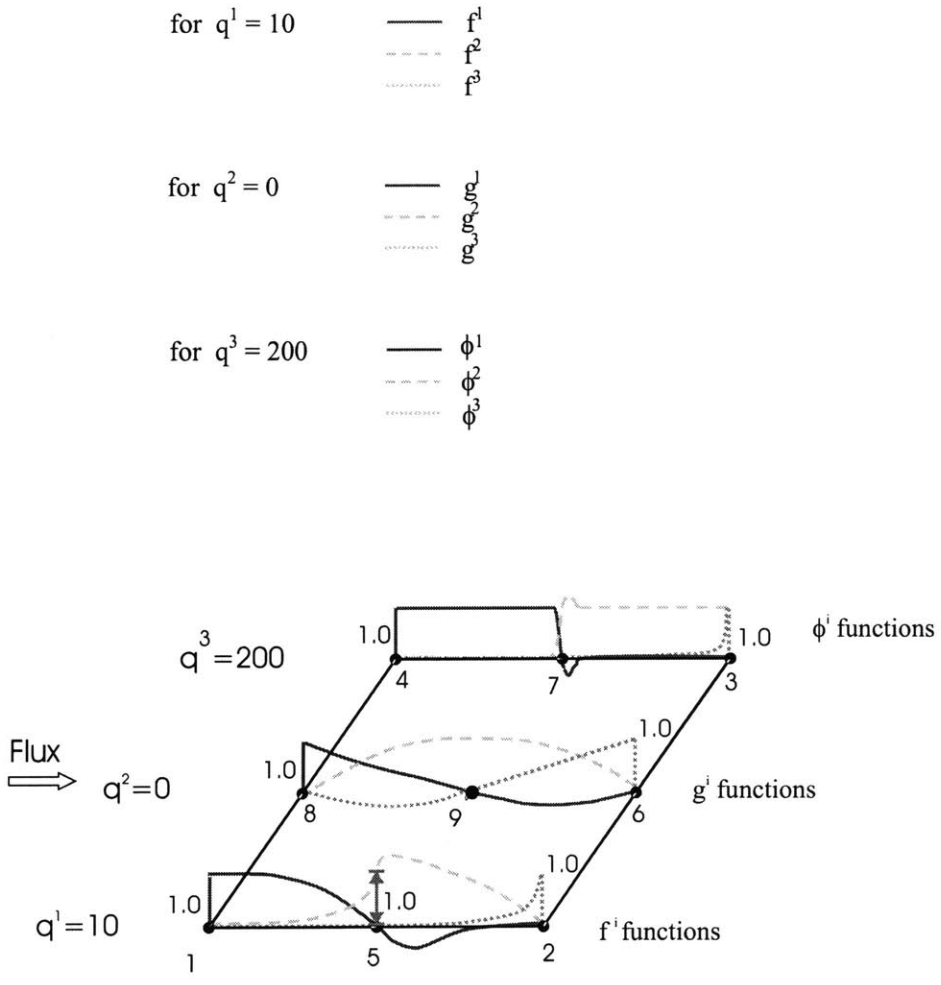

Figure 5-2: The demonstration of f, g and ϕ functions for the flux through 5-7 for the three different values of $q^1 = 10$, $q^2 = 0$ and $q^3 = 200$

To demonstrate the h_j^v functions, once again we consider that the flux is through 5-7 in Fig 5-1 and the h_j^v trial functions are as given in equation (5.5): h_1^v is, for

example,

$$h_1^v = \begin{cases} f^1 \quad \text{for} \quad 0 \leq r \leq 1.0, s = 0 \\ (1-2s)(1-s) \quad \text{for} \quad 0 \leq s \leq 1.0, r = 0 \end{cases} \tag{5.9}$$

This function is shown in Fig 5-3. Trial functions h_5^v and h_8^v are also given in this figure and are as follows,

$$h_5^v = \begin{cases} f^2 \quad \text{for} \quad 0 \leq r \leq 1.0, s = 0 \\ (1-2s)(1-s) \quad \text{for} \quad 0 \leq s \leq 1.0, r = 0.5 \end{cases} \tag{5.10}$$

$$h_8^v = \begin{cases} g^1 \quad \text{for} \quad 0 \leq r \leq 1.0, s = 0.5 \\ 4s(1-s) \quad \text{for} \quad 0 \leq s \leq 1.0, r = 0 \end{cases} \tag{5.11}$$

It is good to mention here the reason why the f, g and ϕ functions are defined as in equations (5.6)-(5.7); while defining new trial functions in V_h for the new 9-node element, it was realized that most of the proposed functions were unable to yield stable solutions. Since, the earlier proposed 9-node element (each element consists of four 4-node sub-elements) is quite stable, as it was shown in chapter 4, it was a good assumption to propose the f, g and ϕ functions such that for high Reynolds numbers, these functions approach the x^k functions of the former 9-node element. This is illustrated in Fig 5-4. For the new 9-node element, f^1, f^2 and f^3 functions for high Reynolds numbers, should almost approach the functions shown in figure (c).

In order to construct the f^1, f^2 and f^3 functions, it was assumed that for $0 \leq r \leq 0.5$, f^1 varies the same as x^1 and for $0.5 \leq r \leq 1.0$, f^3 varies the same as $(1-x^1)$. f^1 function for $0.5 \leq r \leq 1.0$ and f^3 function for $0 \leq r \leq 0.5$, are obtained by the continuity of these functions and their derivatives at $r = 0.5$. Then the f^2 function

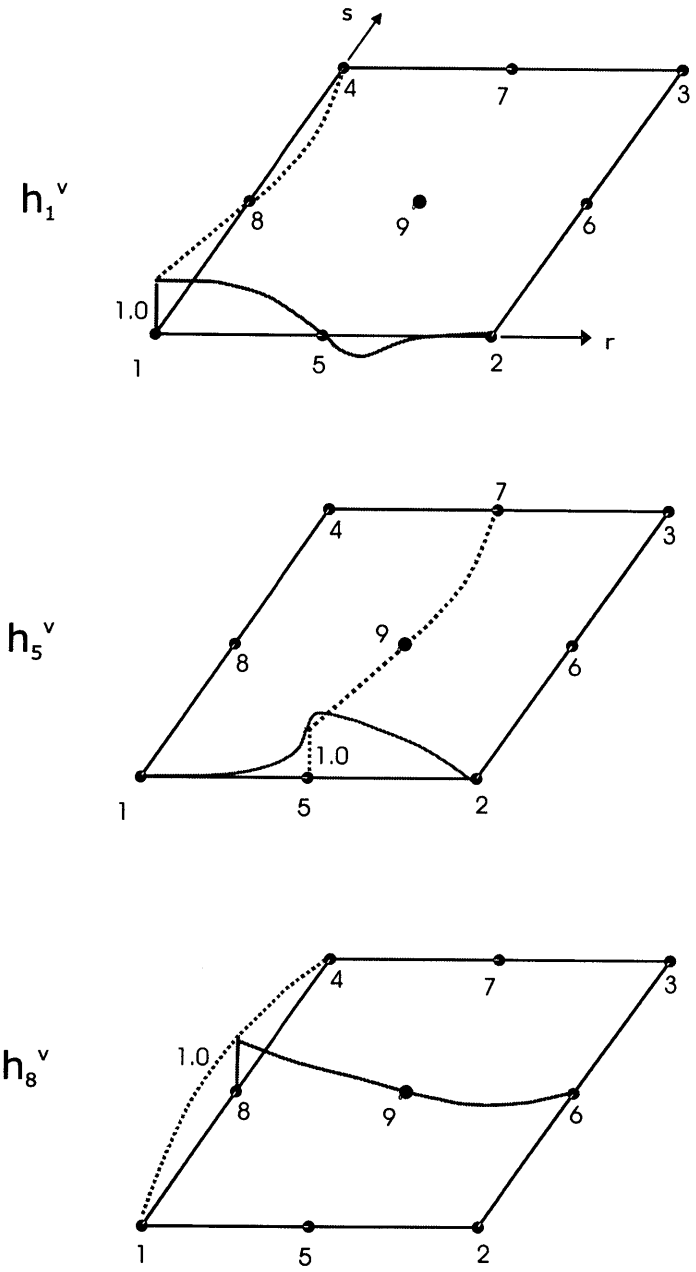

Figure 5-3: The trial functions h_1^v, h_5^v and h_8^v for the flux through 5-7

is defined as $f^2 = 1 - f^1 - f^3$.

The trial functions used here satisfy the requirement $\sum h_i^v = 1$. Note that f^k, g^k and ϕ^k functions and their derivatives in respect to q^k are continuous within the element. When Reynolds number is large enough; q^k is large, these functions approach (almost) the x^k variable used to define the traditional 9-node element (chapter 4). Therefore, the new 9-node element is expected to have comparable stability as the old element. Of course, using the new U_h space will also affect the stability.

The elements in the space Q_h are step functions. Referring to Fig. 5-1, we have, at node 2, for example,

$$h_2^q = \begin{cases} 1 & \text{for } (r,s) \in [\frac{1}{2}\ ,1] \times [0, \frac{1}{2}\ ] \\ 0 & \text{elsewhere} \end{cases} \tag{5.12}$$

Similarly, the weight functions in the space W_h are also step functions and at node 2, for example,

$$h_2^w = \begin{cases} 1 & \text{for } (r,s) \in [\frac{3}{4}\ ,1] \times [0, \frac{1}{4}\ ] \\ 0 & \text{elsewhere} \end{cases} \tag{5.13}$$

Then, the velocities $\mathbf{u}_h$, $\mathbf{v}_h$ and the pressure p_h are, respectively, calculated with the trial functions in U_h, V_h and P_h as follows:

$$\begin{aligned} \mathbf{u}_h &= \sum_{i=1}^{9} h_i^u v_i \\ \mathbf{v}_h &= \sum_{i=1}^{9} h_i^v v_i \\ p_h &= \sum_{i=1}^{4} h_i^p p_i \end{aligned} \tag{5.14}$$

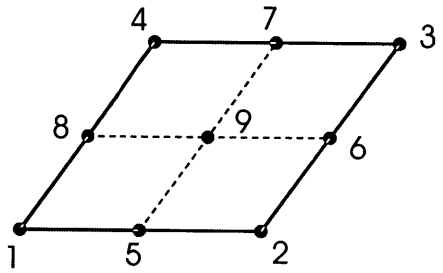

(a) The earlier proposed 9-node element

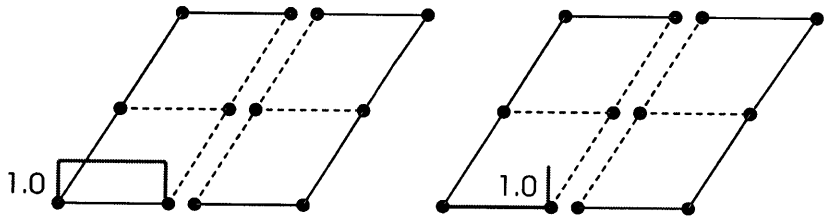

(b) x^1 and $(1-x^1)$ functions for the shown sub-element

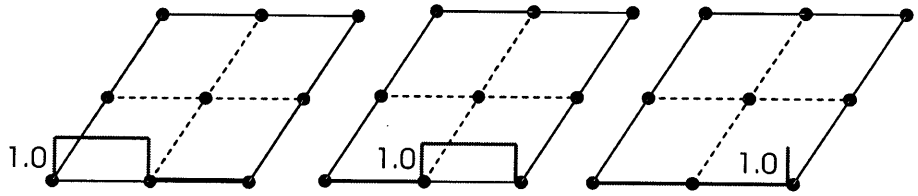

(c) x^1 and $(1-x^1)$ functions for the assemblage of two adjacent sub-elements

Figure 5-4: The earlier proposed 9-node element (consists of four 4-node sub-elements); x^1 and $(1-x^1)$ functions are shown for one sub-element and the assemblage of two adjacent sub-elements for high Reynolds number flow when the flux is through 5-7

where v_i and p_i are the nodal velocity and pressure variables. As in chapter 4, the flux is calculated with the interpolated values at the center of the sides of the control volumes. Analogously, the corresponding *linearized* finite element matrix equations are,

$$\begin{pmatrix} \mathbf{K}_{\mathbf{v}_x\mathbf{v}_x} & \mathbf{K}_{\mathbf{v}_x\mathbf{v}_y} & \mathbf{K}_{\mathbf{v}_x\mathbf{p}} \\ \mathbf{K}_{\mathbf{v}_y\mathbf{v}_x} & \mathbf{K}_{\mathbf{v}_y\mathbf{v}_y} & \mathbf{K}_{\mathbf{v}_y\mathbf{p}} \\ \mathbf{K}_{\mathbf{p}\mathbf{v}_x} & \mathbf{K}_{\mathbf{p}\mathbf{v}_y} & \mathbf{0} \end{pmatrix} \begin{pmatrix} \Delta\mathbf{v}_x \\ \Delta\mathbf{v}_y \\ \Delta\mathbf{p} \end{pmatrix} = \begin{pmatrix} \mathbf{R}_{\mathbf{v}_x} \\ \mathbf{R}_{\mathbf{v}_y} \\ \mathbf{0} \end{pmatrix} - \begin{pmatrix} \mathbf{F}_{\mathbf{v}_x} \\ \mathbf{F}_{\mathbf{v}_y} \\ \mathbf{F}_{\mathbf{p}} \end{pmatrix} \tag{5.15}$$

Similar to (4.24), $\Delta\mathbf{v}_x$, $\Delta\mathbf{v}_y$, $\Delta\mathbf{p}$, are the *increments* of velocity in x direction, velocity in y direction and pressure with respect to the last iteration; $\mathbf{R}_{\mathbf{v}_x}$ and $\mathbf{R}_{\mathbf{v}_y}$ are the discretized load vectors and $\mathbf{F}_{\mathbf{v}_x}$, $\mathbf{F}_{\mathbf{v}_y}$, $\mathbf{F}_{\mathbf{p}}$ contain terms from the linearization process. Elements of the stiffness matrix are defined for the new 9-node element. Using the back-substitution iteration method (in chapter 4, the full Newton-Raphson iteration method was used) for a mesh of non-distorted elements, we get,

$$\mathbf{K}_{\mathbf{v}_x\mathbf{v}_x} = \sum_{\Omega_w} (\rho n_x \frac{\partial y}{\partial s} \int_{\partial\Omega_{wy}} \mathbf{H}^u|_{r^*}\ \mathbf{v}_x\ \mathbf{H}^v|_{r^*}\ ds + \rho n_y \frac{\partial x}{\partial r} \int_{\partial\Omega_{wx}} \mathbf{H}^u|_{s^*}\ \mathbf{v}_y\ \mathbf{H}^v|_{s^*}\ dr$$
$$- \mu n_x \frac{\partial y}{\partial s} \int_{\partial\Omega_{wy}} 2\frac{\partial r}{\partial x}\ \mathbf{H}^u_{,\,r}|_{r^*}\ ds - \mu n_y \frac{\partial x}{\partial r} \int_{\partial\Omega_{wx}} \frac{\partial s}{\partial y}\ \mathbf{H}^u_{,\,s}|_{s^*}\ dr)$$

$$\mathbf{K}_{\mathbf{v}_x\mathbf{v}_y} = -\sum_{\Omega_w} \mu n_y \frac{\partial x}{\partial r} \int_{\partial\Omega_{wx}} \frac{\partial r}{\partial x}\ \mathbf{H}^u_{,\,r}|_{s^*}\ dr$$

$$\mathbf{K}_{\mathbf{v}_y\mathbf{v}_x} = -\sum_{\Omega_w} \mu n_x \frac{\partial y}{\partial s} \int_{\partial\Omega_{wy}} \frac{\partial s}{\partial y}\ \mathbf{H}^u_{,\,s}|_{r^*}\ ds$$

$$\mathbf{K}_{\mathbf{v}_y\mathbf{v}_y} = \sum_{\Omega_w} (\rho n_x \frac{\partial y}{\partial s} \int_{\partial\Omega_{wy}} \mathbf{H}^u|_{r^*}\ \mathbf{v}_x\ \mathbf{H}^v|_{r^*}\ ds + \rho n_y \frac{\partial x}{\partial r} \int_{\partial\Omega_{wx}} \mathbf{H}^u|_{s^*}\ \mathbf{v}_y\ \mathbf{H}^v|_{s^*}\ dr$$
$$- \mu n_x \frac{\partial y}{\partial s} \int_{\partial\Omega_{wy}} \frac{\partial r}{\partial x}\ \mathbf{H}^u_{,\,r}|_{r^*}\ ds - \mu n_y \frac{\partial x}{\partial r} \int_{\partial\Omega_{wx}} 2\frac{\partial s}{\partial y}\ \mathbf{H}^u_{,\,s}|_{s^*}\ dr)$$

$$\mathbf{K}_{\mathbf{v}_x\mathbf{p}} = \sum_{\Omega_w} n_x \frac{\partial y}{\partial s} \int_{\partial\Omega_{wy}} \mathbf{H}^p|_{r^*}\ ds$$

$$\mathbf{K}_{\mathbf{v}_y\mathbf{p}} = \sum_{\Omega_w} n_y \frac{\partial x}{\partial r} \int_{\partial\Omega_{wx}} \mathbf{H}^p|_{s^*}\ dr$$

$$\mathbf{K}_{\mathbf{p}\mathbf{v}_x} = \sum_{\Omega_q} \rho n_x \frac{\partial y}{\partial s} \int_{\partial\Omega_{qy}} \mathbf{H}^u|_{r^*}\ ds$$

$$\mathbf{K}_{\mathbf{p}\mathbf{v}_y} = \sum_{\Omega_q} \rho n_y \frac{\partial x}{\partial r} \int_{\partial\Omega_{qx}} \mathbf{H}^u|_{s^*}\ dr$$

(5.16)

where Ω_w and Ω_q are the control volumes for the velocity and pressure points respectively (Fig. 5-5); all the integrals are calculated over the sides of the control volumes

and subscripts x and y in $\partial\Omega$ refer to the control volume sides in x and y directions; n_x and n_y are the elements of the normal vector $\mathbf{n}$ and are either 1 or -1; the superscript * indicates the flux is calculated with the interpolated values at the center of the sides of the control volumes and $\mathbf{H}^u$, $\mathbf{H}^v$ and $\mathbf{H}^p$ contain the trial functions corresponding to U_h, V_h and P_h spaces.

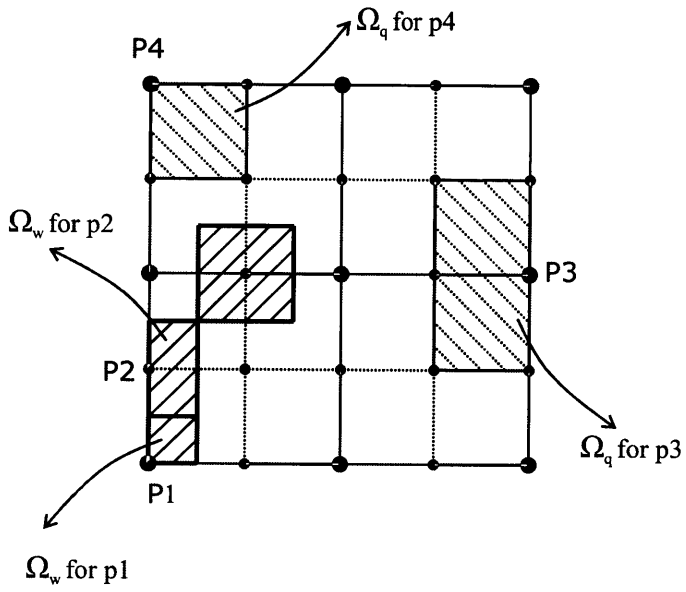

Figure 5-5: Illustration of Ω_w and Ω_q; the control volumes of the velocity and pressure points respectively

5.2 Comparison of the new 9-node element with the earlier published 9-node element

In this section the new proposed FCBI 9-node element, is numerically investigated and compared to the former FCBI 9-node element which consists of four 4-node sub-elements. The element is first tested for the driven cavity flow problem and then for the S-channel flow problem.

In both problems, when the Reynolds number is increased, the new FCBI 9-node element has comparable stability as the former FCBI 9-node element. The reason is that when the Reynolds number is large enough; q^k is large and the f^k, g^k and ϕ^k functions (5.6-5.8) (almost) approach the x^k variable used to define the earlier published 9-node element (chapter 4). However, using the parabolic trial functions in the U_h space for the new FCBI 9-node element slightly decreases the stability since these functions have negative values as well within each element.

To study the accuracy and convergence of the new element, the same error norms as section (4.5.2) are used; the L^2 and H^1 norms of the velocities and L^2 norm of the pressures.

$$\| \mathbf{u} - \mathbf{u}_h \|^2_{L^2} = \sum_{over\ elements} \int (u - u_h)^2_x \, dxdy + \sum_{over\ elements} \int (u - u_h)^2_y \, dxdy \quad (5.17)$$

$$\begin{aligned} \| \mathbf{u} - \mathbf{u}_h \|^2_{H^1} = & \sum_{over\ elements} \int (u - u_h)^2_x \, dxdy + \sum_{over\ elements} \int (u - u_h)^2_y \, dxdy \\ & + \sum_{over\ elements} \int (u - u_h)^2_{x,\,x} \, dxdy + \sum_{over\ elements} \int (u - u_h)^2_{x,\,y} \, dxdy \\ & + \sum_{over\ elements} \int (u - u_h)^2_{y,\,x} \, dxdy + \sum_{over\ elements} \int (u - u_h)^2_{y,\,y} \, dxdy \end{aligned} \quad (5.18)$$

$$\| p - p_h \|^2_{L^2} = \sum_{over\ elements} \int (p - p_h)^2 \, dxdy \quad (5.19)$$

where $\mathbf{u}_h \in U_h$ and $p_h \in P_h$. Since the focus of this thesis is on the non-distorted elements, all the integrals are simply obtained using the Maple program (no numerical integration).

In these equations, $(\ \cdot\ )_{,\,x}$ and $(\ \cdot\ )_{,\,y}$ are the x and y derivatives, $(u - u_h)_x$

and $(u - u_h)_y$ are the x and y components of $(\mathbf{u} - \mathbf{u}_h)$ respectively where $\mathbf{u}$ is the exact velocity and $\mathbf{u}_h$ is the velocity obtained by the finite element solution. The exact solution is the analytical solution and it is unknown for most of the fluid flow problems. In these problems, the finite element solution obtained using the Galerkin 9-node element (with no upwinding) for a very fine mesh is assumed to be the exact solution.

Note that for the earlier published FCBI 9-node elements in (4.5.2), U_h was the space of bilinear functions within each sub-element and $\| \mathbf{u} - \mathbf{u}_h \|_{L^2}$ and $\| \mathbf{u} - \mathbf{u}_h \|_{H^1}$ norms were calculated over the sub-elements. Here, parabolic trial functions in U_h space are defined within each 9-node element.

- The driven cavity flow problem ($Re = 1000$)

To demonstrate the solution errors in detail, the non-uniform mesh of 4×4 elements (Fig.4.?), 8×8 and 16×16 elements are considered. The exact solution is assumed to be the finite element solution obtained using the Galerkin 9-node element (with no upwinding) for a uniform mesh of 64×64 elements. Figure 5-6 illustrates that the $\| \mathbf{u} - \mathbf{u}_h \|_{L^2}$, $\| \mathbf{u} - \mathbf{u}_h \|_{H^1}$ and $\| p - p_h \|_{L^2}$ norms converge when the mesh is refined. In this figure, the solid and the dashed lines represent the solutions for the new FCBI 9-node elements and the earlier published 9-node elements, respectively. It is clear that the solution errors are smaller using the new FCBI 9-node element but the rate of convergence is almost the same.

- The S-channel flow problem ($Re = 100$)

For the S-channel flow problem, consider the same mesh shown in Fig.4.? and 2 times finer and coarser meshes. Convergence curves for the velocity are given in figures (5-7a) and (5-7b) for the L^2 and H^1 norms respectively. In figures (5-7c) and (5-7d), we show the convergence curves for $\| p - p_h \|_{L^2}$ and for $\| \mathbf{u} - \mathbf{u}_h \|_{H^1} + \| p - p_h \|_{L^2}$. In this figure, the solid and the dashed lines represent the solutions for the new FCBI 9-node elements and the former 9-node elements, respectively. When the mesh is refined, velocity and pressure errors are smaller in the L^2 norm for the new proposed

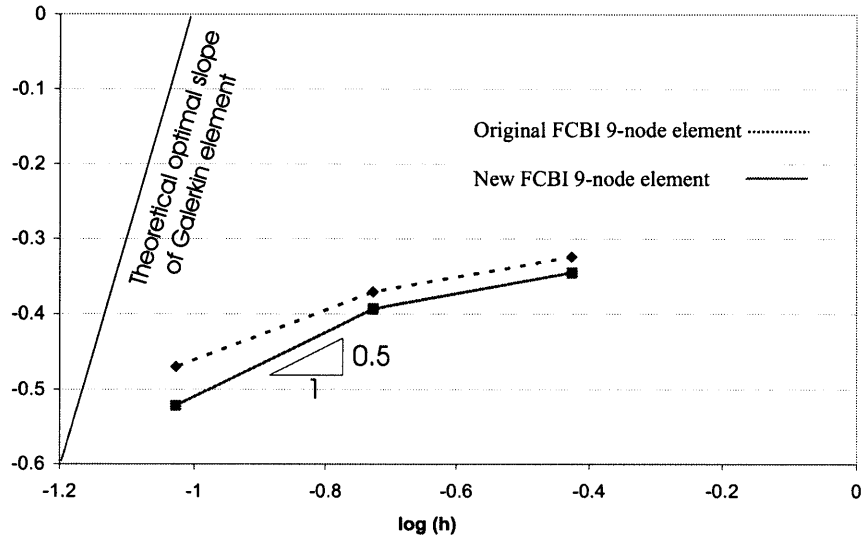

Fig 5.6 (a)

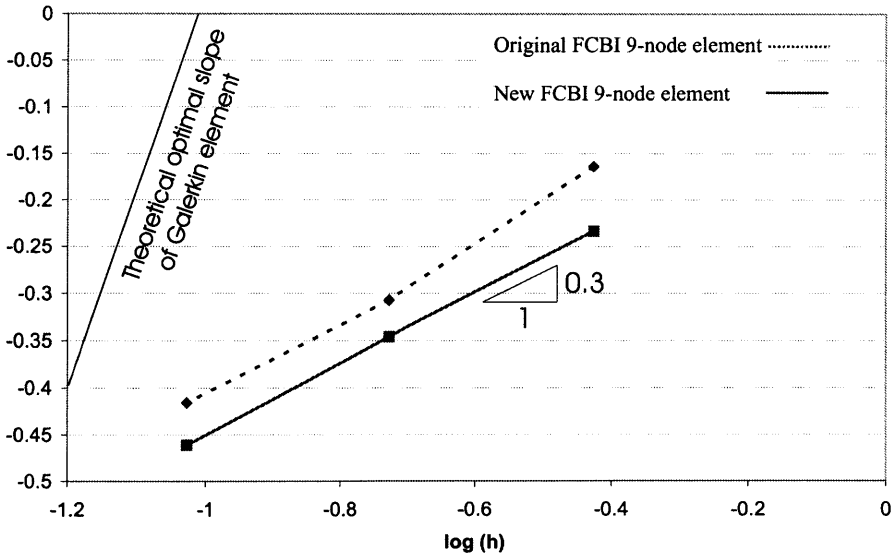

Fig 5.6 (b)

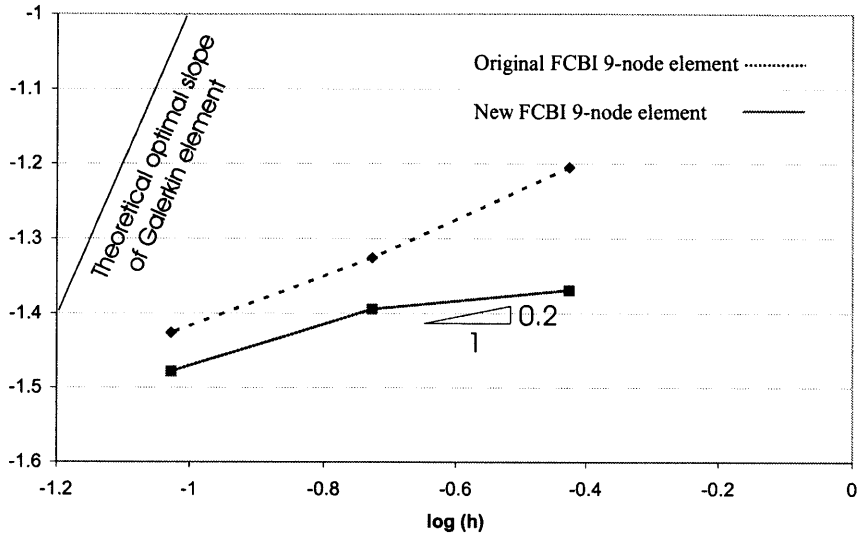

Fig 5.6 (c)

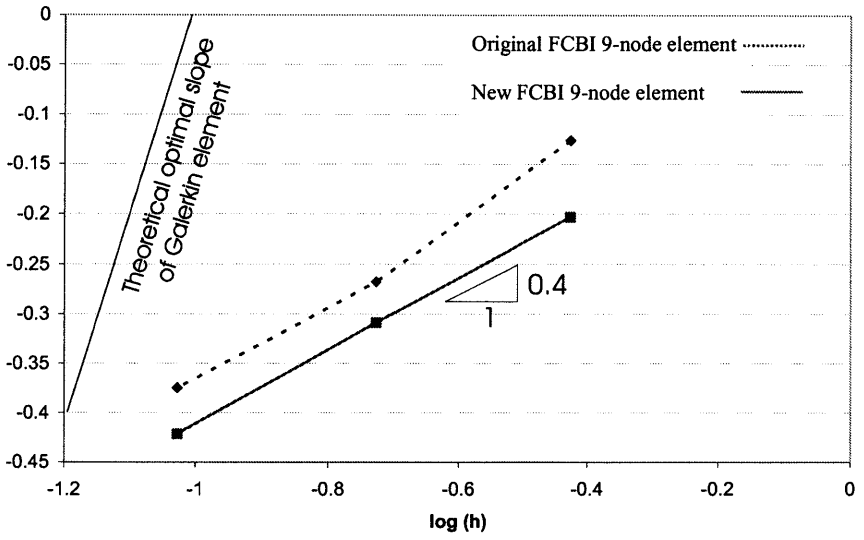

Fig 5.6 (d)

Figure 5-6: Comparison of the new FCBI 9-node elements and the original FCBI 9-node elements for the driven cavity flow problem (Re=1000). In this figure, the x coordinate represents log h when h is the mesh size and the y coordinate for each case is a) $log\ \frac{\|\mathbf{u}-\mathbf{u}_h\|_{L^2}}{\|\mathbf{u}\|_{L^2}}$, b) $log\ \frac{\|\mathbf{u}-\mathbf{u}_h\|_{H^1}}{\|\mathbf{u}\|_{H^1}}$, c) $log\ \frac{\|p-p_h\|_{L^2}}{\|p\|_{L^2}}$, d) $log\ (\frac{\|\mathbf{u}-\mathbf{u}_h\|_{H^1}}{\|\mathbf{u}\|_{H^1}} + \frac{\|p-p_h\|_{L^2}}{\|p\|_{L^2}})$.

9-node element, and the velocity errors are the same for the H^1 norm. In addition, the convergence curves for the L^2 norm (for the velocity and the pressure both) display a larger rate of convergence for the new 9-node element.

5.3 Comparison of the new 9-node element with the Galerkin 9-node element

In this section the newly proposed FCBI 9-node element , is compared to the Galerkin 9-node finite element. The Galerkin 9-node finite element uses the 9 nodes for the velocities and the 4 corner nodes for the pressure interpolations[2]. To compare the accuracy and convergence of the new element and the Galerkin 9-node element, the same error norms as in section (4.5.2) are used; the L^2 and H^1 norms of the velocities and L^2 norm of the pressures, and the same driven cavity flow and the S-channel flow problems are considered.

In both problems, when the Reynolds number is increased, the new FCBI 9-node element is more stable than the Galerkin 9-node element. However, in the cavity flow problem, using the Galerkin 9-node element yields more accurate solutions with a higher rate of convergence. Since our goal is to use a new 9-node FCBI element together with the "goal-oriented error estimation" to control the error of the solution in the structural response in the FSI problems, we want a 9-node element with much better stability and comparable accuracy as Galerkin 9-node element. From the numerical results presented in this section, it becomes clear that the new 9-node elements do not obtain the solution as accurate as the Galerkin 9-node elements but the solution is stable for much higher Reynolds numbers (than the Galerkin 9-node elements), and accurate enough to be used to find the structural responses.

- The driven cavity flow problem

The same non-uniform meshes 4×4, 8×8, 16×16 and 32×32 elements used in (5.2) are considered. Figure 5-8 shows the convergence of the $\| \mathbf{u} - \mathbf{u}_h \|_{L^2}$, $\| \mathbf{u} - \mathbf{u}_h \|_{H^1}$

[2]Also referred to as the Taylor-Hood, Q9/Q4, or 9/4-c element [1]

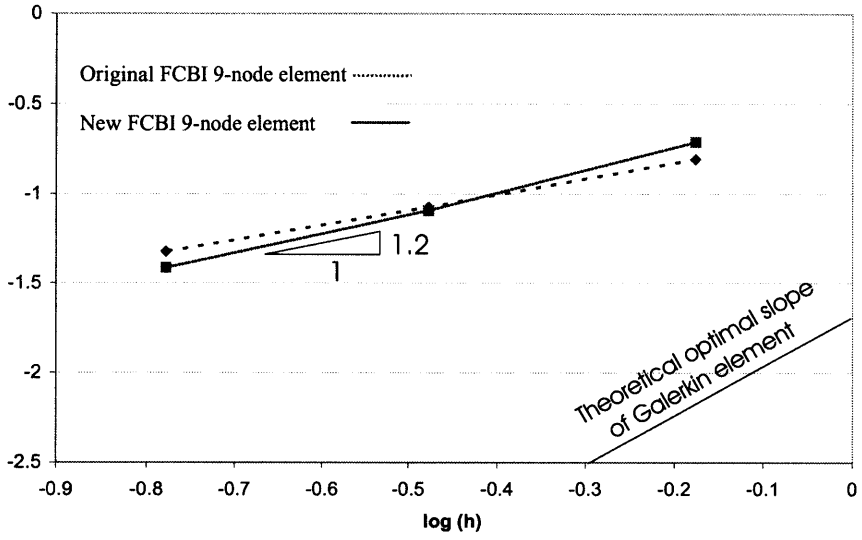

Fig 5.7 (a)

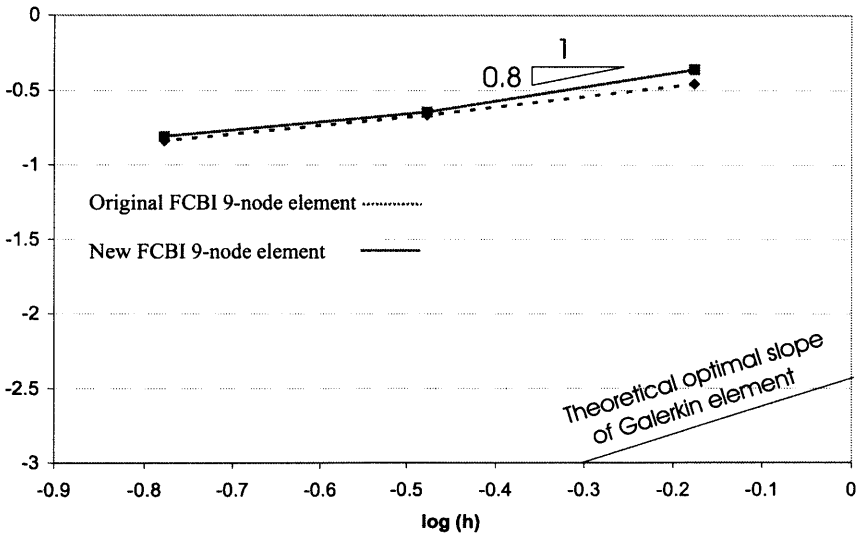

Fig 5.7 (b)

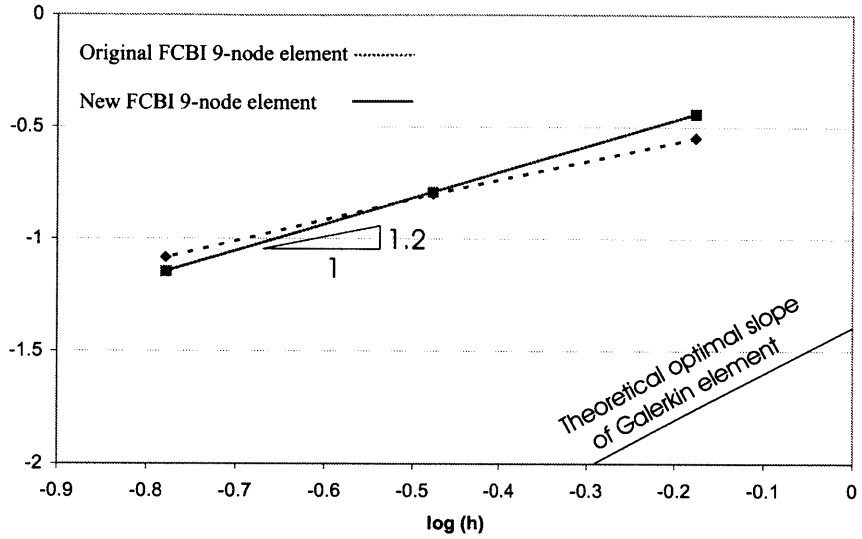

Fig 5.7 (c)

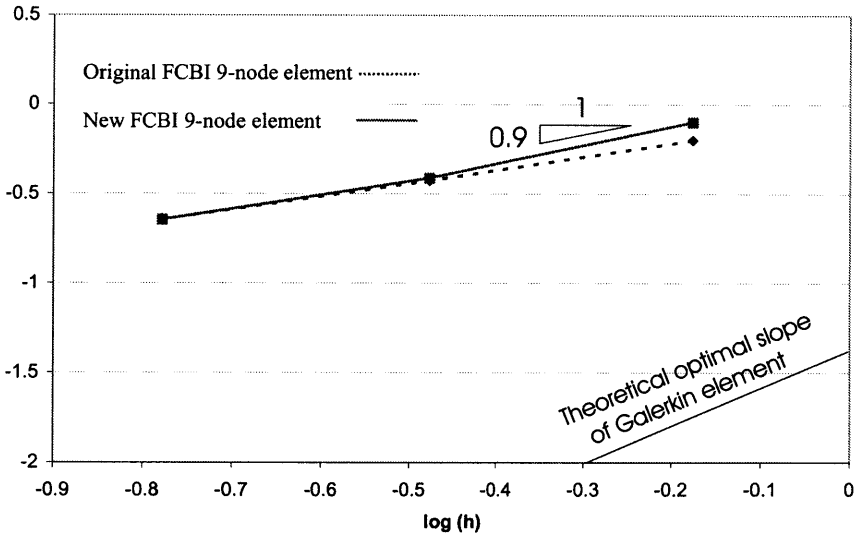

Fig 5.7 (d)

Figure 5-7: Comparison of the new FCBI 9-node elements and the original FCBI 9-node elements for the S-channel flow problem (Re=100). In this figure, the x coordinate represents log h when h is the mesh size and the y coordinate for each case is a) $log\ \frac{\|\mathbf{u}-\mathbf{u}_h\|_{L^2}}{\|\mathbf{u}\|_{L^2}}$, b) $log\ \frac{\|\mathbf{u}-\mathbf{u}_h\|_{H^1}}{\|\mathbf{u}\|_{H^1}}$, c) $log\ \frac{\|p-p_h\|_{L^2}}{\|p\|_{L^2}}$, d) $log\ (\frac{\|\mathbf{u}-\mathbf{u}_h\|_{H^1}}{\|\mathbf{u}\|_{H^1}} + \frac{\|p-p_h\|_{L^2}}{\|p\|_{L^2}})$.

and $\| p - p_h \|_{L^2}$ norms when the mesh is refined. In this figure, the solid and the dashed lines represent the solutions using the new FCBI 9-node elements and the Galerkin 9-node finite elements, respectively. From the convergence curves shown in this figure we observe that the errors are larger using the new proposed 9-node element. In addition when the mesh is refined, the Galerkin 9-node element has higher rate of convergence. However, the Galerkin 9-node element only yields stable solutions for low Reynolds numbers.

Table 5.1 compares the stability of the new proposed 9-node element with the Galerkin 9-node element. In this table, a non-uniform mesh 16×16 elements is used, and the number of iterations required to solve the problem, is also shown for the earlier proposed FCBI 9-node element.

To obtain the results given in this table, the Newton-Raphson iteration method is used for the Galerkin 9-node element and the former FCBI 9-node element when the back-substitution method is used for the new FCBI 9-node element. In this table, (*) denotes that the iteration did not converge within the allowable 50 number of iterations. This table is given for the convergence tolerance 10^{-3}. As it is clear, both FCBI 9-node elements give more stable solutions than the Galerkin 9-node element.

Since our goal is to use a 9-node element together with the "goal-oriented error estimation" to control the error of the solution in the structural response in the fluid-structure interaction problems, we want an element that gives stable solutions for high Reynolds numbers (more stable than the Galerkin 9-node element) with reasonable accuracy (in a coarse mesh). The new proposed 9-node element is such an element which yields stable solutions for higher Reynolds numbers. Although the errors are larger for the new 9-node element, the accuracy of the solution is still reasonable to obtain the structural response in the FSI problems.

In the case of using the Galerkin 9-node finite elements, the solution for the mesh of 4×4 elements is not stable and therefore not given in the figure.

- The S-channel flow problem

For the S-channel flow problem, consider the same meshes as used in section (5.2).

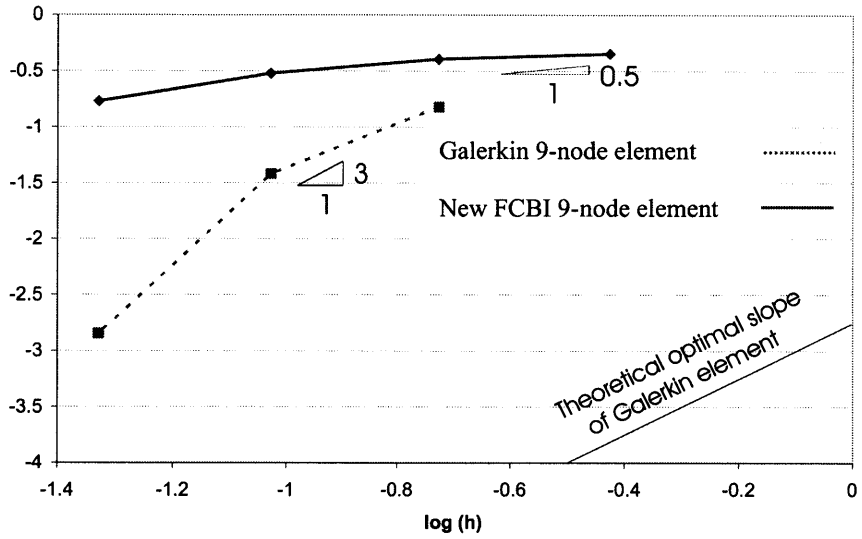

Fig 5.8 (a)

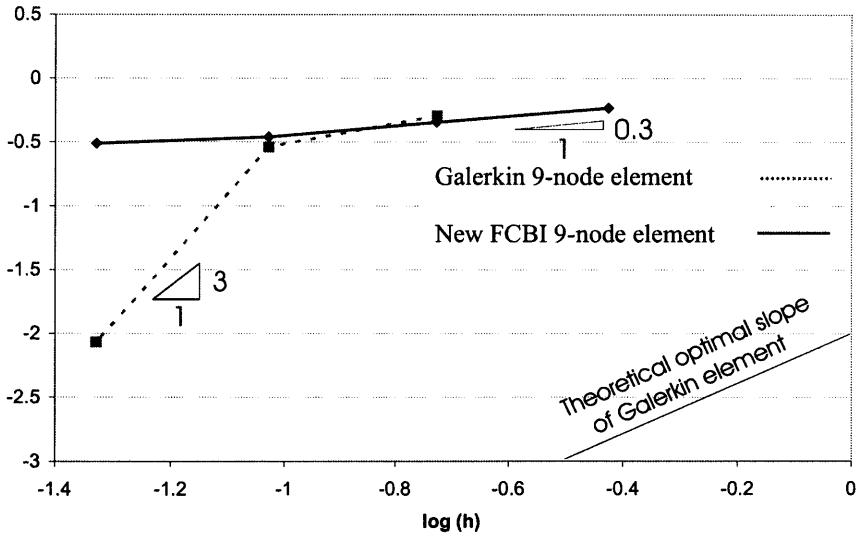

Fig 5.8 (b)

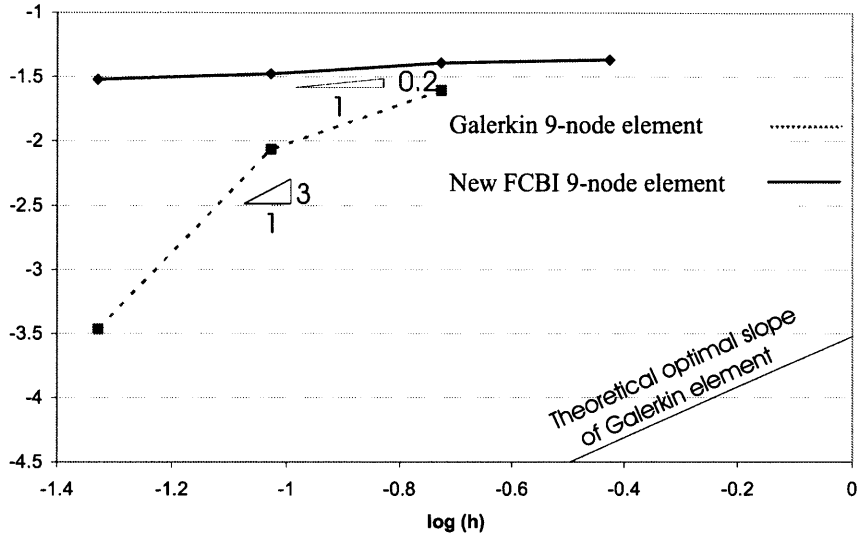

Fig 5.8 (c)

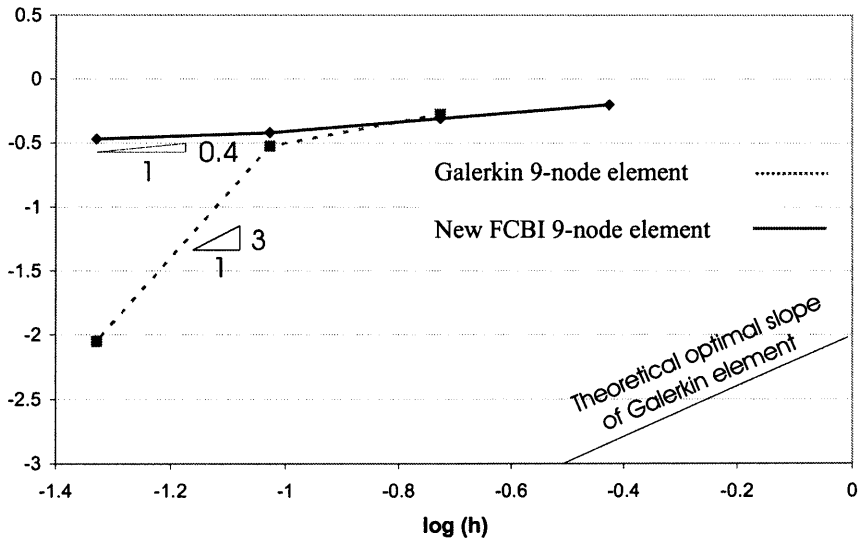

Fig 5.8 (d)

Figure 5-8: Comparison of the new FCBI 9-node elements and the Galerkin 9-node elements for the driven cavity flow problem (Re=1000). In this figure, the x coordinate represents log h when h is the mesh size and the y coordinate for each case is a) $log\ \frac{\|\mathbf{u}-\mathbf{u}_h\|_{L^2}}{\|\mathbf{u}\|_{L^2}}$, b) $log\ \frac{\|\mathbf{u}-\mathbf{u}_h\|_{H^1}}{\|\mathbf{u}\|_{H^1}}$, c) $log\ \frac{\|p-p_h\|_{L^2}}{\|p\|_{L^2}}$, d) $log\ (\frac{\|\mathbf{u}-\mathbf{u}_h\|_{H^1}}{\|\mathbf{u}\|_{H^1}} + \frac{\|p-p_h\|_{L^2}}{\|p\|_{L^2}})$.

Re	The Galerkin 9-node element	The new proposed 9-node element	The earlier published 9-node element
50	4	4	4
100	6	4	4
150	8	5	5
200	*	6	6
1000		9	8
5000		9	9
10,000		11	10
30,000		40	12
45,000		*	16
50,000			*

Table 5.1: Number of iterations required to solve the driven cavity flow problem with different Re numbers. In this table, a non-uniform mesh of 16×16 elements is used, and the convergence tolerance is 10^{-3} for the normalized norms $R_{\mathbf{v}} = \frac{||\Delta \mathbf{v}_h||}{||\mathbf{v}_h||}$ and $R_p = \frac{||\Delta p_h||}{||p_h||}$.

Convergence curves for the velocity are given in figures (5-9a) and (5-9b) for the L^2 and H^1 norms respectively. In figures (5-9c) and (5-9d), we show the convergence curves for $|| p - p_h ||_{L^2}$ and for $|| \mathbf{u} - \mathbf{u}_h ||_{H^1} + || p - p_h ||_{L^2}$. In this figure, the solid and the dashed lines represent the solutions using the new FCBI 9-node elements and the Galerkin 9-node elements, respectively.

The velocity errors are approximately the same in the L^2 and H^1 norms, and the pressures are better predicted using the Galerkin 9-node elements. Similar to the driven cavity flow problem, the new FCBI 9-node element gives stable solutions for higher Reynolds numbers than the Galerkin 9-node element, and although the solution is not as accurate as the solution obtained using the Galerkin 9-node element, it is still sufficiently accurate to be used to find the structural response in fluid-structure interaction problems.

- Concluding remarks on the numerical results

Of course we can only draw partial conclusions from these preliminary numerical results since, in particular, other fluid problems need to be considered for compre-

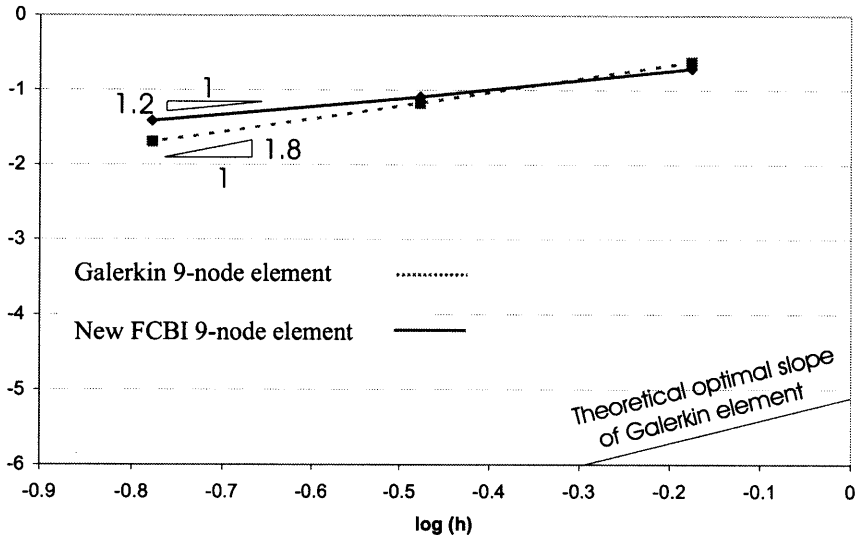

Fig 5.9 (a)

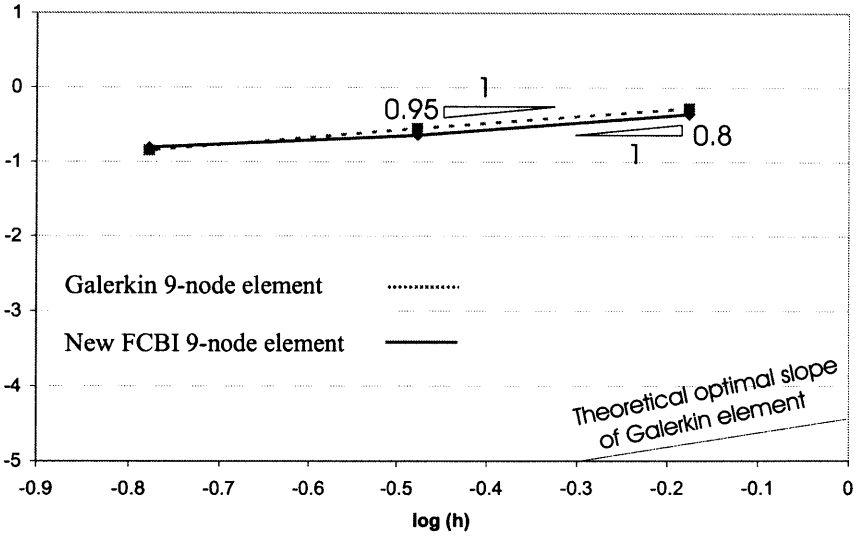

Fig 5.9 (b)

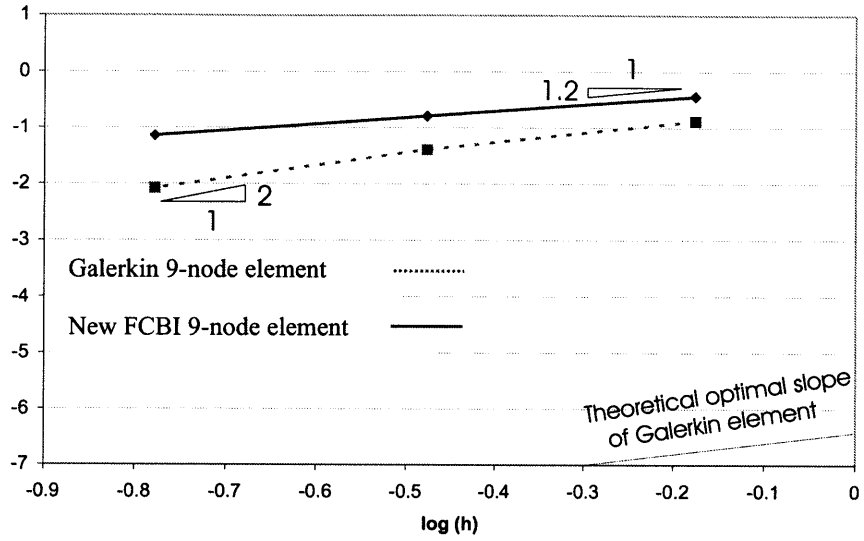

Fig 5.9 (c)

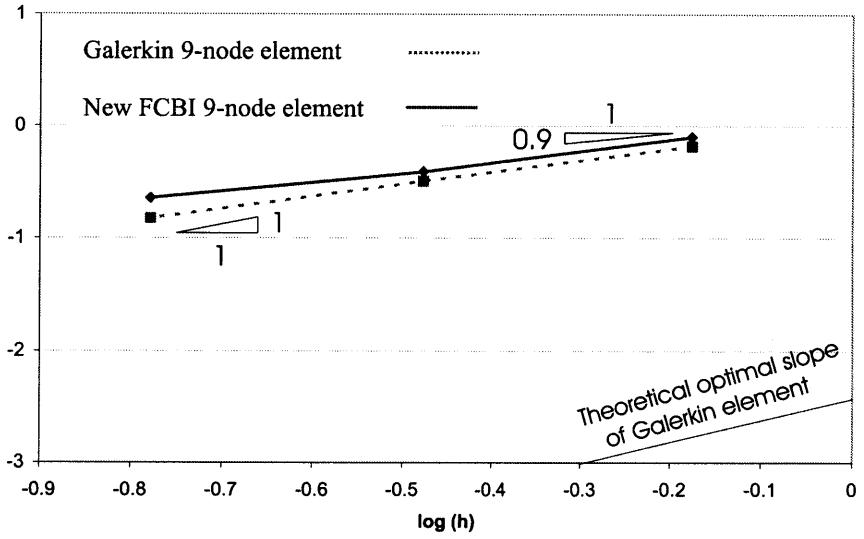

Fig 5.9 (d)

Figure 5-9: Comparison of the new FCBI 9-node elements and the Galerkin 9-node elements for the S-channel flow problem (Re=100). In this figure, the x coordinate represents log h when h is the mesh size and the y coordinate for each case is a) $log\ \frac{\|\mathbf{u}-\mathbf{u}_h\|_{L^2}}{\|\mathbf{u}\|_{L^2}}$, b) $log\ \frac{\|\mathbf{u}-\mathbf{u}_h\|_{H^1}}{\|\mathbf{u}\|_{H^1}}$, c) $log\ \frac{\|p-p_h\|_{L^2}}{\|p\|_{L^2}}$, d) $log\ (\frac{\|\mathbf{u}-\mathbf{u}_h\|_{H^1}}{\|\mathbf{u}\|_{H^1}} + \frac{\|p-p_h\|_{L^2}}{\|p\|_{L^2}})$.

hensiveness.

From these numerical results, the new proposed FCBI 9-node element appears to predict the solution more accurate than the earlier published FCBI 9-node element. For the S-channel flow problem, the convergence curves display a larger rate of convergence using the new 9-node element. In addition, the errors are larger using the new 9-node element than using the Galerkin 9-node element but still accurate enough to be used together with the "goal-oriented error estimation" to control the error of the solution in the structural response in the fluid-structure interaction problems (for "goal-oriented error estimation" we want a 9-node element that with reasonable accuracy gives stable solutions for high Reynolds numbers, however the Galerkin 9-node element is only stable for low Reynolds numbers).

Chapter 6

Linking FCBI to CIP method (CIP-FCBI)

Hydrodynamics equations presented with partial differential equations are usually hard to solve numerically. For example, in problems with discontinuity one must deal with the sudden change of the values or discontinuity in solving these equations. Although there has been progress in numerical analysis and computing technology, various proposed methods are complicated, require much computational effort and are applicable only for specific problems. Therefore, there is still interest in developing more effective methods for solving hydrodynamics equations numerically.

The Cubic-Interpolated Pseudo-particle (CIP) method was introduced by T.Yabe *et al.* in 1991 [26], [17]. In this method, a cubic polynomial is used to interpolate the spatial profile of the value f and its spatial derivative ∇f. The spatial derivative itself is a free parameter and satisfies the master equation for the derivative. After the values f and ∇f are found, the same values for the next time step are simply calculated by shifting the cubic polynomial.

The CIP scheme is a very stable finite difference technique that can solve generalized hyperbolic equations by the 3rd order of accuracy in space. For nonlinear problems, the CIP scheme splits the hyperbolic equation into two phases; the non-advection phase and the advection phase. In each time step, after the non-advection phase is solved by the finite difference method, the CIP method is applied to the ad-

vection phase. This method has been applied to various problems such as solving the Korteweg-de Vries equation and the one-dimensional and two-dimensional shock-tube problems.

The CIP-CUP method (CIP-Combined Unified Procedure) was introduced by T.Yabe *et al.* to solve complex compressible and incompressible fluid flow problems [25], [27]. This method is a pressure-based semi-implicit solver for the Euler equations or the Navier-Stokes equations of fluid flows. The CIP-CUP method solves the non-conservative form of the governing equations in three phases; the convection phase, the remaining phase and the acoustic phase. The acoustic part is solved implicitly by the CUP method while the convection part is solved explicitly by the CIP method. However, at the interface of different fluids in composite flows, or for fluid flow structure interaction problems at the interface of the fluid and structure, there will be oscillation and diffusion in the solution. The reason is that the physical quantities (the material properties) and consequently the sound speeds have large changes at the interfaces which causes problems in the numerical solution.

In section 1, a review of the CIP method is given. Then, in order to solve the Navier-Stokes equations, the CIP scheme is linked to the finite element method (CIP-FEM) and the FCBI scheme (CIP-FCBI), in sections 2 and 3 respectively.

6.1 CIP method

In order to do numerical simulations, the continuous media should be discretized. The goal of the numerical algorithms is not to lose information inside the grid cell between the digitized points. However, most of the proposed numerical schemes fail to take care of the real solution inside the grid cell and in order to have a high resolution, the grid cells should be very small. The CIP method constructs a solution inside the grid cell which is sought close to the real solution of the given equation. We explain the strategy of the CIP method by using the linear advection equation,

$$\frac{\partial f}{\partial t} + u\frac{\partial f}{\partial x} = 0 \tag{6.1}$$

When the velocity is constant, the solution of this equation is a translational wave with the velocity u. If the solution at time $t = 0$ is shown with the solid line in (a) in figure 6-1, at time t, the solution is shown by the dashed line. The solution at grid points is denoted by circles and is the same as the exact solution. However, if we eliminate the lines as in figure (b), the solution profile inside the grid cell has been lost and it is hard to imagine this profile. Of course, one might imagine a linear profile like that shown by the solid line in figure (c). This process is called the first-order upwind scheme and it causes numerical diffusion in the solution. If we use a quadratic polynomial for interpolation, the process is called the Lax-Wendroff scheme or Leith scheme. The problem with this scheme is that it presents a smooth solution with neglecting the real behavior inside the grid cell and there is overshooting at the grid points.

The CIP method approximates the profile close to the real solution within a grid cell. Differentiating (6.1) with spatial variable x we get,

$$\frac{\partial g}{\partial t} + u\frac{\partial g}{\partial x} = -\frac{\partial u}{\partial x} g \tag{6.2}$$

where $g = \frac{\partial f}{\partial x}$.

In the simplest case when the velocity u is constant, (6.2) has exactly the same form as (6.1) and represents the propagation of the spatial derivative with velocity u. If g could be predicted to propagate like that shown in figure (d), the profile after one time step would be limited to a specific profile. This constraint makes the solution become much closer to the initial profile, that is, the real solution.

6.1.1 One-dimensional CIP solver

Linear problem

We consider the one-dimensional hyperbolic equation,

$$L_1 f = \frac{\partial f}{\partial t} + u\frac{\partial f}{\partial x} = 0 \tag{6.3}$$

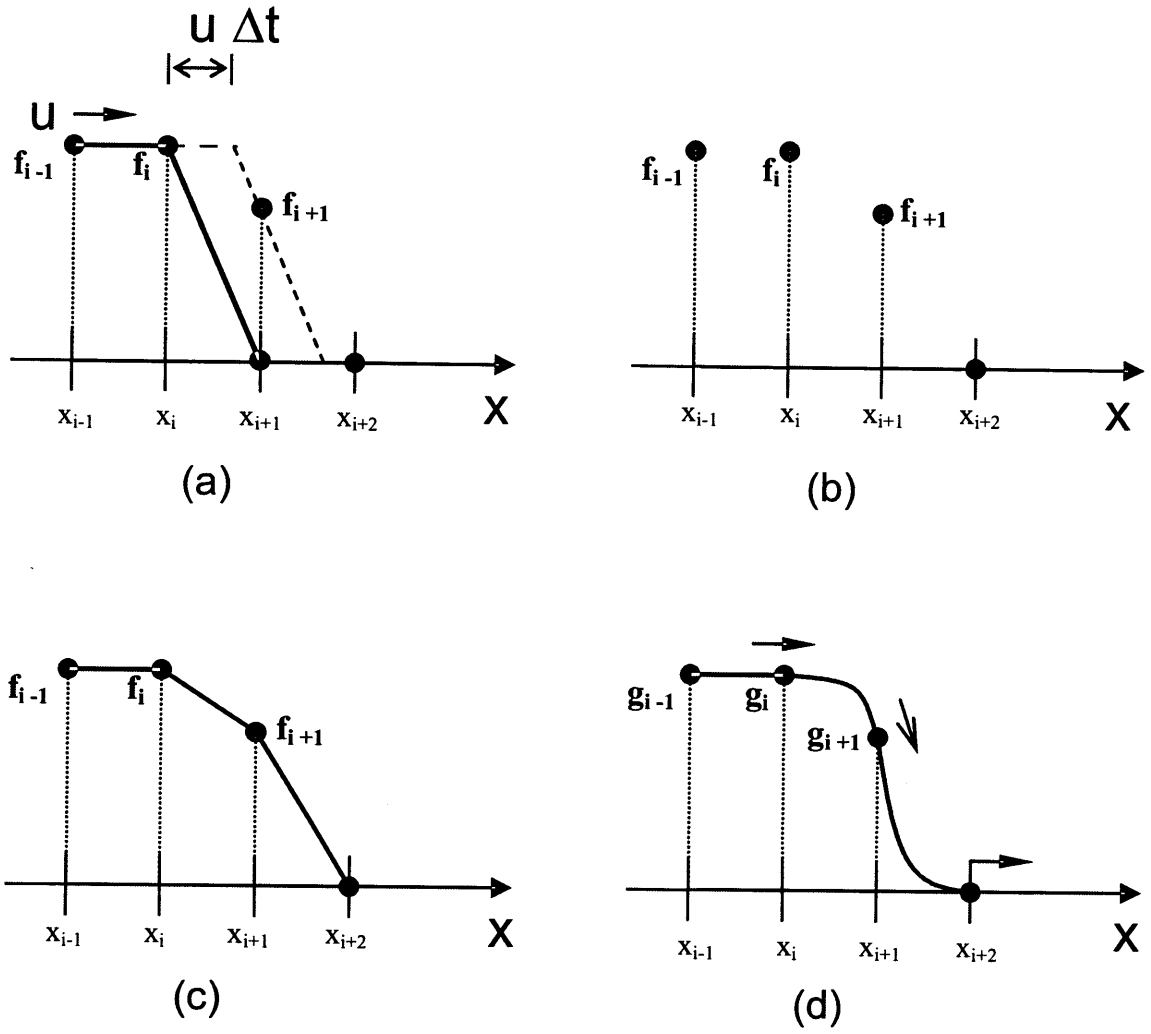

Figure 6-1: The principle of the CIP method. (a) The initial profile and the exact solution (b) The exact solution at the grid points (c) Linear profile between the grid points (d) The spatial derivative in the CIP method

where the value of f is given at grid points $x_1, ..., x_i, ...$ at time $t - \Delta t$. Within each cell (k) bounded by nodes i and $i+1$, f is interpolated using a cubic polynomial such as,

$$F_k(X) = [\ (a_i X + b_i)X + f'_i\ ]X + f_i \tag{6.4}$$

where $X = x - x_i$ and f'_i denotes the spatial derivative of f at point i.

In the CIP method the spatial derivative of f is itself a variable and should satisfy the spatial derivative of the master equation (6.3).

$$L_1(\partial_x f) = \frac{\partial f'}{\partial t} + u\frac{\partial f'}{\partial x} = -\frac{\partial u}{\partial x}\ \frac{\partial f}{\partial x} \tag{6.5}$$

The values of f and f' are known at all the grid points and in order to find f within each cell, the coefficients a_i and b_i should be determined. For the grid cell (k) located between grid points x_i and x_{i+1}, these coefficients are found by the continuity of f and f' at point $i+1$.

$$\begin{aligned} f_{i+1} &= F_k(X = \Delta x) = [\ (a_i \Delta x + b_i)\Delta x + f'_i\ ]\Delta x + f_i \\ f'_{i+1} &= \frac{\partial F_k(X = \Delta x)}{\partial x} = 3a_i \Delta x^2 + 2b_i \Delta x + f'_i \end{aligned} \tag{6.6}$$

where $\Delta x = x_{i+1} - x_i$.

Then these coefficients are as follows,

$$\begin{aligned} a_i &= \frac{(f'_i + f'_{i+1})}{\Delta x^2} + \frac{2(f_i - f_{i+1})}{\Delta x^3} \\ b_i &= -\frac{(2f'_i + f'_{i+1})}{\Delta x} + \frac{3(f_{i+1} - f_i)}{\Delta x^2} \end{aligned} \tag{6.7}$$

Once a_i and b_i are known in terms of f^n and f'^n (f and f' at time $t - \Delta t$), the value of f^{n+1} is simply given by shifting the cubic polynomial and its derivative. For

the linear advection equation with $u = constant$, equation (6.5) is equivalent to (6.3) and f'^n can also be used to estimate f'^{n+1}. Thus,

$$\begin{aligned} f_i^{n+1} &= F(x_i - u\Delta t) = [(a_i + b_i)\xi + f_i']\xi + f_i \\ f_i'^{n+1} &= \frac{dF(x_i - u\Delta t)}{dx} = (3a_i\xi + 2b_i)\xi + f_i' \end{aligned} \tag{6.8}$$

where $\xi = -u\Delta t$.

This expression is derived for $u < 0$. For $u \geq 0$, we obtain a similar expression but we should replace Δx by $-\Delta x$ and $i + 1$ by $i - 1$ in (6.7).

This scheme is called CIP0 and has been found reasonably accurate for many problems including nonlinear problems. However, for problems with discontinuous fronts, the spatial derivative is not continuous at the front and it has different values ${f'}_R$ and ${f'}_L$ for the right side and left side of the front respectively. Therefore, some improved CIP schemes have been proposed, i.e. CIP1 and CIP2.

Non-linear problem

Consider the hyperbolic equation,

$$\frac{\partial f}{\partial t} + \frac{\partial (fu)}{\partial x} = g \tag{6.9}$$

where the advection velocity u and the source term g can be a function of f. This equation can be rewritten as,

$$\frac{\partial f}{\partial t} + u\frac{\partial f}{\partial x} = G = g - f\frac{\partial u}{\partial x} \tag{6.10}$$

As it was explained before, f' should satisfy the spatial derivative of the master equation (6.10) as,

$$\frac{\partial f'}{\partial t} + u\frac{\partial f'}{\partial x} = G' - f'\frac{\partial u}{\partial x} \tag{6.11}$$

In order to solve (6.10) and (6.11), the CIP scheme splits the problem into two

phases; the non-advection phase and the advection phase. The non-advection phase is solved by a finite difference scheme while the advection phase is solved by the CIP solver.

- Non-advection phase

The equations to be solved are,

$$\begin{aligned} \left(\frac{\partial f}{\partial t}\right)_{(1)} &= G = g - f\frac{\partial u}{\partial x} \\ \left(\frac{\partial f'}{\partial t}\right)_{(1)} &= G' - f'\frac{\partial u}{\partial x} \end{aligned} \tag{6.12}$$

The first equation is simply solved using finite differencing

$$f_i^* = f_i^n + G_i^n \Delta t \tag{6.13}$$

where the superscript (*) stands for the time after one step in the non-advection phase.

The second equation in (6.12) can be solved again by finite differencing the equation or by finding f' in terms of G' from equation (6.13). Thus we have,

$$\frac{(f_i'^* - f_i'^n)}{\Delta t} = \frac{(f_{i+1}^* - f_{i-1}^* - f_{i+1}^n + f_{i-1}^n)}{2\Delta x \Delta t} - f_i'^n \frac{(u_{i+1}^n - u_{i-1}^n)}{2\Delta x} \tag{6.14}$$

After f^* and f'^* are found, they will be taken to the advection phase.

- Advection phase

The equations to be solved are as follows,

$$\begin{aligned} \left(\frac{\partial f}{\partial t}\right)_{(2)} + u\frac{\partial f}{\partial x} &= 0 \\ \left(\frac{\partial f'}{\partial t}\right)_{(2)} + u\frac{\partial f'}{\partial x} &= 0 \end{aligned} \tag{6.15}$$

Note that summing equations (6.12) and (6.15) give equations (6.10) and (6.11) since,

$$\begin{aligned} \frac{\partial f}{\partial t} &= \left(\frac{\partial f}{\partial t}\right)_{(1)} + \left(\frac{\partial f}{\partial t}\right)_{(2)} \\ \frac{\partial f'}{\partial t} &= \left(\frac{\partial f'}{\partial t}\right)_{(1)} + \left(\frac{\partial f'}{\partial t}\right)_{(2)} \end{aligned} \tag{6.16}$$

The CIP solver is applied to the advection phase and the interpolated profile is determined from equations (6.7- 6.8) using f^* and f'^* on the right-hand side.

These two phases complete one time step of the calculations. Then we replace f^{n+1} and f'^{n+1} by f^n and f'^n and we return to the non-advection phase again. The solution process is given in table 6.1.1.

Table 6.1.1 Solution process in the non-linear 1D problems

(1) Set initial conditions f_i^n and $f_i'^n$ for all the nodal points i (the superscript n denotes the solution at time $t - \Delta t$).

(2) From the non-advection phase, obtain f_i^* and $f_i'^*$ from the equations (6.13) and (6.14) respectively (for all the nodal points i).

(3) From the advection phase, use the CIP solver to obtain f_i^{n+1} and $f_i'^{n+1}$ from the equations (6.7) and (6.8) for all the nodal points i (the superscript $n+1$ denotes the solution at time t).

(4) Repeat (2) to (4) for the next time step.

Note that the consistency and stability of the CIP scheme are studied in Appendices A and B respectively.

6.1.2 Two-dimensional CIP solver

For simplicity we use a rectangular grid with spacing Δx and Δy and grid points (i,j), $(i+1,j)$, $(i+1,j+1)$ and $(i,j+1)$. We consider a two-dimensional hyperbolic equation as follows,

$$\frac{\partial f}{\partial t} + u\frac{\partial f}{\partial x} + v\frac{\partial f}{\partial y} = g \tag{6.17}$$

When $u < 0$ and $v < 0$, we interpolate $f(x,y)$ with a cubic polynomial within a grid cell as,

$$\begin{aligned} F_{i,j}(x,y) = &[(A1_{i,j}X + A2_{i,j}Y + A3_{i,j})X + A4_{i,j}Y + \partial_x f_{i,j}]X \\ &+[(A5_{i,j}Y + A6_{i,j}X + A7_{i,j})Y + \partial_y f_{i,j}]Y + f_{i,j} \end{aligned} \tag{6.18}$$

where $X = x - x_{i,j}$, $Y = y - y_{i,j}$ and $\partial_x f$ and $\partial_y f$ are $\frac{\partial f}{\partial x}$ and $\frac{\partial f}{\partial y}$ respectively. If the value of f is known at all grid points, $f_{i,j}$ for $i = 1, \ldots, i_{max}$ and $j = 1, \ldots, j_{max}$, only nine parameters A1, ..., A7, $\partial_x f$ and $\partial_y f$ need to be determined.

In the CIP method, the first spatial derivatives should satisfy the derivative of the master equation and thus we have,

$$\begin{aligned} \frac{\partial f_{,x}}{\partial t} + u\frac{\partial f_{,x}}{\partial x} + v\frac{\partial f_{,x}}{\partial y} &= \partial_x g - f_{,x}\frac{\partial u}{\partial x} - f_{,y}\frac{\partial v}{\partial x} \\ \frac{\partial f_{,y}}{\partial t} + u\frac{\partial f_{,y}}{\partial x} + v\frac{\partial f_{,y}}{\partial y} &= \partial_y g - f_{,x}\frac{\partial u}{\partial y} - f_{,y}\frac{\partial v}{\partial y} \end{aligned} \tag{6.19}$$

If $\partial_x f$ and $\partial_y f$ are known at all grid points, we only need to determine the coefficients $A1, \ldots, A7$. There are different two-dimensional CIP solvers based on the assumptions made to find these coefficients. For the choice of having a continuous f at grid points $(i+1,j)$, $(i,j+1)$ and $(i+1,j+1)$ and continuous $\partial_x f$ and $\partial_y f$ at grid points $(i+1,j)$ and $(i,j+1)$ we obtain,

$$
\begin{aligned}
A1_{i,j} &= [-2d_i + \partial_x(f_{i+1,j} + f_{i,j})\Delta x]/\Delta x^3 \\
A2_{i,j} &= [A8_{i,j} - \partial_x d_j \Delta x]/\Delta x^2 \Delta y \\
A3_{i,j} &= [3d_i - \partial_x(f_{i+1,j} + 2f_{i,j})\Delta x]/\Delta x^2 \\
A4_{i,j} &= [-A8_{i,j} + \partial_x d_j \Delta x + \partial_y d_i \Delta y]/\Delta x \Delta y \\
A5_{i,j} &= [-2d_j + \partial_y(f_{i,j+1} + f_{i,j})\Delta y]/\Delta y^3 \\
A6_{i,j} &= [A8_{i,j} - \partial_y d_i \Delta y]/\Delta x \Delta y^2 \\
A7_{i,j} &= [3d_j - \partial_y(f_{i,j+1} + 2f_{i,j})\Delta y]/\Delta y^2 \\
A8_{i,j} &= f_{i,j} - f_{i+1,j} - f_{i,j+1} + f_{i+1,j+1}
\end{aligned}
\tag{6.20}
$$

where $d_i = f_{i+1,j} - f_{i,j}$ and $d_j = f_{i,j+1} - f_{i,j}$. These equations are for $u < 0$ and $v < 0$. For $u \geq 0$, we must change $i+1$ to $i-1$ and Δx to $-\Delta x$. Similarly for $v \geq 0$, $j-1$ and $-\Delta y$ are used instead of $j+1$ and Δy.

We split equations (6.17) and (6.19) into two phases; the advection phase and the non-advection phase. After the non-advection phase is solved by a finite difference scheme, the CIP solver is applied to the advection phase.

- Non-advection phase

The equations to be solved are,

$$
\begin{aligned}
\left(\frac{\partial f}{\partial t}\right)_{(1)} &= g \\
\left(\frac{\partial f_{,x}}{\partial t}\right)_{(1)} &= \partial_x g - f_{,x}\frac{\partial u}{\partial x} - f_{,y}\frac{\partial v}{\partial x} \\
\left(\frac{\partial f_{,y}}{\partial t}\right)_{(1)} &= \partial_y g - f_{,x}\frac{\partial u}{\partial y} - f_{,y}\frac{\partial v}{\partial y}
\end{aligned}
\tag{6.21}
$$

where the subscript (1) in these equations denotes the non-advection part of the time derivatives $\frac{\partial f}{\partial t}$, $\frac{\partial f_{,x}}{\partial t}$ and $\frac{\partial f_{,y}}{\partial t}$.

These equations are solved using a finite difference method and the quantities f, $\partial f_{,x}$ and $\partial f_{,y}$ are advanced as

$$
\begin{aligned}
f^*_{i,j} &= f^n_{i,j} + g_{i,j}\Delta t \\
\partial_x f^*_{i,j} &= \partial_x f^n_{i,j} - \frac{f^*_{i+1,j} - f^*_{i-1,j} - f^n_{i+1,j} + f^n_{i-1,j}}{2\Delta x} \\
&\quad - \partial_x f^n_{i,j}\frac{(u_{i+1,j} - u_{i-1,j})\Delta t}{2\Delta x} - \partial_y f^n_{i,j}\frac{(v_{i+1,j} - v_{i-1,j})\Delta t}{2\Delta x} \\
\partial_y f^*_{i,j} &= \partial_y f^n_{i,j} - \frac{f^*_{i,j+1} - f^*_{i,j-1} - f^n_{i,j+1} + f^n_{i,j-1}}{2\Delta y} \\
&\quad - \partial_x f^n_{i,j}\frac{(u_{i,j+1} - u_{i,j-1})\Delta t}{2\Delta y} - \partial_y f^n_{i,j}\frac{(v_{i,j+1} - v_{i,j-1})\Delta t}{2\Delta y}
\end{aligned}
\tag{6.22}
$$

where the superscript (*) stands for the time after one step in the non-advection phase. After f^*, $\partial_x f^*$ and $\partial_y f^*$ are found, they will be taken to the advection phase.

- Advection phase

The equations to be solved are as follows,

$$
\begin{aligned}
\left(\frac{\partial f}{\partial t}\right)_{(2)} + u\frac{\partial f}{\partial x} + v\frac{\partial f}{\partial y} &= 0 \\
\left(\frac{\partial f_{,x}}{\partial t}\right)_{(2)} + u\frac{\partial f_{,x}}{\partial x} + v\frac{\partial f_{,x}}{\partial y} &= 0 \\
\left(\frac{\partial f_{,y}}{\partial t}\right)_{(2)} + u\frac{\partial f_{,y}}{\partial x} + v\frac{\partial f_{,y}}{\partial y} &= 0
\end{aligned}
\tag{6.23}
$$

where the subscript (2) in these equations denotes the advection part of the time derivatives $\frac{\partial f}{\partial t}$, $\frac{\partial f_{,x}}{\partial t}$ and $\frac{\partial f_{,y}}{\partial t}$. Note that summing the non-advection equations (6.21) and the advection equations (6.23) give the governing equations (6.17) and (6.19) since,

$$
\begin{aligned}
\frac{\partial f}{\partial t} &= \left(\frac{\partial f}{\partial t}\right)_{(1)} + \left(\frac{\partial f}{\partial t}\right)_{(2)} \\
\frac{\partial f_{,x}}{\partial t} &= \left(\frac{\partial f_{,x}}{\partial t}\right)_{(1)} + \left(\frac{\partial f_{,x}}{\partial t}\right)_{(2)} \\
\frac{\partial f_{,y}}{\partial t} &= \left(\frac{\partial f_{,y}}{\partial t}\right)_{(1)} + \left(\frac{\partial f_{,y}}{\partial t}\right)_{(2)}
\end{aligned}
\tag{6.24}
$$

The CIP solver is applied to the advection phase; coefficients $A1, \ldots, A7$ are determined from equations (6.20) and after a short time step Δt we update f and its spatial derivatives as,

$$
\begin{aligned}
f_{i,j}^{n+1} &= F_{i,j}(x_{i,j} - u\Delta t, y_{i,j} - v\Delta t) \\
\partial_x f_{i,j}^{n+1} &= \partial_x F_{i,j}(x_{i,j} - u\Delta t, y_{i,j} - v\Delta t) \\
\partial_y f_{i,j}^{n+1} &= \partial_y F_{i,j}(x_{i,j} - u\Delta t, y_{i,j} - v\Delta t)
\end{aligned}
\tag{6.25}
$$

To follow the calculations for the next time step, we replace f^{n+1}, $\partial_x f^{n+1}$ and $\partial_y f^{n+1}$ by f^n, $\partial_x f^n$ and $\partial_y f^n$ and we start from the non-advection phase again.

The two-dimensional solver described here is for the choice of having a continuous f at grid points $(i+1, j)$, $(i, j+1)$ and $(i+1, j+1)$ and continuous $\partial_x f$ and $\partial_y f$ at grid points $(i+1, j)$ and $(i, j+1)$. Based on the assumptions made, there are some other two-dimensional solvers.

Type-A solver interpolates f within a grid cell as,

$$
\begin{aligned}
F(x, y) = {} & C_{3,0}X^3 + C_{2,0}X^2 + \partial_x f_{i,j}X + f_{i,j} + C_{0,3}Y^3 \\
& + C_{0,2}Y^2 + \partial_y f_{i,j}Y + C_{2,1}X^2Y + C_{1,1}XY + C_{1,2}XY^2
\end{aligned}
\tag{6.26}
$$

where the C coefficients are determined from continuity of f at grid points (i, j), $(i+1, j)$, $(i, j+1)$ and $(i+1, j+1)$ while $\partial_x f$ and $\partial_y f$ are continuous at grid points

(i,j), $(i+1,j)$ and $(i,j+1)$.

In order to develop a more accurate interpolation, we consider the continuity of $\partial_x f$ and $\partial_y f$ at the grid point $(i+1,j+1)$ in addition to the above conditions. This interpolation is called *Type-B* and the interpolation function is expressed as follows,

$$\begin{aligned} F(x,y) = C_{3,0}X^3 + C_{2,0}X^2 + \partial_x f_{i,j}X + f_{i,j} + C_{0,3}Y^3 + C_{0,2}Y^2 + \partial_y f_{i,j}Y \\ +C_{3,1}X^3Y + C_{2,1}X^2Y + C_{1,2}XY^2 + C_{1,1}XY + C_{1,3}XY^3 \end{aligned} \tag{6.27}$$

where the C coefficients are found from the continuity of f, $\partial_x f$ and $\partial_y f$ at grid points (i,j), $(i+1,j)$, $(i,j+1)$ and $(i+1,j+1)$.

6.1.3 The CIP solver for compressible and incompressible flows

Different CIP solvers have been proposed for the compressible and incompressible fluid flows. Among these solvers, we present the most powerful one; the CIP-CUP (Cubic Interpolated Propagation / Combined Unified Procedure) method [25], [27].

The CIP-CUP method is a semi-implicit solver that considers the governing equations of fluid flow as follows,

$$\begin{aligned} \frac{\partial \rho}{\partial t} &+ \mathbf{u}\cdot\nabla\rho = -\rho\nabla\cdot\mathbf{u} \\ \frac{\partial \mathbf{u}}{\partial t} &+ \mathbf{u}\cdot\nabla\mathbf{u} = -\frac{\nabla p}{\rho} + \frac{\mathbf{F}}{\rho} \\ \frac{\partial p}{\partial t} &+ \mathbf{u}\cdot\nabla p = -\rho\, C_s^2\nabla\cdot\mathbf{u} \end{aligned} \tag{6.28}$$

where ρ is the density, $\mathbf{u}$ is the velocity vector, p is the pressure and C_s is the local sound speed. For the Navier-Stokes equations, $\mathbf{F}$ contains viscosity effects, surface tensions and external forces. For the Euler equations, there is no viscosity effect and $\mathbf{F}$ only contains the surface tensions and external forces.

The CIP-CUP solver splits the problem into three different parts; the convection

part, the acoustic part and the remaining part. The convection part is solved by the CIP method, the acoustic part is solved by the CUP method while the remaining part is solved by a finite difference scheme or a finite volume method.

- The convection part

The equations to be solved are,

$$\begin{aligned}
\left(\frac{\partial \rho}{\partial t}\right)_{(c)} + \mathbf{u}\cdot\nabla\rho &= 0 \\
\left(\frac{\partial \mathbf{u}}{\partial t}\right)_{(c)} + \mathbf{u}\cdot\nabla\mathbf{u} &= 0 \\
\left(\frac{\partial p}{\partial t}\right)_{(c)} + \mathbf{u}\cdot\nabla p &= 0
\end{aligned} \tag{6.29}$$

where the subscript (c) denotes the convection part of the time derivatives.

The CIP solver explained in (6.1.2) is used to solve the convection part. We also need to update the spatial derivatives of quantities ρ, $\mathbf{u}$ and p before we proceed to the remaining part.

- The remaining part

The remaining part is governed by the equation,

$$\left(\frac{\partial \mathbf{u}}{\partial t}\right)_{(r)} = \frac{\mathbf{F}}{\rho} \tag{6.30}$$

where the subscript (r) denotes the remaining part of the time derivative term $\frac{\partial \mathbf{u}}{\partial t}$. For the Navier-Stokes equations, $\mathbf{F}$ contains viscosity effects, surface tensions and external forces. For the Euler equations, there is no viscosity effect and $\mathbf{F}$ only contains the surface tensions and external forces. This equation can be solved by a finite difference scheme or a finite volume method. After the velocity is updated, we proceed to the acoustic part.

- The acoustic part

The governing equations of the acoustic part are,

$$\begin{aligned}
\left(\frac{\partial \rho}{\partial t}\right)_{(a)} &= -\rho \nabla \cdot \mathbf{u} \\
\left(\frac{\partial \mathbf{u}}{\partial t}\right)_{(a)} &= -\frac{\nabla p}{\rho} \\
\left(\frac{\partial p}{\partial t}\right)_{(a)} &= -\rho\, C_s^2 \nabla \cdot \mathbf{u}
\end{aligned} \tag{6.31}$$

where the subscript (a) denotes the acoustic part of the time derivatives. Note that summing the governing equations of the convection part, remaining part and the acoustic part yields the equations (6.28) since,

$$\begin{aligned}
\frac{\partial \rho}{\partial t} &= \left(\frac{\partial \rho}{\partial t}\right)_{(c)} + \left(\frac{\partial \rho}{\partial t}\right)_{(a)} \\
\frac{\partial \mathbf{u}}{\partial t} &= \left(\frac{\partial \mathbf{u}}{\partial t}\right)_{(c)} + \left(\frac{\partial \mathbf{u}}{\partial t}\right)_{(a)} + \left(\frac{\partial \mathbf{u}}{\partial t}\right)_{(r)} \\
\frac{\partial p}{\partial t} &= \left(\frac{\partial p}{\partial t}\right)_{(c)} + \left(\frac{\partial p}{\partial t}\right)_{(a)}
\end{aligned} \tag{6.32}$$

These equations are solved by the CUP method, which is an implicit finite difference method. Discretizing the time derivatives on the left hand side of these equations and estimating the right hand side for the future values (values to be found at the end of this phase), we obtain

$$\begin{aligned}
\frac{\rho^{n+1} - \rho^*}{\Delta t} &= -\rho^* \nabla \cdot \mathbf{u}^{n+1} \\
\frac{\mathbf{u}^{n+1} - \mathbf{u}^*}{\Delta t} &= -\frac{\nabla p^{n+1}}{\rho^*} \\
\frac{p^{n+1} - p^*}{\Delta t} &= -\rho^*\, C_s^{*2}\, \nabla \cdot \mathbf{u}^{n+1}
\end{aligned} \tag{6.33}$$

where n is the number of the time step, Δt is the time interval, and the quantities with the superscript (*) are the values after solving the convection and the remaining

parts. At each time step Δt, the acoustic phase should be solved after the other phases since at the end of this phase, we satisfy the divergence-free condition for the velocity in incompressible fluid flows.

In equations (6.33), the velocity, the pressure and the density at time $n+1$ are dependent. In order to find the pressure, we take the divergence of the second equation and substitute it into the third equation. The pressure equation will then be,

$$\frac{p^{n+1} - p^*}{\Delta t} = -\rho^* \, C_s^{*2} \, \nabla \cdot \mathbf{u}^* + \rho^* \, C_s^{*2} \, \Delta t \, \nabla \cdot \frac{\nabla p^{n+1}}{\rho^*} \tag{6.34}$$

After we find p^{n+1}, $\mathbf{u}^{n+1}$ is obtained from the second equation of (6.33). Also, the density is updated explicitly by

$$\rho^{n+1} = \rho^* + \frac{p^{n+1} - p^*}{C_s^{*2}} \tag{6.35}$$

For incompressible fluid flows, the sound speed C_s is infinite, and the pressure equation (6.34) is reduced to

$$\nabla \cdot \frac{\nabla p^{n+1}}{\rho^*} = \frac{\nabla \cdot \mathbf{u}^*}{\Delta t} \tag{6.36}$$

Therefore, CIP-CUP method is applicable to both compressible and incompressible fluids.

Calculation of p^{n+1}, $\mathbf{u}^{n+1}$ and ρ^{n+1} completes one time step of the CIP-CUP method. For the next time step, we could repeat the calculation from the convection part using above values as initial values. The solution process is given in table 6.1.3.

Table 6.1.3 Solution process in the CIP-CUP method

(1) Set initial conditions ρ_i^n, $\mathbf{u}_i^n$ and p_i^n and their spatial derivatives for all the nodal points i (the superscript n denotes the solution at time $t - \Delta t$).

(2) From the convection phase use the CIP solver to get $\hat{\rho}_i$, $\hat{\mathbf{u}}_i$ and $\hat{p}_i$ and their spatial derivatives (for all the nodal points i).

(3) From the remaining phase, use a finite difference method to get ρ_i^*, $\mathbf{u}_i^*$ and p_i^* and their spatial derivatives for all the nodal points i ($\rho_i^* = \hat{\rho}_i$, $p_i^* = \hat{p}_i$).

(4) From the acoustic phase, get ρ_i^{n+1}, $\mathbf{u}_i^{n+1}$ and p_i^{n+1} and their spatial derivatives from the equations (6.33)- (6.35) for all the nodal points i (the superscript $n+1$ denotes the solution at time t).

(5) Repeat (2) to (5) for the next time step.

6.2 Linking the finite element method to the CIP method

The CIP method was originally proposed for the finite difference method; both the convection phase and the non-convection phase are solved using the finite difference method. However in some problems, satisfying the boundary conditions for the incompressible Navier-Stokes equations is easier using the finite element methods. In addition, in problems for which the domain is complicated and mesh grading is required, the finite difference methods are not as flexible as the finite element methods.

The CIP method is here extended for use in the finite element method and the finite element shape functions for the third order interpolation are introduced in [24], [16]. This shape function is defined by the product of the linear shape function and a new second order shape function. In this chapter, these functions are used to solve the two-dimensional incompressible Navier-Stokes equations.

6.2.1 The governing equations

The non-dimensional continuity and momentum equations are written as,

$$\begin{aligned} &\nabla \cdot \mathbf{u} = 0 \\ &\frac{\partial \mathbf{u}}{\partial t} + (\mathbf{u} \cdot \nabla)\mathbf{u} = -\nabla p + \frac{1}{Re} \nabla^2 \mathbf{u} \end{aligned} \tag{6.37}$$

where $\mathbf{u}$, p and Re are the velocity vector, pressure and the Reynolds number respectively. External force is not considered here.

The shape function for the third order interpolation function in CIP-FEM is defined for the velocity $\mathbf{u}$ and its derivatives. Therefore, we need the spatial derivatives of the momentum equation as follows,

$$\begin{aligned} \frac{\partial \mathbf{u}_x}{\partial t} + (\mathbf{u} \cdot \nabla)\mathbf{u}_x &= -(\mathbf{u}_x \cdot \nabla)\mathbf{u} - \nabla p_x + \frac{1}{Re} \nabla^2 \mathbf{u}_x \\ \frac{\partial \mathbf{u}_y}{\partial t} + (\mathbf{u} \cdot \nabla)\mathbf{u}_y &= -(\mathbf{u}_y \cdot \nabla)\mathbf{u} - \nabla p_y + \frac{1}{Re} \nabla^2 \mathbf{u}_y \end{aligned} \tag{6.38}$$

where the subscripts x and y show the derivative in each direction.

We split the governing equations into an advection phase, a non-advection phase and the Poisson equation of pressure. The advection phase is solved by the CIP method (CIP-FEM), the non-advection phase by the Galerkin method, and the Poisson equation by the simultaneous relaxation method of the GSMAC (generalized simplified marker and cell) method [18].

- The advection phase

The governing equations of the advection phase are,

$$\begin{aligned} &\frac{\hat{\mathbf{u}} - \mathbf{u}^n}{\Delta t} + (\mathbf{u}^n \cdot \nabla)\mathbf{u}^n = 0 \\ &\frac{\hat{\mathbf{u}}_x - \mathbf{u}_x^n}{\Delta t} + (\mathbf{u}^n \cdot \nabla)\mathbf{u}_x^n = 0 \\ &\frac{\hat{\mathbf{u}}_y - \mathbf{u}_y^n}{\Delta t} + (\mathbf{u}^n \cdot \nabla)\mathbf{u}_y^n = 0 \end{aligned} \tag{6.39}$$

where the superscript (n) stands for the solution at time $t - \Delta t$ and the superscript

($\hat{}$) stands for the solution after one step in the advection phase.

The CIP-FEM is applied to discretize and solve these equations. First, we describe the CIP method. Considering the advection equation for a potential ϕ,

$$\frac{\partial \phi}{\partial t} + \mathbf{u} \cdot \nabla \phi = 0 \tag{6.40}$$

The solution at time "t" is approximated as,

$$\phi(x_i, t) \sim \phi \left(x_i - \int u dt, t - dt \right) \tag{6.41}$$

where x_i denotes the grid point where ϕ is given. The start point $x_* = x_i - \int u dt$ becomes the grid point at the next time step. x_* is called the advection distance and should be calculated along the particle path. However, the exact value of this distance is difficult to obtain and it is approximated explicitly as,

$$\Delta x = x_i - x_* = u_i^n \, \Delta t \tag{6.42}$$

In order for this approximation to be close to the exact value, Δt must be sufficiently small.

In the CIP method, the potential ϕ is interpolated using the third order shape functions, and these functions are defined for the system of coordinates ξ-η. Since the start point x_* is obtained in the x-y coordinate system, we find the corresponding ξ_* and η_* for this point.

The shape function then is defined as,

$$\phi(\xi, \eta) = \sum_a h_a(\xi, \eta)[G_a(\xi, \eta) + E_a(\xi, \eta)\phi_a] \tag{6.43}$$

where h_a is the conventional linear shape function, and G_a and E_a are new shape functions that are second order and linear respectively.

For the element shown in figure 6-2, these functions are as follows,

$$
\begin{aligned}
h_1 &= \frac{1}{4}(1-\xi)(1-\eta) \\
h_2 &= \frac{1}{4}(1+\xi)(1-\eta) \\
h_3 &= \frac{1}{4}(1+\xi)(1+\eta) \\
h_4 &= \frac{1}{4}(1-\xi)(1+\eta)
\end{aligned}
\tag{6.44}
$$

$$
\begin{aligned}
E_1 &= \frac{1}{2}(-\xi-\eta) \\
E_2 &= \frac{1}{2}(\xi-\eta) \\
E_3 &= \frac{1}{2}(\xi+\eta) \\
E_4 &= \frac{1}{2}(-\xi+\eta)
\end{aligned}
\tag{6.45}
$$

$$
\begin{aligned}
G_1 &= \frac{1}{2}(1-\xi^2)[\partial_\xi\phi_1+\phi_1] + \frac{1}{2}(1-\eta^2)[\partial_\eta\phi_1+\phi_1] \\
G_2 &= \frac{1}{2}(-1+\xi^2)[\partial_\xi\phi_2-\phi_2] + \frac{1}{2}(1-\eta^2)[\partial_\eta\phi_2+\phi_2] \\
G_3 &= \frac{1}{2}(-1+\xi^2)[\partial_\xi\phi_3-\phi_3] + \frac{1}{2}(-1+\eta^2)[\partial_\eta\phi_3-\phi_3] \\
G_4 &= \frac{1}{2}(1-\xi^2)[\partial_\xi\phi_4+\phi_4] + \frac{1}{2}(-1+\eta^2)[\partial_\eta\phi_4-\phi_4]
\end{aligned}
\tag{6.46}
$$

Using the CIP-FEM, the velocity $\mathbf{u}$ and its derivatives are updated for the time "t" ($\hat{\mathbf{u}}$, $\hat{\mathbf{u}}_x$ and $\hat{\mathbf{u}}_y$). These values are then taken to the non-advection phase.

- The non-advection phase

The governing equations are as follows,

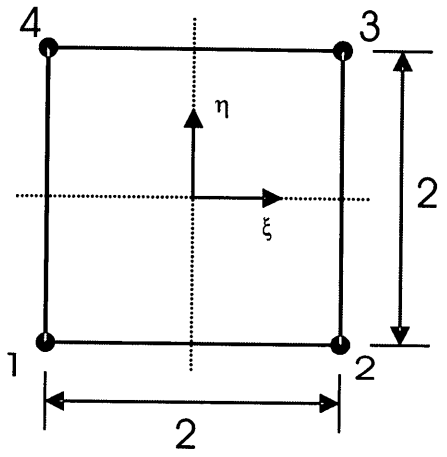

Figure 6-2: The 4-node element used in the finite element discretization

$$
\begin{aligned}
\frac{\tilde{\mathbf{u}} - \hat{\mathbf{u}}}{\Delta t} &= -\nabla p^n + \frac{1}{Re}\nabla^2 \mathbf{u}^n \\
\frac{\mathbf{u}_x^{n+1} - \hat{\mathbf{u}}_x}{\Delta t} &= -(\mathbf{u}_x^n \cdot \nabla)\mathbf{u}^n - \nabla p_x^{n+1} + \frac{1}{Re}\nabla^2 \mathbf{u}_x^n \\
\frac{\mathbf{u}_y^{n+1} - \hat{\mathbf{u}}_y}{\Delta t} &= -(\mathbf{u}_y^n \cdot \nabla)\mathbf{u}^n - \nabla p_y^{n+1} + \frac{1}{Re}\nabla^2 \mathbf{u}_y^n
\end{aligned}
\tag{6.47}
$$

In order to avoid considering the pressure derivatives p_x and p_y as nodal variables and updating them for each time step in the second and third equations, these terms are replaced by the velocity terms from the first equation. Then, the second and third equations are written as,

$$
\begin{aligned}
\frac{\mathbf{u}_x^{n+1} - \hat{\mathbf{u}}_x}{\Delta t} &= -(\mathbf{u}_x^n \cdot \nabla)\mathbf{u}^n + \frac{\partial}{\partial x}\left(\frac{\mathbf{u}^{n+1} - \hat{\mathbf{u}}}{\Delta t}\right) \\
\frac{\mathbf{u}_y^{n+1} - \hat{\mathbf{u}}_y}{\Delta t} &= -(\mathbf{u}_y^n \cdot \nabla)\mathbf{u}^n + \frac{\partial}{\partial y}\left(\frac{\mathbf{u}^{n+1} - \hat{\mathbf{u}}}{\Delta t}\right)
\end{aligned}
\tag{6.48}
$$

The non-advection phase is discretized by the Galerkin method. For the 4-node element shown in figure 6-2, we use the four corner points to interpolate the velocity when the pressure is constant within each element. Then the velocity $\mathbf{u}$ and its derivatives in (6.47- 6.48) are replaced by

$$\begin{aligned}
\mathbf{u} &= \sum_{i=1}^{4} h_i \mathbf{u}_i \\
\mathbf{u}_x &= \sum_{i=1}^{4} h_{xi} \mathbf{u}_i \\
\mathbf{u}_y &= \sum_{i=1}^{4} h_{yi} \mathbf{u}_i
\end{aligned} \tag{6.49}$$

After discretization by the Galerkin method, the first equation in (6.47) and equations (6.48) are written respectively as,

$$\begin{aligned}
M_{ij} \left(\frac{\tilde{\mathbf{u}} - \hat{\mathbf{u}}}{\Delta t} \right)_j &= C_i \, p^n - \frac{1}{Re} \, D_{ij} \, \mathbf{u}_j^n + S_i \\
M_{ij} \left(\frac{\mathbf{u}_x^{n+1} - \hat{\mathbf{u}}_x}{\Delta t} \right)_j &= -A_{ij} \, \mathbf{u}_{xi}^n \, \mathbf{u}_j^n + A_{ij} \left(\frac{\mathbf{u}^{n+1} - \hat{\mathbf{u}}}{\Delta t} \right)_j \\
M_{ij} \left(\frac{\mathbf{u}_y^{n+1} - \hat{\mathbf{u}}_y}{\Delta t} \right)_j &= -A_{ij} \, \mathbf{u}_{yi}^n \, \mathbf{u}_j^n + A_{ij} \left(\frac{\mathbf{u}^{n+1} - \hat{\mathbf{u}}}{\Delta t} \right)_j
\end{aligned} \tag{6.50}$$

where p presents the constant pressure within the element, the lower subscripts i and j show the local node numbers and superscript n is the time step number. Except for the first term on the right-hand side of the second and third equations, repeated subscripts mean summation. The matrices M_{ij}, C_i, A_{ij} and D_{ij} are the mass matrix, the gradient matrix, the advection matrix and the diffusion matrix respectively and are written as,

$$\begin{aligned}
M_{ij} &= \int_{\Omega^e} h_i \, h_j \, d\Omega \\
C_i &= \int_{\Omega^e} \nabla h_i \, d\Omega \\
A_{ij} &= \int_{\Omega^e} h_i \, \nabla h_j \, d\Omega \\
D_{ij} &= \int_{\Omega^e} \nabla h_i \cdot \nabla h_j \, d\Omega
\end{aligned} \tag{6.51}$$

where S_i contains the boundary terms. Note that the M_{ij} matrix shown here is the consistent mass matrix. We can use the lumped mass matrix instead and replace M_{ij} by $\overline{M_{ij}}$ in equations (6.50). For a non-distorted mesh, the M_{ij} matrix is the same for all the elements and therefore the assemblage will be easier. Note that in the traditional finite element methods (solution is dominant by the stiffness matrix), the lumped mass matrix is preferred since using the lumped mass matrix instead of the consistent one, reduces the numerical operations for the solution significantly.

In the non-advection phase, first the velocity $\tilde{\mathbf{u}}$ is obtained from the first equation in (6.50), then the divergence of the velocity, $\nabla \cdot \tilde{\mathbf{u}}$, is calculated. The simultaneous relaxation method is used to satisfy the continuity equation ($\nabla \cdot \tilde{\mathbf{u}} = 0$) and to modify the velocity $\tilde{\mathbf{u}}$. This method is explained later on in this section.

After the simultaneous relaxation method has been applied, we find the modified velocity $\mathbf{u}^{n+1}$ and pressure p^{n+1}. The velocity $\mathbf{u}^{n+1}$ is then used in (6.50) to obtain $\mathbf{u}_x^{n+1}$ and $\mathbf{u}_y^{n+1}$. The calculations for one time step are complete now and for the next time step, we take the values $\mathbf{u}^{n+1}$, p^{n+1}, $\mathbf{u}_x^{n+1}$ and $\mathbf{u}_y^{n+1}$ to the advection phase and we repeat the calculations for the new time step.

- The simultaneous relaxation method

This method is used to satisfy the continuity equation $\nabla \cdot \tilde{\mathbf{u}} = 0$. After obtaining $\tilde{\mathbf{u}}$ in the non-advection phase, this velocity is modified as follows,

$$\begin{aligned} \nabla^2 \phi^{(m)} &= \nabla \cdot \tilde{\mathbf{u}}^{(m)} \\ p^{(m+1)} &= p^{(m)} + \phi^{(m)}/\Delta t \\ \tilde{\mathbf{u}}^{(m+1)} &= \tilde{\mathbf{u}}^{(m)} - \nabla \phi^{(m)} \end{aligned} \tag{6.52}$$

where the superscript m represents the repeat level and ϕ is the velocity potential. The initial values are defined as,

$$\begin{cases} \tilde{\mathbf{u}}^{(0)} = \tilde{\mathbf{u}} \\ p^{(0)} = p^n \end{cases} \tag{6.53}$$

We first calculate the divergence of the velocity $\tilde{\mathbf{u}}$, then we obtain the velocity potential ϕ from the first equation in (6.52). Using the second and third equations, the velocity and pressure are modified. We repeat the calculations until the velocity $\tilde{\mathbf{u}}$ satisfies the continuity equation; then we have,

$$\begin{aligned} \mathbf{u}^{n+1} &= \tilde{\mathbf{u}}^{(m+1)} \\ p^{n+1} &= p^{(m+1)} \end{aligned} \tag{6.54}$$

The solution process is given in table 6.2.1.

Table 6.2.1 Solution process in the CIP-FEM method for incompressible flows

(1) Set initial conditions $\mathbf{u}^n$ and the spatial derivatives $\mathbf{u}_x^n$ and $\mathbf{u}_y^n$ for all the nodal points (the superscript n denotes the solution at time $t - \Delta t$).

(2) From the advection phase use the CIP solver to obtain $\hat{\mathbf{u}}$ and the spatial derivatives $\hat{\mathbf{u}}_x$ and $\hat{\mathbf{u}}_y$ for all the nodal points using equations (6.43)- (6.46).

(3) From the non-advection phase, use the Galerkin method to obtain $\tilde{\mathbf{u}}$ from the first equation in (6.50).

(4) From the simultaneous relaxation method, obtain the velocity potential ϕ and the modified velocity and pressure from the equations (6.52). After repeating calculations in this step and satisfying the equation $\nabla \cdot \tilde{\mathbf{u}} = 0$, obtain $\mathbf{u}^{n+1}$ and p^{n+1}.

(5) From the non-advection phase, obtain the spatial derivatives $\mathbf{u}_x^{n+1}$ and $\mathbf{u}_y^{n+1}$ from the second and third equations in (6.50).

(6) Repeat (2) to (6) for the next time step.

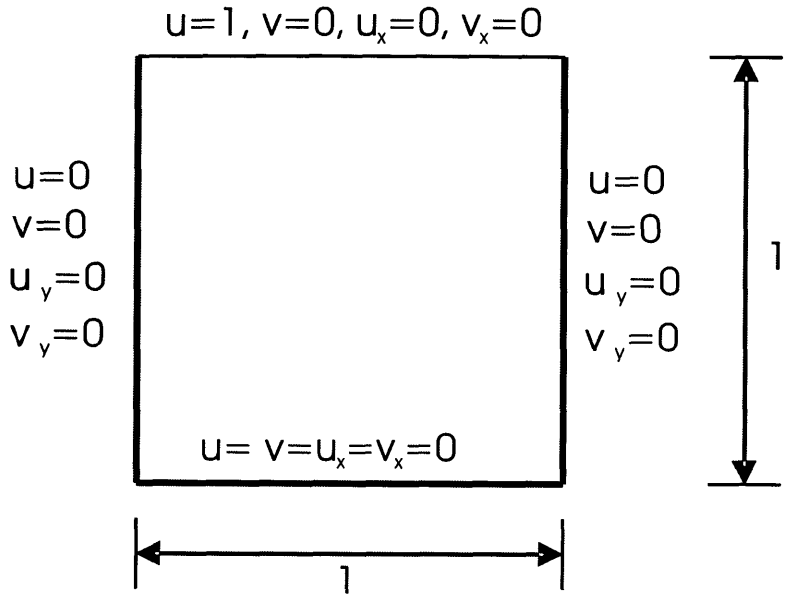

Figure 6-3: The driven cavity flow problem

6.2.2 Numerical solutions

To study the effectiveness of the CIP-FEM method, we consider the driven cavity flow problem shown in figure 6-3. The boundary conditions are shown in this figure and the initial conditions are all zero except for the horizontal velocity $u = 1$ at the upper side of the cavity. This problem is solved for two different cases; $Re = 1000$ and $Re = 10000$. In both cases, the horizontal velocity at the vertical centerline, and the vertical velocity at the horizontal centerline are plotted and compared with the solutions of the *Ghia et al.* and the FCBI method.

- For $Re = 1000$

In this problem, a non-uniform mesh of 30 x 30 elements (figure 6-4 (a)) has been used. For the time increment $\Delta t = 0.005$, the flow is almost steady at $t = 50$. The velocity profiles on the vertical and horizontal center axes of the cavity are shown in figure 6-5 at time $t = 50$. In this figure, the solution obtained by *Ghia et al.* is shown by "o", this solution is assumed to be a very accurate solution. The solution obtained for the FCBI triangular elements for a mesh of 40 x 40 x 2 elements are also given in this figure [20].

As it is clear from figure 6-5, the CIP-FEM method has a higher spatial accuracy than the FCBI scheme. In addition, the spatial derivatives are more accurate in the CIP-FEM method since they are considered as nodal variables in the solution. However, this method requires more computational effort than the FCBI method. For example, in the CIP-FEM method, the problem is solved in two phases; the advection phase and the non-advection phase and in each phase after the nodal velocities have been updated, the nodal spatial derivatives are calculated. In addition, for the non-advection phase the continuity equation is satisfied by the relaxation method and this increases the solution time.

It should be noted that although spatial derivatives of velocities are also considered as nodal variables in the CIP-FEM method, the system of equations for velocities are solved separately from the system of equations for velocity derivatives (after velocities are obtained, then the velocity derivatives are updated). In addition, the velocities in the x and y directions are also uncoupled as seen in equations (6.39) and (6.47). Therefore, the velocity in each direction is obtained separately.

- For $Re = 10000$

A non-uniform mesh of 50 x 50 elements (figure 6-4 (b)) with the time increment $\Delta t = 0.002$ has been used here. After the solution is steady, the velocity profiles on the vertical and horizontal center axes of the cavity are as shown in figure 6-6. In this figure, the *Ghia et al.* and the FCBI solutions are also given. It can be seen that the CIP-FEM method has higher spatial accuracy than the FCBI scheme (the FCBI triangular element has been used here [20]).

In order to solve high Reynolds number flows with the traditional finite element method, we require a very fine mesh. Linking the CIP method to the finite element method increases the stability of the solution in addition to improving the accuracy for the velocities and the derivatives.

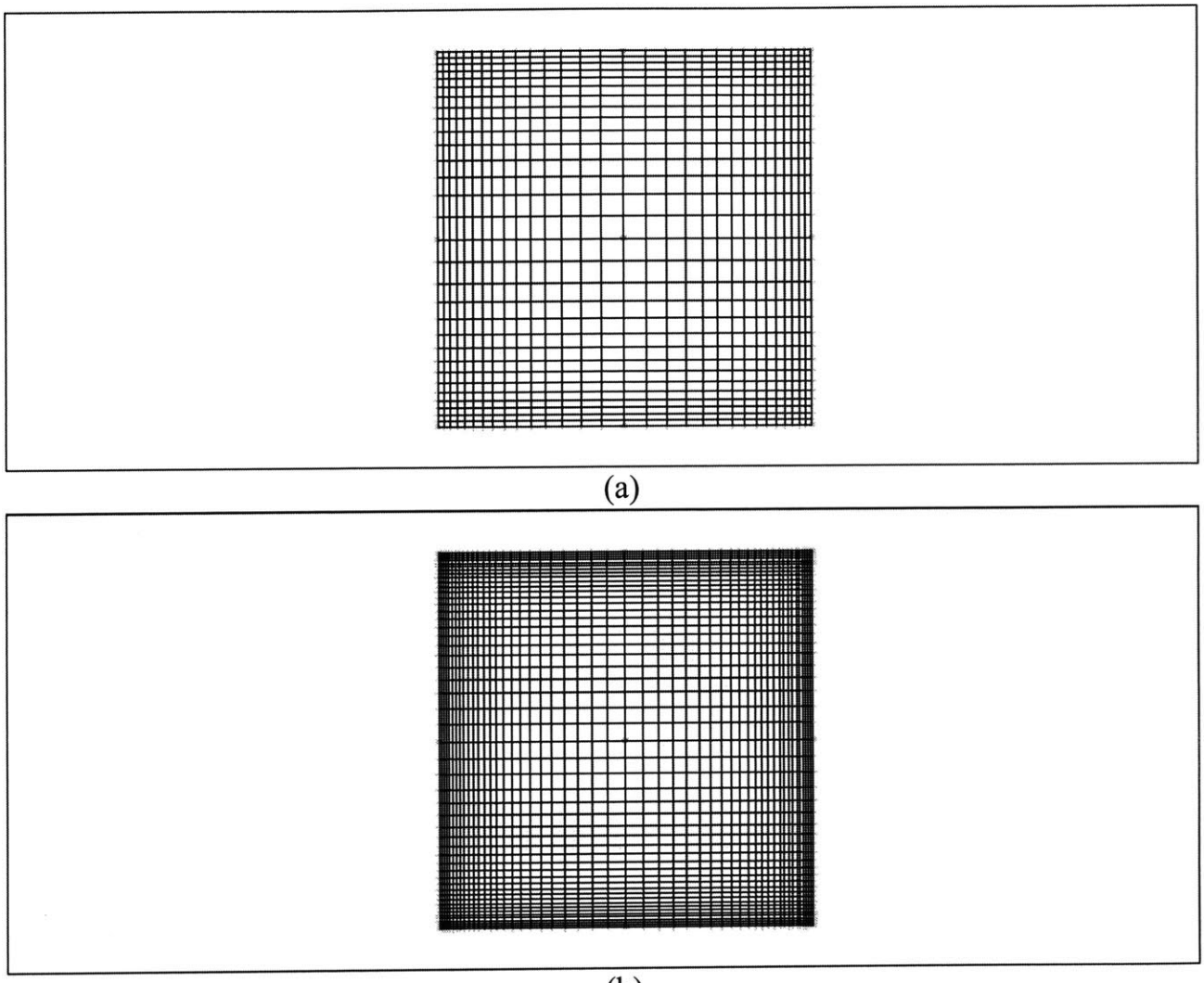

Figure 6-4: The non-uniform meshes used for (a) $Re = 1000$, (b) $Re = 10000$.

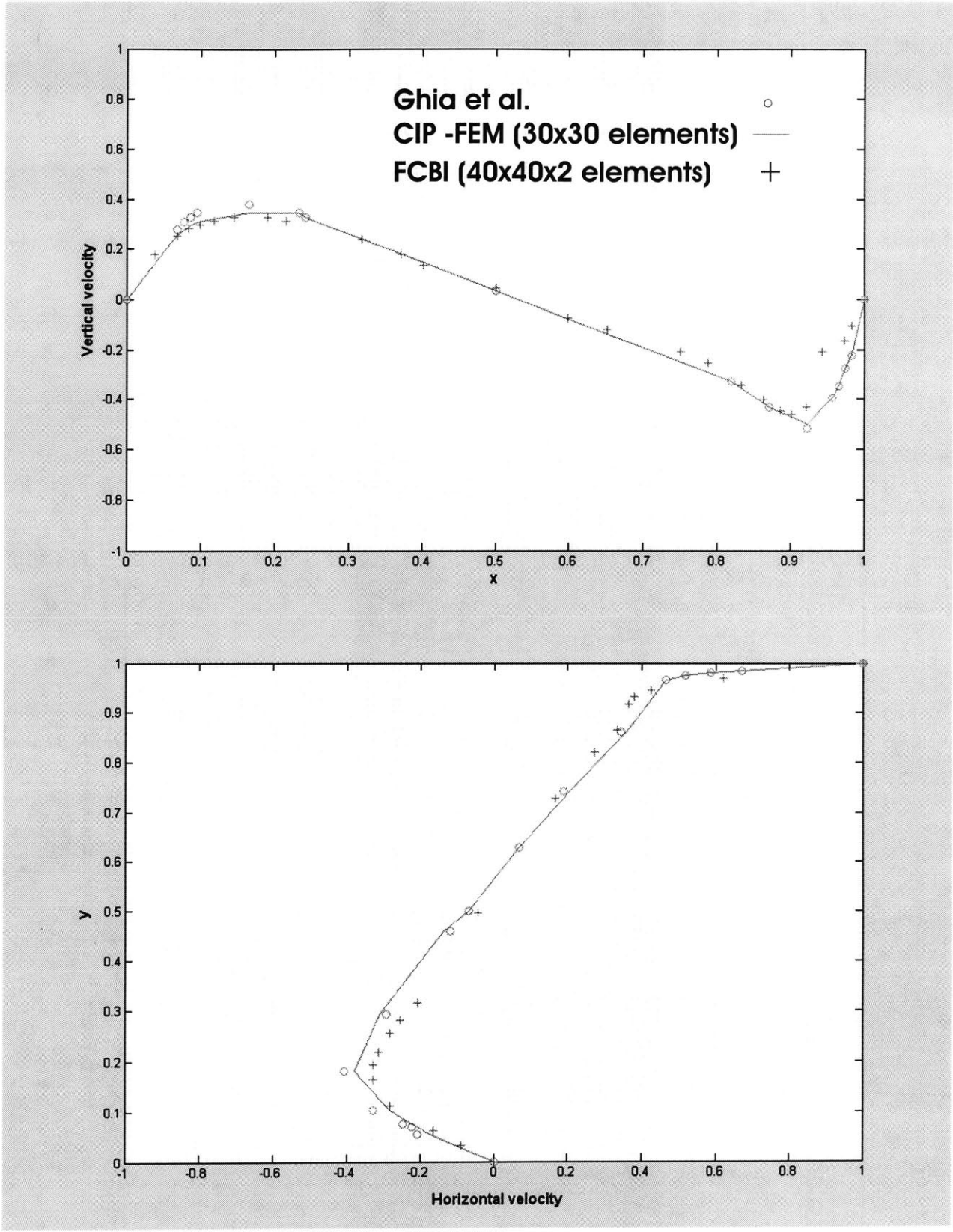

Figure 6-5: Velocity profiles for $Re = 1000$.

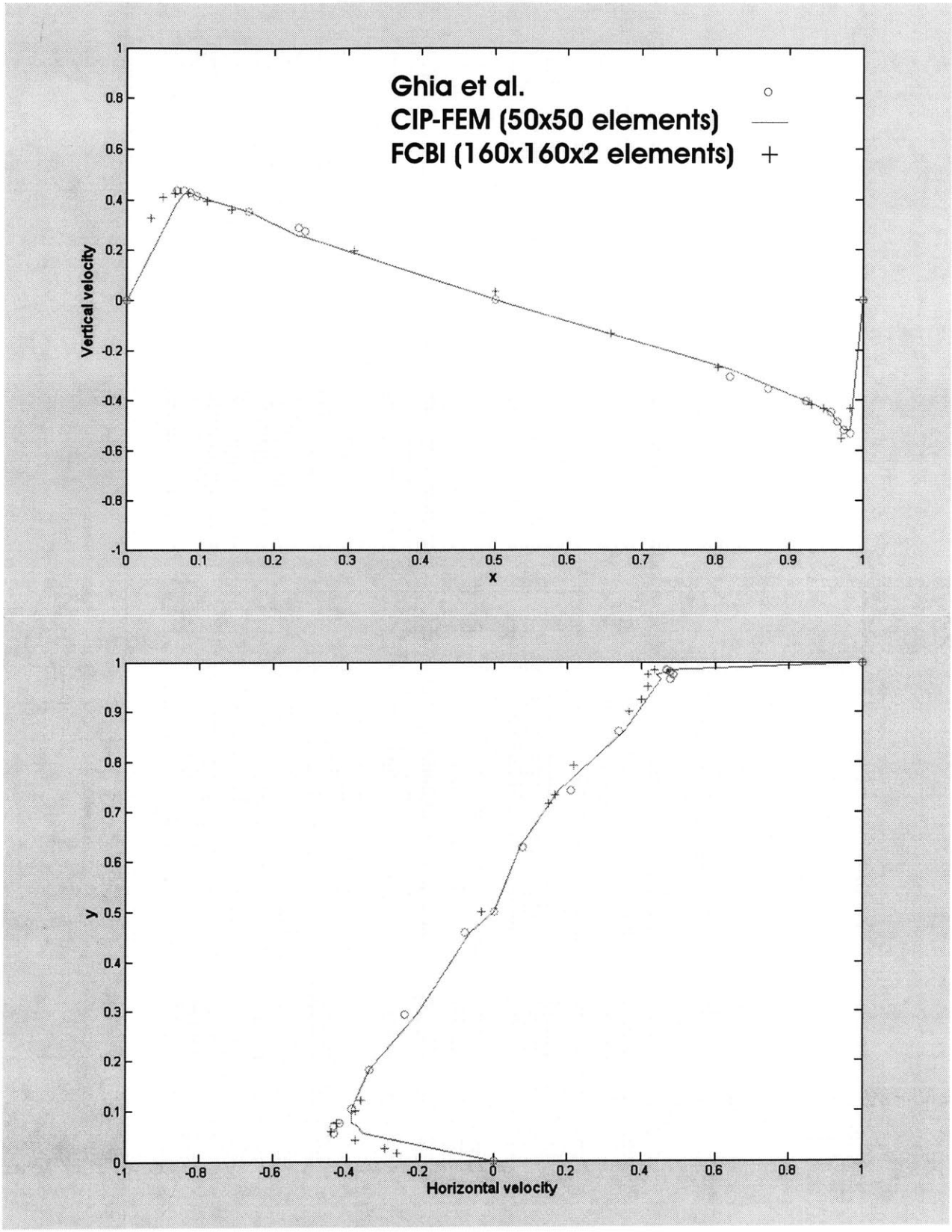

Figure 6-6: Velocity profiles for $Re = 10000$.

6.3 Linking the FCBI scheme to the CIP method

The convergence curves shown in figures (4.18)-(4.19) display a small rate of convergence when the FCBI 9-node element is used. In addition, from figures 6-5 and 6-6 we observe that linking the CIP method to the finite element method improves the accuracy of the solution and velocities are more accurate using the CIP-FEM method. In order to improve the accuracy of the solution and the rate of the convergence for the FCBI scheme, the CIP method is here extended for use in the FCBI scheme.

6.3.1 The governing equations

The non-dimensional continuity and momentum equations are written as,

$$\begin{aligned} &\nabla \cdot \mathbf{u} = 0 \\ &\frac{\partial \mathbf{u}}{\partial t} + (\mathbf{u} \cdot \nabla)\mathbf{u} = -\nabla p + \frac{1}{Re} \nabla^2 \mathbf{u} \end{aligned} \tag{6.55}$$

where $\mathbf{u}$, p and Re are the velocity vector, pressure and the Reynolds number respectively. External force is not considered here.

In the CIP-FCBI method, we need the spatial derivatives of the momentum equation as follows,

$$\begin{aligned} \frac{\partial \mathbf{u}_x}{\partial t} + (\mathbf{u} \cdot \nabla)\mathbf{u}_x &= -(\mathbf{u}_x \cdot \nabla)\mathbf{u} - \nabla p_x + \frac{1}{Re} \nabla^2 \mathbf{u}_x \\ \frac{\partial \mathbf{u}_y}{\partial t} + (\mathbf{u} \cdot \nabla)\mathbf{u}_y &= -(\mathbf{u}_y \cdot \nabla)\mathbf{u} - \nabla p_y + \frac{1}{Re} \nabla^2 \mathbf{u}_y \end{aligned} \tag{6.56}$$

where the subscripts x and y show the derivative in each direction.

We split the governing equations into an advection phase and a non-advection phase. The advection phase is solved by the CIP method and the same third order interpolation functions (6.43)-(6.46) are used. The non-advection phase is solved by the FCBI scheme.

Note that in the FCBI scheme in the equation (4.1), we consider the Navier-

Stokes equations of a two-dimensional incompressible fluid flow at time t when the solution is at the steady-state. In the CIP-FCBI method, we need to include the time dependent terms since the velocities and the spatial derivatives of the velocities for the next time step are obtained by shifting the cubic polynomial in the advection phase and by updating the velocities and its derivatives in the non-advection phase. Here in the CIP-FCBI method, we continue the calculation until the solution is at the steady-state and the velocities, the pressures and the spatial derivatives of the velocities do not change.

- The advection phase

The governing equations of the advection phase are,

$$\begin{aligned} \frac{\hat{\mathbf{u}} - \mathbf{u}^n}{\Delta t} + (\mathbf{u}^n \cdot \nabla)\mathbf{u}^n &= 0 \\ \frac{\hat{\mathbf{u}}_x - \mathbf{u}_x^n}{\Delta t} + (\mathbf{u}^n \cdot \nabla)\mathbf{u}_x^n &= 0 \\ \frac{\hat{\mathbf{u}}_y - \mathbf{u}_y^n}{\Delta t} + (\mathbf{u}^n \cdot \nabla)\mathbf{u}_y^n &= 0 \end{aligned} \tag{6.57}$$

Considering the advection equation for a potential ϕ,

$$\frac{\partial \phi}{\partial t} + \mathbf{u} \cdot \nabla \phi = 0 \tag{6.58}$$

The solution at time "t" is approximated as,

$$\phi(x_i, t) \sim \phi\left(x_i - \int u dt, t - dt\right) \tag{6.59}$$

where x_i denotes the grid point where ϕ is given. The start point $x_* = x_i - \int u dt$ becomes the grid point at the next time step. x_* is called the advection distance and should be calculated along the particle path. However, the exact value of this distance is difficult to obtain and it is approximated explicitly as,

$$\Delta x = x_i - x_* = u_i^n \, \Delta t \tag{6.60}$$

In order for this approximation to be close to the exact value, Δt must be sufficiently small.

In the CIP method, the potential ϕ is interpolated using the third order shape functions, and these functions are defined for the system of coordinates ξ-η within each sub-element. Since the start point x_* is obtained in the x-y coordinate system, we find the corresponding ξ_* and η_* for this point.

The shape function then is defined as,

$$\phi(\xi,\eta) = \sum_a h_a(\xi,\eta)[G_a(\xi,\eta) + E_a(\xi,\eta)\phi_a] \tag{6.61}$$

where h_a is the conventional linear shape function, and G_a and E_a are new shape functions that are second order and linear respectively.

We use the FCBI 9-node elements consist of four 4-node sub-elements shown in figure 6-7(a) to descretize the fluid domain. For the sub-element shown in figure 6-7(b), these functions are as follows,

$$\begin{aligned} h_1 &= \frac{1}{4}(1-\xi)(1-\eta) \\ h_2 &= \frac{1}{4}(1+\xi)(1-\eta) \\ h_3 &= \frac{1}{4}(1+\xi)(1+\eta) \\ h_4 &= \frac{1}{4}(1-\xi)(1+\eta) \end{aligned} \tag{6.62}$$

$$\begin{aligned} E_1 &= \frac{1}{2}(-\xi-\eta) \\ E_2 &= \frac{1}{2}(\xi-\eta) \\ E_3 &= \frac{1}{2}(\xi+\eta) \\ E_4 &= \frac{1}{2}(-\xi+\eta) \end{aligned} \tag{6.63}$$

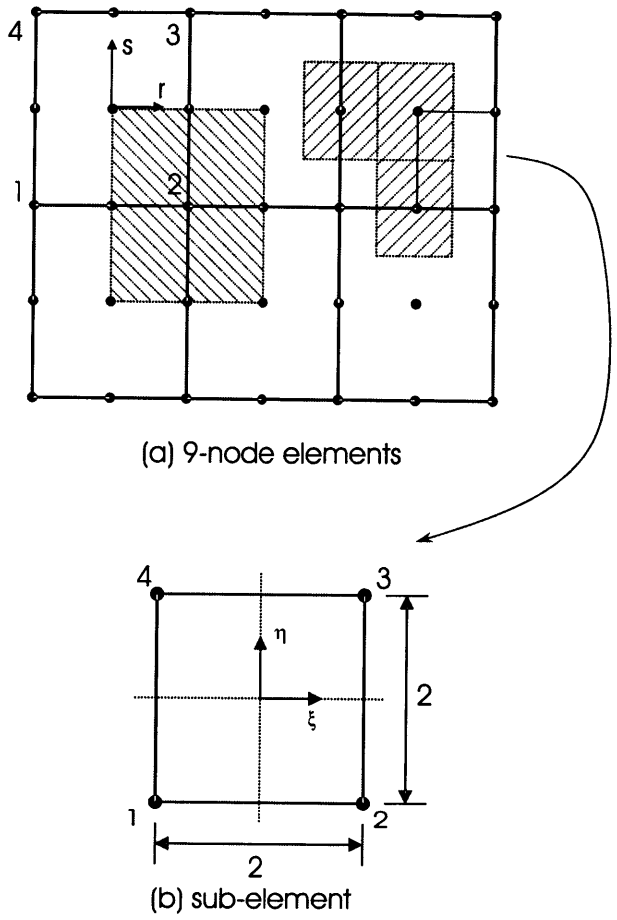

Figure 6-7: 9-node elements and the 4-node sub-element used in the finite element discretization

$$
\begin{aligned}
G_1 &= \frac{1}{2}(1-\xi^2)[\partial_\xi\phi_1 + \phi_1] + \frac{1}{2}(1-\eta^2)[\partial_\eta\phi_1 + \phi_1] \\
G_2 &= \frac{1}{2}(-1+\xi^2)[\partial_\xi\phi_2 - \phi_2] + \frac{1}{2}(1-\eta^2)[\partial_\eta\phi_2 + \phi_2] \\
G_3 &= \frac{1}{2}(-1+\xi^2)[\partial_\xi\phi_3 - \phi_3] + \frac{1}{2}(-1+\eta^2)[\partial_\eta\phi_3 - \phi_3] \\
G_4 &= \frac{1}{2}(1-\xi^2)[\partial_\xi\phi_4 + \phi_4] + \frac{1}{2}(-1+\eta^2)[\partial_\eta\phi_4 - \phi_4]
\end{aligned}
\tag{6.64}
$$

Using the CIP-FCBI method, the velocity $\mathbf{u}$ and its derivatives are updated for the time "t" ($\hat{\mathbf{u}}$, $\hat{\mathbf{u}}_x$ and $\hat{\mathbf{u}}_y$). These values are then taken to the non-advection phase.

- The non-advection phase

The governing equations are as follows,

$$\begin{aligned}
\frac{\mathbf{u}^{n+1}-\hat{\mathbf{u}}}{\Delta t} + \nabla p^{n+1} &= \frac{1}{Re}\,\nabla^2\mathbf{u}^n \\
\frac{\mathbf{u}_x^{n+1}-\hat{\mathbf{u}}_x}{\Delta t} &= -(\mathbf{u}_x^n\cdot\nabla)\mathbf{u}^n - \nabla p_x^{n+1} + \frac{1}{Re}\,\nabla^2\mathbf{u}_x^n \\
\frac{\mathbf{u}_y^{n+1}-\hat{\mathbf{u}}_y}{\Delta t} &= -(\mathbf{u}_y^n\cdot\nabla)\mathbf{u}^n - \nabla p_y^{n+1} + \frac{1}{Re}\,\nabla^2\mathbf{u}_y^n
\end{aligned} \tag{6.65}$$

In order to avoid considering the pressure derivatives p_x and p_y as nodal variables and updating them for each time step in the second and third equations, these terms are replaced by the velocity terms from the first equation. Then, the second and third equations are written as,

$$\begin{aligned}
\frac{\mathbf{u}_x^{n+1}-\hat{\mathbf{u}}_x}{\Delta t} &= -(\mathbf{u}_x^n\cdot\nabla)\mathbf{u}^n + \frac{\partial}{\partial x}\left(\frac{\mathbf{u}^{n+1}-\hat{\mathbf{u}}}{\Delta t}\right) \\
\frac{\mathbf{u}_y^{n+1}-\hat{\mathbf{u}}_y}{\Delta t} &= -(\mathbf{u}_y^n\cdot\nabla)\mathbf{u}^n + \frac{\partial}{\partial y}\left(\frac{\mathbf{u}^{n+1}-\hat{\mathbf{u}}}{\Delta t}\right)
\end{aligned} \tag{6.66}$$

The non-advection phase is discretized by the FCBI scheme. The finite element solution is obtained by considering a weak form of these equations and the continuity equation. Using the Petrov-Galerkin procedure (the test functions do not correspond to the trial functions), the weak formulation of the problem within the domain Ω can be given as

Find $\mathbf{u}\in U$ and $p\in P$ such that

$$\begin{aligned}
&\int_\Omega w\left(\frac{\mathbf{u}^{n+1}-\hat{\mathbf{u}}}{\Delta t} + \nabla p^{n+1}\right)\,d\Omega = \int_\Omega w\,\frac{1}{Re}\,\nabla^2\mathbf{u}^n\,d\Omega \\
&\int_\Omega q\,\nabla\cdot\mathbf{u}\,d\Omega = 0 \\
&\int_\Omega w\left(\frac{\mathbf{u}_x^{n+1}-\hat{\mathbf{u}}_x}{\Delta t}\right)\,d\Omega = \int_\Omega w\,\left[-(\mathbf{u}_x^n\cdot\nabla)\mathbf{u}^n + \frac{\partial}{\partial x}\left(\frac{\mathbf{u}^{n+1}-\hat{\mathbf{u}}}{\Delta t}\right)\right]\,d\Omega \\
&\int_\Omega w\left(\frac{\mathbf{u}_y^{n+1}-\hat{\mathbf{u}}_y}{\Delta t}\right)\,d\Omega = \int_\Omega w\,\left[-(\mathbf{u}_y^n\cdot\nabla)\mathbf{u}^n + \frac{\partial}{\partial y}\left(\frac{\mathbf{u}^{n+1}-\hat{\mathbf{u}}}{\Delta t}\right)\right]\,d\Omega
\end{aligned} \tag{6.67}$$

where $w \in W$ and $q \in Q$.

For the 4-node sub-element shown in figure 6-7, we use the four corner points to interpolate the velocity when the pressure is interpolated within each element. The trial functions in U are defined in each sub-element as,

$$\begin{aligned} h_1^u &= \frac{1}{4}(1-\xi)(1-\eta) \\ h_2^u &= \frac{1}{4}(1+\xi)(1-\eta) \\ h_3^u &= \frac{1}{4}(1+\xi)(1+\eta) \\ h_4^u &= \frac{1}{4}(1-\xi)(1+\eta) \end{aligned} \tag{6.68}$$

with $-1 \leq \xi, \eta \leq 1$.

Similarly, the trial functions in the space P are given in each element as,

$$\begin{aligned} h_1^p &= \frac{1}{4}(1-r)(1-s) \\ h_2^p &= \frac{1}{4}(1+r)(1-s) \\ h_3^p &= \frac{1}{4}(1+r)(1+s) \\ h_4^p &= \frac{1}{4}(1-r)(1+s) \end{aligned} \tag{6.69}$$

with $-1 \leq r, s \leq 1$.

The elements in the space Q are step functions. Referring to Fig. 4.2(a), we have, at node 2, for example,

$$h_2^q = \begin{cases} 1 & \text{for } (r,s) \in [0,1] \times [-1,0] \\ 0 & \text{elsewhere} \end{cases} \tag{6.70}$$

Similarly, the weight functions in the space W are also step functions. Considering the sub-element shown in Fig. 4.2(b), at node 1, for example,

$$h_2^w = \begin{cases} 1 & \text{for } (\xi,\eta) \in [-1,0] \times [-1,0] \\ 0 & \text{elsewhere} \end{cases} \tag{6.71}$$

Then the velocity $\mathbf{u}$ and its derivatives and the pressure p in (6.67) are replaced by

$$\begin{aligned} \mathbf{u} &= \sum_{i=1}^{4} h_i^u \ \mathbf{u}_i \\ \mathbf{u}_x &= \sum_{i=1}^{4} h_{xi}^u \ \mathbf{u}_i \\ \mathbf{u}_y &= \sum_{i=1}^{4} h_{yi}^u \ \mathbf{u}_i \\ p &= \sum_{j=1}^{4} h_j^p \ p_j \end{aligned} \tag{6.72}$$

The dimensional form of the equations (6.67) is written as

$$\begin{aligned} &\int_\Omega w \left(\frac{\mathbf{u}^{n+1} - \hat{\mathbf{u}}}{\Delta t} + \frac{1}{\rho} \nabla p^{n+1} \right) d\Omega = \int_\Omega w \ \frac{\mu}{\rho} \nabla^2 \mathbf{u}^n \ d\Omega \\ &\int_\Omega q \ \nabla \cdot (\rho \mathbf{u}) \ d\Omega = 0 \\ &\int_\Omega w \left(\frac{\mathbf{u}_x^{n+1} - \hat{\mathbf{u}}_x}{\Delta t} \right) d\Omega = \int_\Omega w \left[-(\mathbf{u}_x^n \cdot \nabla)\mathbf{u}^n + \frac{\partial}{\partial x} \left(\frac{\mathbf{u}^{n+1} - \hat{\mathbf{u}}}{\Delta t} \right) \right] d\Omega \\ &\int_\Omega w \left(\frac{\mathbf{u}_y^{n+1} - \hat{\mathbf{u}}_y}{\Delta t} \right) d\Omega = \int_\Omega w \left[-(\mathbf{u}_y^n \cdot \nabla)\mathbf{u}^n + \frac{\partial}{\partial y} \left(\frac{\mathbf{u}^{n+1} - \hat{\mathbf{u}}}{\Delta t} \right) \right] d\Omega \end{aligned} \tag{6.73}$$

Assembling the first two equations in (6.73) (the momentum and the continuity equations) for all the control volumes in the body, and using the divergence theorem we get

$$\begin{pmatrix} \mathbf{K}_{\mathbf{v}_x\mathbf{v}_x} & \mathbf{K}_{\mathbf{v}_x\mathbf{v}_y} & \mathbf{K}_{\mathbf{v}_x\mathbf{p}} \\ \mathbf{K}_{\mathbf{v}_y\mathbf{v}_x} & \mathbf{K}_{\mathbf{v}_y\mathbf{v}_y} & \mathbf{K}_{\mathbf{v}_y\mathbf{p}} \\ \mathbf{K}_{\mathbf{p}\mathbf{v}_x} & \mathbf{K}_{\mathbf{p}\mathbf{v}_y} & \mathbf{0} \end{pmatrix} \begin{pmatrix} \mathbf{u}^1 \\ \mathbf{u}^2 \\ \mathbf{p} \end{pmatrix} = \begin{pmatrix} \mathbf{R}_{\mathbf{v}_x} \\ \mathbf{R}_{\mathbf{v}_y} \\ \mathbf{0} \end{pmatrix} \tag{6.74}$$

where $\mathbf{u}^1$ and $\mathbf{u}^2$ contain the nodal velocities in the x and y directions respectively and $\mathbf{p}$ contains the nodal pressures. For a mesh of non-distorted elements, we get

$$\begin{aligned}
\mathbf{K}_{\mathbf{v}_x\mathbf{v}_x}(i,j) &= \frac{1}{\Delta t} \sum_i w_{\Omega i} \int_\Omega h_j^u \, dxdy \\
\mathbf{K}_{\mathbf{v}_x\mathbf{v}_y}(i,j) &= 0 \\
\mathbf{K}_{\mathbf{v}_x\mathbf{p}}(i,j) &= \sum_i w_{\Omega i} \int_{\partial\Omega} \frac{h_j^p}{\rho} \, n_x \, dy \\
\mathbf{K}_{\mathbf{v}_y\mathbf{v}_x}(i,j) &= 0 \\
\mathbf{K}_{\mathbf{v}_y\mathbf{v}_y}(i,j) &= \mathbf{K}_{\mathbf{v}_x\mathbf{v}_x}(i,j) \\
\mathbf{K}_{\mathbf{v}_y\mathbf{p}}(i,j) &= \sum_i w_{\Omega i} \int_{\partial\Omega} \frac{h_j^p}{\rho} \, n_y \, dx \\
\mathbf{K}_{\mathbf{p}\mathbf{v}_x}(i,j) &= \sum_i q_{\Omega i} \int_{\partial\Omega} h_j^u \, n_x \, dy \\
\mathbf{K}_{\mathbf{p}\mathbf{v}_y}(i,j) &= \sum_i q_{\Omega i} \int_{\partial\Omega} h_j^u \, n_y \, dx
\end{aligned} \tag{6.75}$$

$$\begin{aligned}
\mathbf{R}_{\mathbf{v}_x}(i) &= \sum_i w_{\Omega i} \int_{\partial\Omega} \frac{\mu}{\rho} \, (h_{j,y}^u \, u_j^{1n}) \, n_y \, dx + \sum_i w_{\Omega i} \int_{\partial\Omega} \frac{\mu}{\rho} \, (h_{j,x}^u \, u_j^{1n}) \, n_x \, dy \\
&\quad + \frac{1}{\Delta t} \sum_i w_{\Omega i} \int_\Omega h_j^u \, dxdy \, \hat{u}_j^1 \\
\mathbf{R}_{\mathbf{v}_y}(i) &= \sum_i w_{\Omega i} \int_{\partial\Omega} \frac{\mu}{\rho} \, (h_{j,y}^u \, u_j^{2n}) \, n_y \, dx + \sum_i w_{\Omega i} \int_{\partial\Omega} \frac{\mu}{\rho} \, (h_{j,x}^u \, u_j^{2n}) \, n_x \, dy \\
&\quad + \frac{1}{\Delta t} \sum_i w_{\Omega i} \int_\Omega h_j^u \, dxdy \, \hat{u}_j^2
\end{aligned} \tag{6.76}$$

where u_j^1 and u_j^2 are the velocities in x and y directions respectively ($\mathbf{u}_j = [u_j^1, u_j^2]^T$), $\partial\Omega$ is the surface area of the control volume Ω and n_x and n_y are the elements of the unit normal vector $\mathbf{n}$ pointing to the outside of the control volume.

As it was mentioned earlier in chapter 4, for the FCBI 9-node element used here, the *inf-sup* condition is satisfied. Note that the equation (6.74) is linear and there is no iteration involved to solve this equation. In addition, elements of the $\mathbf{K}$ matrix can be calculated once at the beginning of the solution and at each time step, only the load vector $\mathbf{R}$ needs to be updated. This will decrease the solution time significantly.

Assembling the last two equations in (6.73) (the spatial derivatives of the momentum equation) for all the control volumes in the body, we get

$$\begin{aligned} M_{ij}\left(\frac{\mathbf{u}_x^{n+1} - \hat{\mathbf{u}}_x}{\Delta t}\right)_j &= \mathbf{R}_{ix} \\ M_{ij}\left(\frac{\mathbf{u}_y^{n+1} - \hat{\mathbf{u}}_y}{\Delta t}\right)_j &= \mathbf{R}_{iy} \end{aligned} \tag{6.77}$$

where the matrices M_{ij}, $\mathbf{R}_{ix}$ and $\mathbf{R}_{iy}$ are written as,

$$\begin{aligned} M_{ij} &= \sum_i w_{\Omega i} \int_\Omega h_j^u \, dxdy \\ \mathbf{R}_{ix} &= \sum_i w_{\Omega i} \left(\int_\Omega h_{j,x}^u \, dxdy\right)\left(\frac{\mathbf{u}^{n+1} - \hat{\mathbf{u}}}{\Delta t}\right)_j - \sum_i w_{\Omega i} \int_\Omega (h_j^u \, u_{jx}^{1n})\,(h_{j,x}^u \, \mathbf{u}_j^n)\, dxdy \\ &\quad - \sum_i w_{\Omega i} \int_\Omega (h_j^u \, u_{jx}^{2n})\,(h_{j,y}^u \, \mathbf{u}_j^n)\, dxdy \\ \mathbf{R}_{iy} &= \sum_i w_{\Omega i} \left(\int_\Omega h_{j,y}^u \, dxdy\right)\left(\frac{\mathbf{u}^{n+1} - \hat{\mathbf{u}}}{\Delta t}\right)_j - \sum_i w_{\Omega i} \int_\Omega (h_j^u \, u_{jy}^{1n})\,(h_{j,x}^u \, \mathbf{u}_j^n)\, dxdy \\ &\quad - \sum_i w_{\Omega i} \int_\Omega (h_j^u \, u_{jy}^{2n})\,(h_{j,y}^u \, \mathbf{u}_j^n)\, dxdy \end{aligned} \tag{6.78}$$

where the subscripts x and y show the derivative in x and y directions, the superscript n stands for the number of the time step and superscripts 1 and 2 denote the velocity

in x and y directions respectively. For a non-distorted mesh, the M_{ij} matrix is the same for all the elements and therefore the assemblage will be easy.

In the non-advection phase, first the velocity $\mathbf{u}^{n+1}$ and the pressure p^{n+1} are obtained from the equation (6.74), the velocity $\mathbf{u}^{n+1}$ is then used in (6.77) to obtain $\mathbf{u}_x^{n+1}$ and $\mathbf{u}_y^{n+1}$. The calculations for one time step are complete now and for the next time step, we take the values $\mathbf{u}^{n+1}$, p^{n+1}, $\mathbf{u}_x^{n+1}$ and $\mathbf{u}_y^{n+1}$ to the advection phase and we repeat the calculations for the new time step.

The solution process is given in table 6.3.1.

Table 6.3.1 Solution process in the CIP-FCBI method for incompressible flows

(1) Set initial conditions $\mathbf{u}^n$ and the spatial derivatives $\mathbf{u}_x^n$ and $\mathbf{u}_y^n$ for all the nodal points (the superscript n denotes the solution at time $t - \Delta t$).

(2) From the advection phase use the CIP solver to obtain $\hat{\mathbf{u}}$ and the spatial derivatives $\hat{\mathbf{u}}_x$ and $\hat{\mathbf{u}}_y$ for all the nodal points using equations (6.61)- (6.64).

(3) From the non-advection phase, use the FCBI scheme to obtain $\mathbf{u}^{n+1}$ and p^{n+1} from the equation (6.74).

(4) From the non-advection phase, obtain the spatial derivatives $\mathbf{u}_x^{n+1}$ and $\mathbf{u}_y^{n+1}$ from the equation (6.77).

(5) Repeat (2) to (5) for the next time step.

6.3.2 Numerical solutions

To study the effectiveness of the CIP-FCBI method, we again consider the driven cavity flow problem shown in figure 6-3. The boundary conditions are shown in this figure and the initial conditions are all zero except for the horizontal velocity $u = 1$ at the upper side of the cavity. This problem is solved for two different cases; $Re = 1000$ and $Re = 10000$. In both cases, the horizontal velocity at the vertical centerline, and the vertical velocity at the horizontal centerline are plotted and compared with the solutions of the *Ghia et al.*, the CIP-FEM method and the FCBI method.

- For $Re = 1000$

In this problem, a non-uniform mesh of 32 x 32 sub-elements (16 x 16 elements) (figure 6-8 (a)) has been used. For the time increment $\Delta t = 0.005$, the flow is almost steady at $t = 35$. The velocity profiles on the vertical and horizontal center axes of the cavity are shown in figure 6-9 at time $t = 35$. In this figure, the solution obtained by *Ghia et al.* is shown by "o", this solution is assumed to be the exact solution. The solution obtained for the FCBI triangular elements for a mesh of 40 x 40 x 2 elements [20], and the solution obtained for the CIP-FEM method for a mesh of 30 x 30 elements (figure 6-4 (a)) are also given in this figure.

As it is clear from figure 6-9, the CIP-FCBI method has a higher spatial accuracy than the FCBI scheme. In addition, the spatial derivatives are more accurate in the CIP-FCBI method since they are considered as nodal variables in the solution. However, this method requires more computational effort than the FCBI method. For example, in the CIP-FCBI method, the problem is solved in two phases; the advection phase and the non-advection phase and in each phase after the nodal velocities have been updated, the nodal spatial derivatives are calculated. The velocities are slightly more accurate using the CIP-FEM method. However, the CIP-FEM method requires more computational effort than the CIP-FCBI method since for the non-advection phase, the continuity equation is satisfied by the relaxation method and this increases the solution time.

It should be noted that although spatial derivatives of velocities are also considered as nodal variables in the CIP-FCBI method, the system of equations for velocities are solved separately from the system of equations for velocity derivatives (after velocities are obtained, then the velocity derivatives are updated).

- For $Re = 10000$

The non-uniform mesh of 64 x 64 sub-elements (32 x 32 elements) shown in figure 6-8 (b) with the time increment $\Delta t = 0.002$ has been used here. After the solution is steady, the velocity profiles on the vertical and horizontal center axes of the cavity are as shown in figure 6-10. In this figure, the *Ghia et al.*, the CIP-FEM, and the FCBI solutions are also given. It can be seen that the CIP-FCBI method has higher

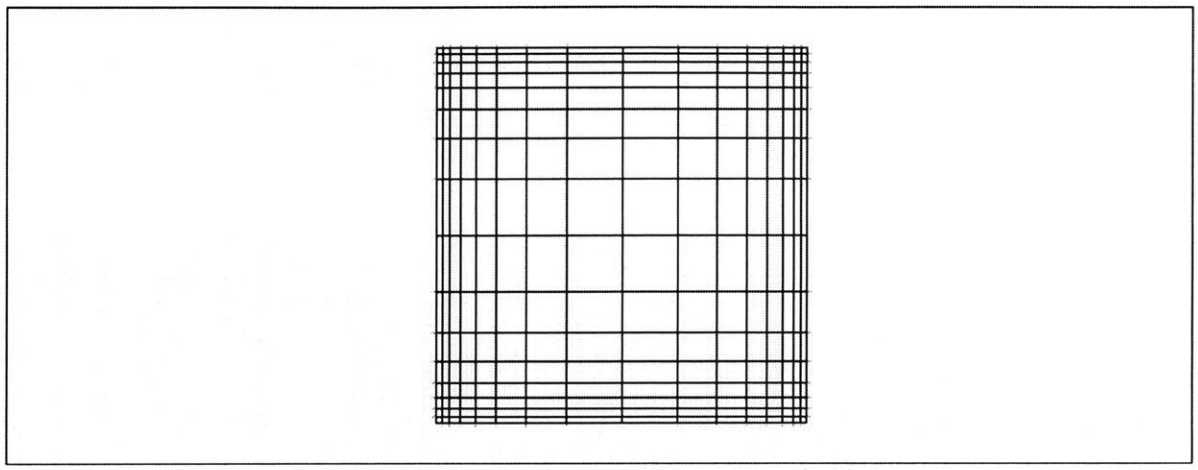

(a) 16 x 16 elements (32 x 32 sub-elements)

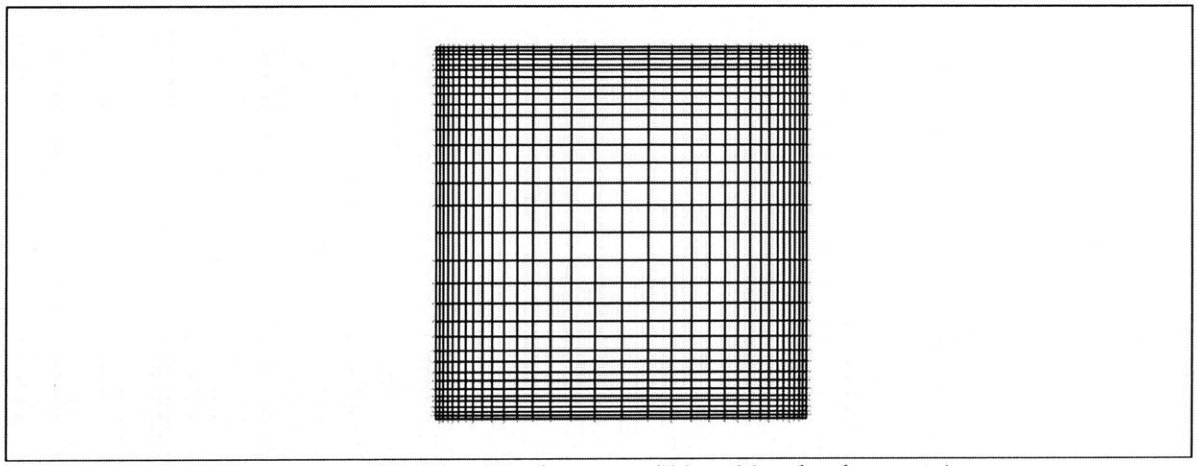

(b) 32 x 32 elements (64 x 64 sub-elements)

Figure 6-8: The non-uniform meshes used for (a) $Re = 1000$, (b) $Re = 10000$.

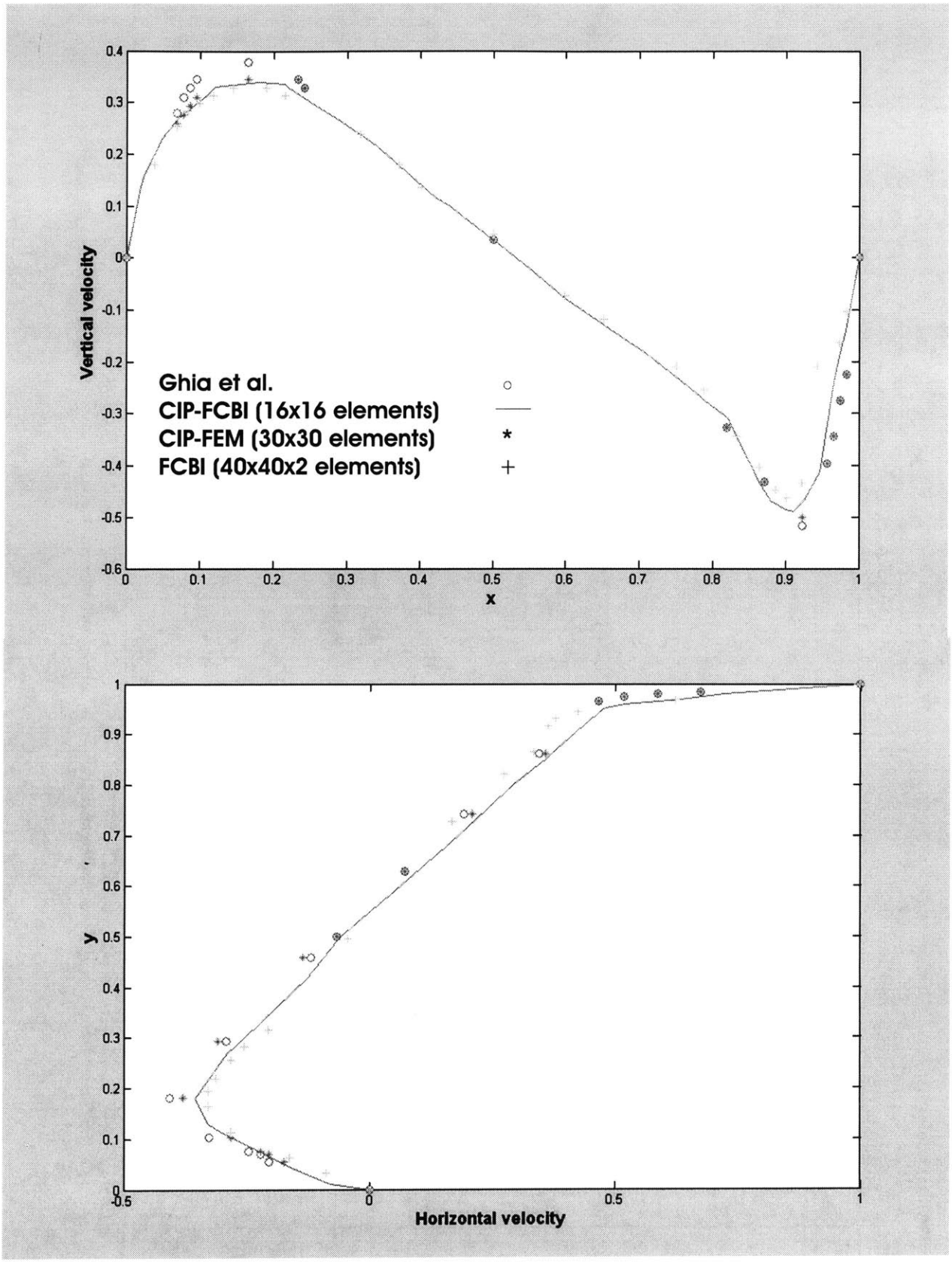

Figure 6-9: Velocity profiles for $Re = 1000$.

spatial accuracy than the FCBI scheme (the FCBI triangular element has been used here [20]). However, the velocities are slightly more accurate using the CIP-FEM method.

- Concluding remarks on the numerical results

Of course we can only draw partial conclusions from these preliminary numerical results since, in particular, other fluid problems need to be solved for comprehensiveness.

From these numerical results, the CIP-FEM and the CIP-FCBI methods appear to predict the solution more accurately than the traditional finite element method and the FCBI scheme. In order to solve high Reynolds number flows with the traditional finite element method, we require a very fine mesh. Linking the CIP method to the finite element method increases the stability of the solution in addition to improving the accuracy for the velocities and the spatial derivatives. In order to obtain accurate solutions for high Reynolds number flows, we require a finer mesh for the FCBI method than for the CIP-FCBI method. Linking the CIP method to the FCBI scheme improves the accuracy for the velocities and the derivatives. In addition, when the flow is not at the steady state and the time dependent terms need to be included in the Navier-Stokes equations, or in the problems when the derivatives of the velocities need to be obtained to high accuracy, the CIP-FCBI method is more convenient than the FCBI method. However, both the CIP-FEM method and the CIP-FCBI methods require more computational effort than the finite element method and the FCBI scheme (and it takes longer for these methods to stabilize the flow) since the advection phase is solved by the CIP method. In addition, in the CIP-FEM method, the continuity equation is satisfied by the relaxation method and this increases the solution time.

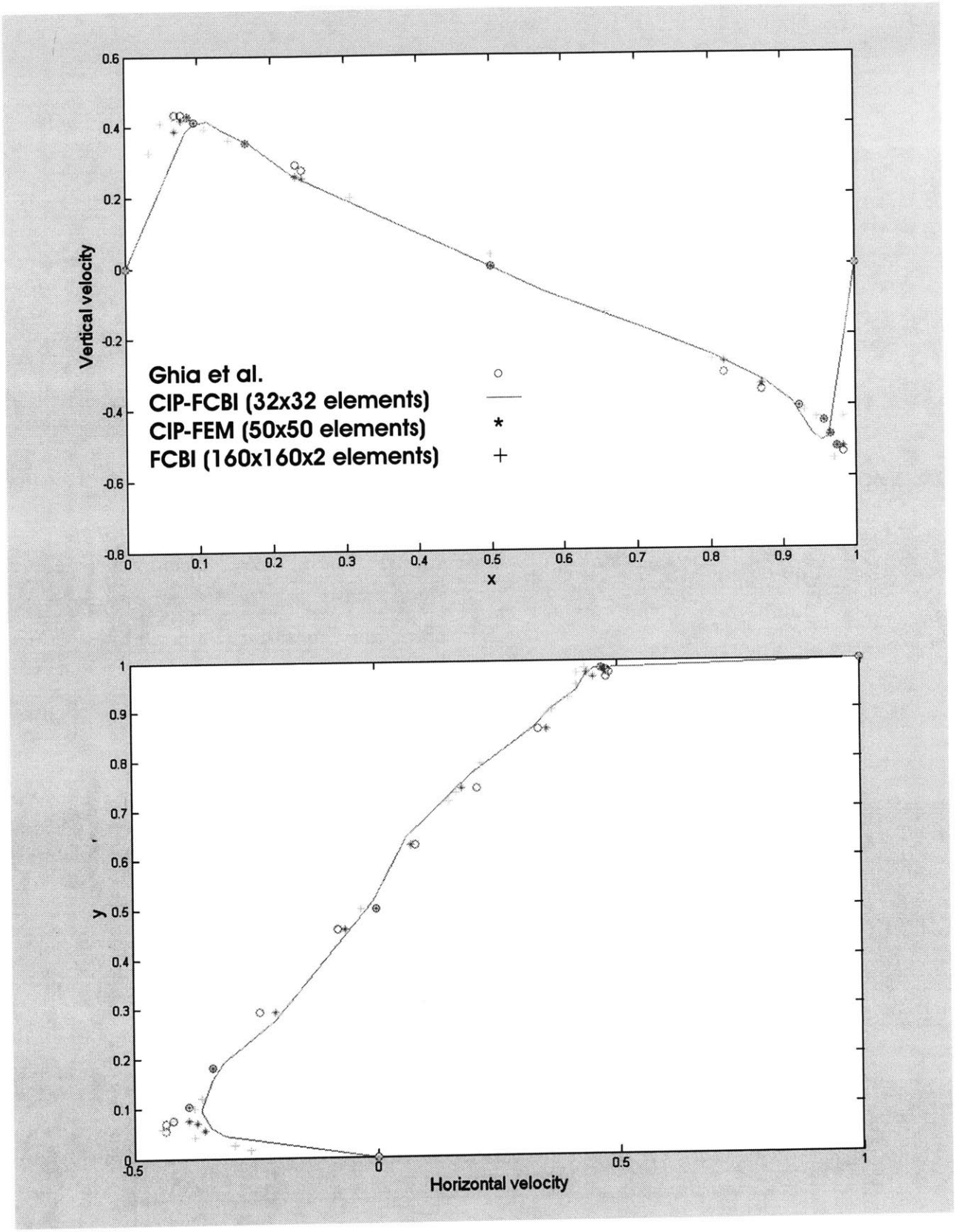

Figure 6-10: Velocity profiles for $Re = 10000$.

Chapter 7

Conclusions

The Navier-Stokes equations are widely used for the analysis of incompressible laminar flows. If the Reynolds number is increased to certain values, oscillations appear in the finite element solution of the Navier-Stokes equations. In order to solve for high Reynolds number flows and avoid the oscillations, one technique is to introduce artificial upwinding into the equations to stabilize the convective term, ideally without degrading the accuracy of the solution: e.g. the streamline upwind/Petrov-Galerkin (SUPG) method , the Galerkin/least-squares (GLS) method, the Cubic Interpolated Pseudo/Propagation (CIP) method and use of the bubble functions.

The analysis of fluid flows with structural interactions has captured much attention during the recent years. Such analysis is performed considering the solution of the Navier-Stokes fluid flows fully coupled to the non-linear structural response. However, a fully coupled fluid flow structural interaction analysis can be computationally very expensive. The cost of the solution is, roughly, proportional to the number of nodes or grid points used to discretize the fluid and the structure. In order for interaction effects to be significant, the structure is usually thin and can be represented as a shell, hence not too many grid points are required. The large number of grid points and consequently number of equations in fluid flow structural interaction problems (FSI) is due to the representation of the fluid domain. For high Reynolds number fluid flows, to have a stable solution, more grid points are required. In order to decrease the number of grid points in the fluids (using a coarser mesh) and still have a stable

solution, the flow-condition-based interpolation (FCBI) procedure was introduced.

The FCBI is a hybrid of the finite element and the finite volume methods and introduces some upwinding into the laminar Navier-Stokes equations by using the exact solution of the advection-diffusion equation in the trial functions in the advection term. The test functions for both the continuity and the momentum equations are step functions and the governing equations are written over control volumes. Hence, the mass and momentum conservations are satisfied locally. Ideally any numerical solution for fluids should yield stable solutions for low and high Reynolds number flows with reasonable accuracy. Of course, when fine meshes are used, more details of the flow are captured and the level of accuracy is higher. Ideally, we want our numerical scheme to yield still stable solutions with reasonable accuracy when coarse meshes are used. In particular, this will decrease the required number of grid points and elements in the fluid phase in the fluid-structure interaction problems.

The previous works on the FCBI procedure include the development of a 4-node element and a 9-node element consisting of four 4-node sub-elements. In this thesis, the stability, the accuracy and the rate of convergence of the already published FCBI schemes was studied. From the numerical results, the FCBI 9-node elements (consist of four 4-node sub-elements) appear to be stable for high Reynolds numbers although no upwind parameter is used, and predict the solution reasonably accurate. Of course, in order for the solution errors to be small, the mesh needs to be refined. However, the convergence curves used for the $\| \mathbf{u} - \mathbf{u}_h \|_{L^2}$, $\| \mathbf{u} - \mathbf{u}_h \|_{H^1}$ and $\| p - p_h \|_{L^2}$ norms, display a small rate of convergence when the FCBI 9-node elements are used.

In order to ensure that using the coarse meshes to represent the fluid yields an accurate enough structural response, the solution errors need to be controlled and measured. The "goal-oriented error estimation" might be applied to assess the error in the quantities of interest in the structure. In fluid flow structural interaction analysis, it is ideal to use an FCBI solution scheme in rather coarse meshes together with "goal-oriented error estimation" to control the error of the solution in the structural response.

From the numerical results, it became clear that the earlier published FCBI 9-

node elements (consist of four 4-node sub-elements) are more stable than the Galerkin 9-node elements. However, the Galerkin 9-node elements give more accurate solutions with a higher rate of convergence. Hence, a new FCBI 9-node element was proposed that obtains more accurate solutions than the earlier proposed FCBI elements. The new 9-node element does not obtain the solution as accurate as the Galerkin 9-node elements but the solution is stable for much higher Reynolds numbers (than the Galerkin 9-node elements), and accurate enough to be used to find the structural responses.

The Cubic-Interpolated Pseudo-particle (CIP) method is a very stable finite difference technique that can solve generalized hyperbolic equations by the 3rd order of accuracy in space. In this method, a cubic polynomial is used to interpolate the spatial profile of the value and its spatial derivative. The spatial derivative itself is a free parameter and satisfies the master equation for the derivative. After the value and its spatial derivative are found, the same values for the next time step are simply calculated by shifting the cubic polynomial. For nonlinear problems, the CIP scheme splits the hyperbolic equation into two phases; the non-advection phase and the advection phase. In each time step, after the non-advection phase is solved by the finite difference method, the CIP method is applied to the advection phase.

The CIP method was originally proposed for the finite difference method; both the convection phase and the non-convection phase are solved using the finite difference method. However in some problems, satisfying the boundary conditions for the incompressible Navier-Stokes equations is easier using the finite element methods. In addition, in problems for which the domain is complicated and mesh grading is required, the finite difference methods are not as flexible as the finite element methods.

In this thesis, the CIP method was extended for use in the finite element method (CIP-FEM) and the FCBI scheme (CIP-FCBI). The finite element shape functions for the third order interpolation were defined by the product of the linear shape function and a new second order shape function. These functions were used to solve the two-dimensional incompressible Navier-Stokes equations.

From the numerical results, the CIP-FEM and the CIP-FCBI methods appear to

predict the solution more accurate than the traditional finite element method and the FCBI scheme. In order to solve high Reynolds number flows with the traditional finite element method, we require a very fine mesh. Linking the CIP method to the finite element method increases the stability of the solution in addition to improving the accuracy for the velocities and the derivatives. In order to obtain accurate solutions for high Reynolds number flows, we require a finer mesh for the FCBI method than for the CIP-FCBI method. Linking the CIP method to the FCBI scheme improves the accuracy for the velocities and the derivatives. In addition, when the flow is not at the steady state and the time dependent terms need to be included in the Navier-Stokes equations, or in the problems when the derivatives of the velocities need to be obtained to high accuracy, the CIP-FCBI method is more convenient than the FCBI method. However, both the CIP-FEM method and the CIP-FCBI methods require more computational effort than the finite element method and the FCBI scheme (and it takes longer for these methods to stabilize the flow) since the advection phase is solved by the CIP method. In addition, in the CIP-FEM method, the continuity equation is satisfied by the relaxation method and this increases the solution time.

This work represents only a first step in liking the FCBI scheme to the CIP method, more work could be done to improve the accuracy of the solution in the CIP-FCBI method. In addition, to study the accuracy and convergence of the FCBI 9-node elements, we considered the L^2 and H^1 norms of the velocities and L^2 norm of the pressure, better norms could be found to measure the errors in the FCBI scheme.

Appendix A

Consistency of the CIP scheme

The difference scheme $\hat{\mathcal{L}}f^n = 0$ is consistent with the differential equation $\mathcal{L}f = 0$ if for all grid points j and time steps n

$$(\hat{\mathcal{L}}f^n)_j - (\mathcal{L}f)_j^n \to 0 \tag{A.1}$$

when $\Delta x, \Delta t \to 0$.

In this appendix, we prove the consistency of the CIP scheme for the one-dimensional non-linear hyperbolic equation

$$\frac{\partial f}{\partial t} + u\frac{\partial f}{\partial x} = G = g - f\frac{\partial u}{\partial x} \tag{A.2}$$

As it was explained in chapter 6, f' should satisfy the spatial derivative of the master equation (A.2) as

$$\frac{\partial f'}{\partial t} + u\frac{\partial f'}{\partial x} = G' - f'\frac{\partial u}{\partial x} \tag{A.3}$$

In order to solve (A.2) and (A.3), the CIP scheme splits the problem into two phases; the non-advection phase and the advection phase. The non-advection phase is solved by a finite difference scheme while the advection phase is solved by the CIP solver.

- Non-advection phase

The equations to be solved are,

$$\begin{aligned}\left(\frac{\partial f}{\partial t}\right)_{(1)} &= G = g - f\frac{\partial u}{\partial x} \\ \left(\frac{\partial f'}{\partial t}\right)_{(1)} &= G' - f'\frac{\partial u}{\partial x}\end{aligned} \tag{A.4}$$

The first equation is simply solved using finite differencing

$$f_i^* = f_i^n + G_i^n \Delta t \tag{A.5}$$

where the superscript (*) stands for the time after one step in the non-advection phase.

The second equation in (A.4) can be solved again by finite differencing the equation or by finding f' in terms of G' from equation (A.5). Thus we have,

$$\frac{(f_i'^* - f_i'^n)}{\Delta t} = \frac{(f_{i+1}^* - f_{i-1}^* - f_{i+1}^n + f_{i-1}^n)}{2\Delta x \Delta t} - f_i'^n \frac{(u_{i+1}^n - u_{i-1}^n)}{2\Delta x} \tag{A.6}$$

Note that we need to prove the consistency of the finite difference scheme used here. Considering the first equation in (A.4), the differential equation and the finite difference scheme used are as follows (at the grid point j)

$$\begin{aligned}(\hat{\mathcal{L}} f^n)_j &= \frac{f_j^* - f_j^n}{\Delta t} - G_j^n \\ (\mathcal{L} f)_j^n &= (f, _t)_j^n - G_j^n\end{aligned} \tag{A.7}$$

where the subscript $(, t)$ denotes the time derivative. Using the Taylor series

$$f_j^* = f_j^n + \Delta t (f, _t)_j^n + \frac{\Delta t^2}{2}(f, _{tt})_j^n \tag{A.8}$$

and replacing f_j^* in (A.7), we show that the finite difference scheme (A.5) is consistent.

$$(\hat{\mathcal{L}} f^n)_j - (\mathcal{L} f)_j^n = \frac{\Delta t}{2}(f, _{tt})_j^n = \mathcal{O}(\Delta t) \to 0 \qquad \text{for } \Delta t \to 0 \tag{A.9}$$

Now, we consider the second equation in (A.4)

$$\left(\frac{\partial f'}{\partial t}\right)_{(1)} = G' - f'\frac{\partial u}{\partial x} \tag{A.10}$$

where the differential equation and the finite difference scheme at the grid point j are as follows

$$\begin{aligned}(\hat{\mathcal{L}}f^n)_j &= \frac{f_j'^* - f_j'^n}{\Delta t} - \frac{f_{j+1}^* - f_{j-1}^* - f_{j+1}^n + f_{j-1}^n}{2\Delta x \Delta t} + f_j'^n \frac{u_{j+1}^n - u_{j-1}^n}{2\Delta x} \\ (\mathcal{L}f)_j^n &= (f'_{,\,t})_j^n - (G_{,\,x})_j^n + (f_{,\,x})_j^n (u_{,\,x})_j^n\end{aligned} \tag{A.11}$$

Using equation (A.5), we can use relations

$$\begin{aligned}\frac{f_{j+1}^* - f_{j+1}^n}{\Delta t} &= G_{j+1}^n \\ \frac{f_{j-1}^* - f_{j-1}^n}{\Delta t} &= G_{j-1}^n\end{aligned} \tag{A.12}$$

to obtain

$$(\hat{\mathcal{L}}f^n)_j = \frac{f_j'^* - f_j'^n}{\Delta t} - \frac{G_{j+1}^n - G_{j-1}^n}{2\Delta x} + f_j'^n \frac{u_{j+1}^n - u_{j-1}^n}{2\Delta x} \tag{A.13}$$

Using the Taylor series

$$\begin{aligned}f_j'^* &= f_j'^n + \Delta t (f'_{,\,t})_j^n + \frac{\Delta t^2}{2}(f'_{,\,tt})_j^n \\ G_{j+1}^n &= G_j^n + \Delta x (G_{,\,x})_j^n + \frac{\Delta x^2}{2}(G_{,\,xx})_j^n + \frac{\Delta x^3}{6}(G_{,\,xxx})_j^n \\ G_{j-1}^n &= G_j^n - \Delta x (G_{,\,x})_j^n + \frac{\Delta x^2}{2}(G_{,\,xx})_j^n - \frac{\Delta x^3}{6}(G_{,\,xxx})_j^n \\ u_{j+1}^n &= u_j^n + \Delta x (u_{,\,x})_j^n + \frac{\Delta x^2}{2}(u_{,\,xx})_j^n + \frac{\Delta x^3}{6}(u_{,\,xxx})_j^n \\ u_{j-1}^n &= u_j^n - \Delta x (u_{,\,x})_j^n + \frac{\Delta x^2}{2}(u_{,\,xx})_j^n - \frac{\Delta x^3}{6}(u_{,\,xxx})_j^n\end{aligned} \tag{A.14}$$

and substituting them in equation (A.13), we prove the consistency of the finite

difference method used.

$$(\hat{\mathcal{L}}f^n)_j - (\mathcal{L}f)_j^n = \frac{\Delta t}{2}\,(f'_{,\,tt})_j^n - \frac{\Delta x^2}{6}\,(G_{,\,xxx})_j^n + (f_x)_j^n \frac{\Delta x^2}{6}\,(u_{,\,xxx})_j^n = \mathcal{O}(\Delta t, \Delta x^2) \to 0 \tag{A.15}$$

for $\Delta t, \Delta x \to 0$.

After f^* and f'^* are found, they will be taken to the advection phase.

- Advection phase

The equations to be solved are as follows,

$$\begin{aligned} \left(\frac{\partial f}{\partial t}\right)_{(2)} + u\frac{\partial f}{\partial x} &= 0 \\ \left(\frac{\partial f'}{\partial t}\right)_{(2)} + u\frac{\partial f'}{\partial x} &= 0 \end{aligned} \tag{A.16}$$

The CIP solver is applied to the advection phase and the interpolated profile is determined from equations (6.7) and (6.8) using f^* and f'^* on the right-hand side. Since the CIP solver uses the analytical solution, there is no need to prove the consistency of the advection phase.

Note that adding equations (A.4) and (A.16) give equations (A.2) and (A.3) since,

$$\begin{aligned} \frac{\partial f}{\partial t} &= \left(\frac{\partial f}{\partial t}\right)_{(1)} + \left(\frac{\partial f}{\partial t}\right)_{(2)} \\ \frac{\partial f'}{\partial t} &= \left(\frac{\partial f'}{\partial t}\right)_{(1)} + \left(\frac{\partial f'}{\partial t}\right)_{(2)} \end{aligned} \tag{A.17}$$

Solving these equations in two phases is consistent since the values at the end of the non-advection phase (f^* and f'^*) are taken to the advection phase as the initial values.

In this appendix, we proved the consistency of the CIP scheme for the one-dimensional non-linear equation. For more general cases, a similar procedure is followed.

Appendix B

Stability of the CIP scheme

Consider the difference scheme

$$\mathbf{f}^{n+1} = \mathbf{S}\ \mathbf{f}^n \tag{B.1}$$

where $\mathbf{S}$ is the matrix relating the solution at time t ($\mathbf{f}^n$) to the solution at time $t+\Delta t$ ($\mathbf{f}^{n+1}$), and

$$\mathbf{f} = \begin{bmatrix} f_1 & f_2 & \cdots \end{bmatrix}^T \tag{B.2}$$

This difference scheme is stable if there exists C_T such that

$$||\mathbf{f}^n|| = ||\mathbf{S}^n\mathbf{f}^0|| \leq C_T||\mathbf{f}^0|| \tag{B.3}$$

for all $\mathbf{f}^0$; and n, Δt such that $0 \leq n\Delta t \leq T$. Note that the superscript n stands for the time except in $\mathbf{S}^n$ that denotes the power.

The stability analysis of the usual finite difference method is generally formulated using the discrete Fourier transformation (the von Neumann stability criterion). Since the CIP scheme involves spatial derivatives, the von Neumann stability analysis is applied with some modifications. In this appendix, we prove the stability of the CIP scheme for the linear equation when the velocity is constant (this appendix presents the stability in the advection phase). For more general cases, a similar procedure is

followed [21].

Consider the one-dimensional linear equation

$$\frac{\partial f}{\partial t} + u\frac{\partial f}{\partial x} = 0 \tag{B.4}$$

where the velocity u is constant. The equation for the spatial derivative of f is then

$$\frac{\partial f'}{\partial t} + u\frac{\partial f'}{\partial x} = 0 \tag{B.5}$$

We assume that the physical quantity f is discretized spatially for the periodic computational domain $[0, L]$ with the equally spaced $N+1$ grid points ($L = N\Delta x$). The profile $F(x)$ for $(j-1)\Delta x \leq x \leq j\Delta x$ is interpolated using the cubic polynomial shown in equation (6.4). For $u > 0$

$$\begin{aligned} F_j(x) &= w_f(x - j\Delta x)f_j + w_{f'}(x - j\Delta x)f'_j + w_{f-1}(x - j\Delta x)f_{j-1} + w_{f'-1}(x - j\Delta x)f'_{j-1} \\ F'_j(x) &= w'_f(x - j\Delta x)f_j + w'_{f'}(x - j\Delta x)f'_j + w'_{f-1}(x - j\Delta x)f_{j-1} + w'_{f'-1}(x - j\Delta x)f'_{j-1} \end{aligned} \tag{B.6}$$

where

$$
\begin{aligned}
w_f(x) &= 1 - \frac{3x^2}{\Delta x^2} - \frac{2x^3}{\Delta x^3} \\
w_{f'}(x) &= x + \frac{2x^2}{\Delta x} + \frac{x^3}{\Delta x^2} \\
w_{f-1}(x) &= \frac{3x^2}{\Delta x^2} + \frac{2x^3}{\Delta x^3} \\
w_{f'-1}(x) &= \frac{x^2}{\Delta x} + \frac{x^3}{\Delta x^2} \\
w'_f(x) &= -\frac{6x}{\Delta x^2} - \frac{6x^2}{\Delta x^3} \\
w'_{f'}(x) &= 1 + \frac{4x}{\Delta x} + \frac{3x^2}{\Delta x^2} \\
w'_{f-1}(x) &= \frac{6x}{\Delta x^2} + \frac{6x^2}{\Delta x^3} \\
w'_{f'-1}(x) &= \frac{2x}{\Delta x} + \frac{3x^2}{\Delta x^2}
\end{aligned}
\tag{B.7}
$$

Since the function $F_j(x)$ is continuous and periodic, Fourier coefficients for wave number $k = \frac{2\pi n}{L}$ $(n = 0, \pm 1, \pm 2, \cdots)$ are written as

$$
\begin{aligned}
\hat{F}(k) &= \sum_{j=1}^{N} \int_{(j-1)\Delta x}^{j\Delta x} F_j(x)\, e^{ikx}\, dx = \sum_{j=1}^{N} \int_{-\Delta x}^{0} F_j(x + j\Delta x)\, e^{ik(x+j\Delta x)}\, dx \\
&= \sum_{j=1}^{N} e^{ikj\Delta x} \int_{-\Delta x}^{0} (w_f(x) f_j + w_{f'}(x) f'_j + w_{f-1}(x) f_{j-1} + w_{f'-1}(x) f'_{j-1})\, e^{ikx}\, dx \\
&= \hat{W}_f(k) F(k) + \hat{W}_{f'}(k) F'(k) \\
&= \begin{bmatrix} \hat{W}_f(k) & \hat{W}_{f'}(k) \end{bmatrix} \begin{bmatrix} 1 & 0 \\ 0 & 1 \end{bmatrix} \begin{bmatrix} F(k) \\ F'(k) \end{bmatrix}
\end{aligned}
\tag{B.8}
$$

where the notation i is $\sqrt{-1}$ and

$$
\begin{aligned}
\hat{W}_f(k) &= [\hat{w}_f(k) + \hat{w}_{f-1}(k)\ e^{ik\Delta x}] \\
\hat{W}_{f'}(k) &= [\hat{w}_{f'}(k) + \hat{w}_{f'-1}(k)\ e^{ik\Delta x}] \\
F(k) &= \sum_{j=1}^{N}\ e^{ikj\Delta x} f_j \\
F'(k) &= \sum_{j=1}^{N}\ e^{ikj\Delta x} f'_j \\
\hat{w}_f(k) &= \int_{-\Delta x}^{0} w_f(x)\ e^{ikx}\ dx \\
\hat{w}_{f'}(k) &= \int_{-\Delta x}^{0} w_{f'}(x)\ e^{ikx}\ dx \\
\hat{w}_{f-1}(k) &= \int_{-\Delta x}^{0} w_{f-1}(x)\ e^{ikx}\ dx \\
\hat{w}_{f'-1}(k) &= \int_{-\Delta x}^{0} w_{f'-1}(x)\ e^{ikx}\ dx
\end{aligned}
\tag{B.9}
$$

Since $F(k)$ represents the discrete Fourier coefficients for the continuous function $f(x)$, it satisfies

$$
\begin{aligned}
&F(k + \frac{2\pi N}{L}\ ) = F(k) \\
&F(k) = F^*(-k) \qquad \text{for} \quad \frac{2\pi}{L}\ \leq k \leq \frac{\pi N}{L} \\
&F(0) = F^*(0)
\end{aligned}
\tag{B.10}
$$

where the superscript (*) denotes the complex conjugate.

Applying the CIP solver, f^{n+1} and f'^{n+1} are updated as

$$
\begin{aligned}
f_i^{n+1} &= F(x_i - u\Delta t) \\
f_i'^{n+1} &= \frac{dF(x_i - u\Delta t)}{dx}
\end{aligned}
\tag{B.11}
$$

or

$$
\begin{aligned}
f_j^{n+1} &= c_f f_j^n + c_{f'} f_j'^n + c_{f-1} f_{j-1}^n + c_{f'-1} f_{j-1}'^n \\
f_j'^{n+1} &= c_f' f_j^n + c_{f'}' f_j'^n + c_{f-1}' f_{j-1}^n + c_{f'-1}' f_{j-1}'^n
\end{aligned}
\tag{B.12}
$$

where

$$
\begin{aligned}
c_f &= (1 - 3c^2 + 2c^3) \\
c_{f'} &= (-c + 2c^2 - c^3)\Delta x \\
c_{f-1} &= (3c^2 - 2c^3) \\
c_{f'-1} &= (c^2 - c^3)\Delta x \\
c_f' &= \frac{6c - 6c^2}{\Delta x} \\
c_{f'}' &= (1 - 4c + 3c^2) \\
c_{f-1}' &= \frac{-6c + 6c^2}{\Delta x} \\
c_{f'-1}' &= (-2c + 3c^2)
\end{aligned}
\tag{B.13}
$$

and $c = u\Delta t/\Delta x$ (the Courant-Friedrich-Lewy (CFL) number).

The Fourier transform of f after one time step is as follows

$$\hat{F}^{n+1}(k) = \sum_{j=1}^{N} e^{ikj\Delta x} \left[\hat{W}_f(k) f_j^{n+1} + \hat{W}_{f'}(k) f_j'^{n+1}\right]$$

$$\begin{aligned} &= \sum_{j=1}^{N} e^{ikj\Delta x} \left([\hat{W}_f(k)(c_f + e^{ik\Delta x} c_{f-1}) + \hat{W}_{f'}(k)(c'_f + e^{ik\Delta x} c'_{f-1})]\ f_j^n \right. \\ &\quad \left. + [\hat{W}_f(k)(c_{f'} + e^{ik\Delta x} c_{f'-1}) + \hat{W}_{f'}(k)(c'_{f'} + e^{ik\Delta x} c'_{f'-1})]\ f_j'^n \right) \end{aligned} \tag{B.14}$$

$$\begin{aligned} &= [\hat{W}_f(k) C_f + \hat{W}_{f'}(k) C'_f]\ F^n(k) + [\hat{W}_f(k) C_{f'} + \hat{W}_{f'}(k) C'_{f'}]\ F'^n(k) \\ &= \begin{bmatrix} \hat{W}_f(k) & \hat{W}_{f'}(k) \end{bmatrix}\ S(k) \begin{bmatrix} F^n(k) \\ F'^n(k) \end{bmatrix} \end{aligned}$$

where

$$S(k) = \begin{bmatrix} C_f & C_{f'} \\ C'_f & C'_{f'} \end{bmatrix} \tag{B.15}$$

and

$$\begin{aligned} C_f &= (c_f + e^{ik\Delta x} c_{f-1}) \\ C'_f &= (c'_f + e^{ik\Delta x} c'_{f-1}) \\ C_{f'} &= (c_{f'} + e^{ik\Delta x} c_{f'-1}) \\ C'_{f'} &= (c'_{f'} + e^{ik\Delta x} c'_{f'-1}) \end{aligned} \tag{B.16}$$

If we repeat applying the above procedure and we use equation (B.8), we obtain

$$\begin{bmatrix} F^n(k) \\ F'^n(k) \end{bmatrix} = S^n(k) \begin{bmatrix} F^0(k) \\ F'^0(k) \end{bmatrix} \tag{B.17}$$

and

$$\hat{F}^n(k) = \begin{bmatrix} \hat{W}_f(k) & \hat{W}_{f'}(k) \end{bmatrix} S^n(k) \begin{bmatrix} F^0(k) \\ F'^0(k) \end{bmatrix} \tag{B.18}$$

For the stability of the CIP scheme, the growth of the errors should be bounded; the absolute values of all the eigenvalues of the $S(k)$ should be less than unity. The matrix $S(k)$ is periodic over the domain $[0, 2\pi]$ of the independent variable $(k\Delta x)$ and $S(k) = S^*(-k)$. This matrix has eigenvalues

$$\begin{aligned} \lambda_1, \lambda_2 = {} & 3e^{ik\Delta x}c^2 + 1 - e^{ik\Delta x}c^3 + c^3 - e^{ik\Delta x}c - 2c \pm [(c-1)^2\ c^2\ (c^2 + e^{2ik\Delta x}\ c^2 \\ & - 2e^{ik\Delta x}\ c^2 - 4e^{2ik\Delta x}\ c + 2e^{ik\Delta x}\ c + 2c + 10\ e^{ik\Delta x} - 2 + e^{2ik\Delta x})]^{0.5} \end{aligned} \tag{B.19}$$

The absolute values of λ_1 and λ_2 are less than unity for $0 \leq k\Delta x \leq \pi$ and $c \leq 1$. Note that in this appendix, we proved the stability of the CIP scheme for the linear equation when the velocity is constant. For more general cases, a similar procedure is followed.